JOURNAL OF
EMERGING INVESTIGATORS

VOLUME 3, ISSUE 10 | OCTOBER 2020
emerginginvestigators.org

Seizure signals
Developing and evaluating epilepsy-detecting algorithms

Nanotube membranes
Fabricating devices for harnessing osmotic energy

Cephalopod genetics
Solving a technical barrier to sequencing the squid genome

Urban heat retention
Tracking autumn variance in the urban heat island effect

A model for Rett syndrome
Genetic modification in flies to study the disease

JOURNAL OF EMERGING INVESTIGATORS

The Journal of Emerging Investigators is an open-access journal that publishes original research in the biological and physical sciences that is written by middle and high school students. JEI provides students, under the guidance of a teacher or advisor, the opportunity to submit and gain feedback on original research and to publish their findings in a peer-reviewed scientific journal. Because grade-school students often lack access to formal research institutions, we expect that the work submitted by students may come from classroom-based projects, science fair projects, or other forms of mentor-supervised research.

JEI is a non-profit group run and operated by graduate students, postdoctoral fellows, and professors across the United States.

Contents

VOLUME 3, ISSUE 10 | OCTOBER 2020

JOURNAL OF
EMERGING INVESTIGATORS

Article

In vitro comparison of anticancer and immunomodulatory activities of resveratrol and its oligomers

Jeffery F. Zhang[1], Everett Henry[2], L. Harris Zhang[2]
[1]Morris County Vocational School, The Academy for Biotechnology, Mountain Lakes, NJ
[1]Mountain Lakes High School, Mountain Lakes, NJ
[2] NanoBiotec, LLC, Hanover, NJ

SUMMARY

Stilbenoids are a group of naturally occurring phenolic compounds produced *de novo* in many plant species to protect against fungal infection and toxins. Resveratrol (3,4',5-trihydroxystilbene), a stilbenoid isolated from grapes and many species of plants, is widely known for its extensive bioactivities, such as antioxidation, anti-inflammatory and anticancer effects. Recently, many novel resveratrol oligomers have been isolated from various plants. While their structures are diverse, these oligomers are characterized by the polymerization of two or more resveratrol units. Little is known regarding the bioactivities of these novel resveratrol oligomers. We hypothesized that these oligomers might have similar or superior bioactivities to resveratrol. In this study, we designed *in vitro* models to compare resveratrol side by side with natural dimers (ε-viniferin and gnetin H) and trimers (suffruticosol B and C) from plants for their bioactivities. Our data showed that these oligomers, similar to resveratrol, had many activities such as downregulation of cancer cell proliferation, upregulation of normal keratinocyte growth, and the modulation of the expression of pro- and anti-inflammatory cytokines in immune cells. Furthermore, these oligomers appeared to have higher cytotoxicity than resveratrol in normal human blood cells; the order was the trimers (suffruticosol B and C) > dimers (ε-viniferin and gnetin H) > monomer (resveratrol). However, only suffruticosol C, gnetin H and resveratrol showed anticancer activity against human T98G glioblastoma cells at lower concentrations. No correlation between anticancer or immunomodulating effects and the degree of polymerization was observed. Our results provide some preliminary evidences that resveratrol oligomers could be potential preventive or therapeutic agents for cancers and other immune-related diseases. As far as any superiority of efficacy of these stilbenoids is concerned, more extensive studies are definitely needed.

INTRODUCTION

Resveratrol (3,5,4′-trihydroxy-trans-stilbene) is a well-known stilbenoid, a group of naturally occurring phenolic compounds found in many plant species. Stilbenoid are produced *de novo* in plants as antimicrobial compounds to protect against injury or attack by pathogens, such as viruses, bacteria, or fungi (1). Rich sources of resveratrol in food include the skin of grapes, various berries, and others. It is commonly used as a dietary supplement and extensively studied in laboratory models of various human diseases, such as hypertension, diabetes, obesity, cancers, and others (2, 3). Resveratrol has been reported to exhibit a broad variety of biological and pharmacological activities ranging from antibacterial, antiviral, antioxidant, anti-inflammatory, immunomodulation, and cancer prevention (**Figure 1**) (3, 4, 5). For example, resveratrol can be used as complementary therapeutic for autoimmune diseases including multiple sclerosis and immune thrombocytopenic purpura due to its potential to reverse the imbalance of Th17/Treg cells (6, 7). Resveratrol was also reported to have chemopreventive activity on major stages of carcinogenesis (8). Currently multiple clinical trials of resveratrol are ongoing and have focused on cancer, neurological disorders and others. Therefore, it is clear that many beneficial effects of resveratrol have been observed. However, resveratrol's therapeutic efficacy depends on several factors such as types of cancer, demographics, etc. (1).

In the latest decade, many novel stilbenoids similar to resveratrol have been discovered in various plant species (3). These stilbenoids with complex unique structures exist as oligomers of resveratrol (**Figure 2**), resulting from polymerization of two or more resveratrol units (3, 5). There is little information, however, regarding the bioactivities of these novel resveratrol oligomers. We hypothesized that these oligomers, like resveratrol, might have anticancer and immunomodulating activities and potential utility as preventive

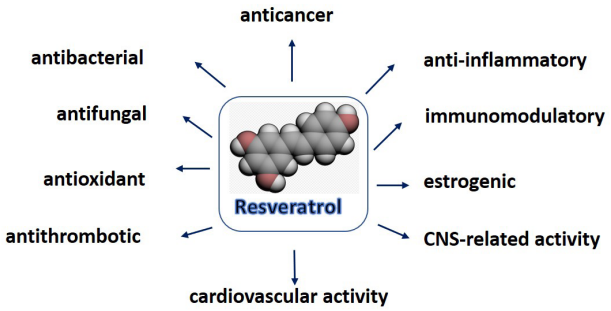

Figure 1. Pleiotropic biological and pharmacological activities of resveratrol. Resveratrol found in many plant and food is commonly used as a dietary supplement. It exhibits a broad variety of biological and pharmacological activities with potential for our wellness.

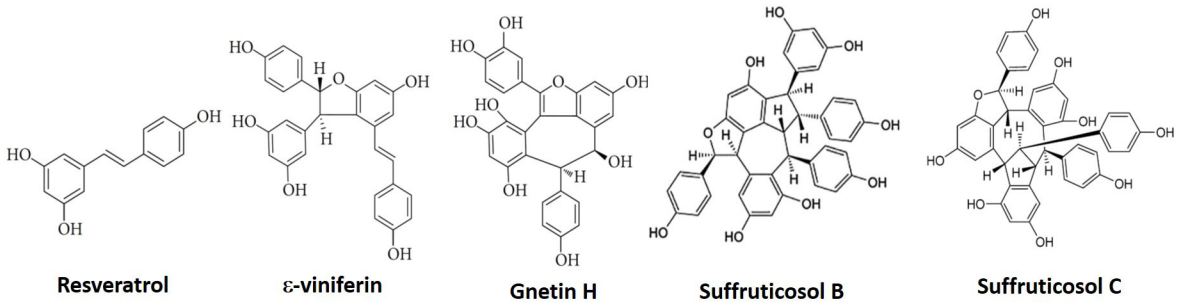

Figure 2. Chemical structures of resveratrol and its oligomers tested in this study. More and more novel stilbenoids similar to resveratrol have been discovered from plants. These stilbenoids have complex unique polyphenolic structures as oligomers of resveratrol.

or therapeutic agents for cancer and other immune-related diseases. It is of particular interest to examine whether these oligomers are comparable or superior to the monomer resveratrol in term of anticancer and immunomodulating activities.

RESULTS

To test our hypothesis, in the present study we designed several *in vitro* cell models to compare side by side the resveratrol versus two dimers and two trimers for their activities on several common cancer cell lines representing human solid and hematopoietic tumor cells, normal human skin cells (keratinocytes), as well as primary immune cells activated with two important stimuli mainly targeting T lymphocytes, monocytes, and B lymphocytes. Before investigation of these five stilbenoid compounds, we set out to test their potential cytotoxic concentrations on normal cells, using peripheral blood mononuclear cells (PBMCs) isolated from normal human blood. We estimated the cell viability by trypan blue staining and microscopic observation (data not shown) and also quantitated adenosine triphosphate (ATP) present in the cell culture, an indicator of metabolically active cells. We tested three concentrations (0.125, 1.25, 12.5 μM) of the compounds. **Figure 3** shows that all these compounds at lower concentrations (0.125-1.25 μM) had no appreciable toxicity (p>0.05). While the dimer gnetin H and the trimers suffruticosol B and C at higher concentrations, ≥ 12.5 μM, started to show significant cytotoxicity (p<0.01 and 0.001), resveratrol and e-viniferin at 12.5 μM had no marked toxicity (p>0.05). The order of toxicity at 12.5 μM is: suffruticosol C > suffruticosol B > gnetin H.

In next experiments, we chose the same non-toxic compound concentrations for normal PBMCs to test any specific cancer-killing activity of these compounds. Five common lines of human cancer cells representing glioblastoma and lymphoma were tested: glioblastoma including A-172, T98G and U-87 cells; and lymphoma including Karpas-422 and RIVA cells. Among these tested cancer cell lines, we found that T98G was the most sensitive to these stilbenoids; proliferation of these cells was pronouncedly suppressed with the treatment of three stilbenoids, namely, resveratrol, the dimer e-viniferin and the trimer suffruticosol C at 1.25 μM (> 50% inhibition, p<0.01), while gnetin H and suffruticosol B up to 1.25 μM had no significant inhibition on T98G cells (p>0.05). Proliferation of the other lines of cancer cells was not clearly impacted by any of these compounds at 1.25 μM (**Figure 4**), although there was significant inhibition of these cancer cells with compounds at 12.5 μM or higher (data not shown).

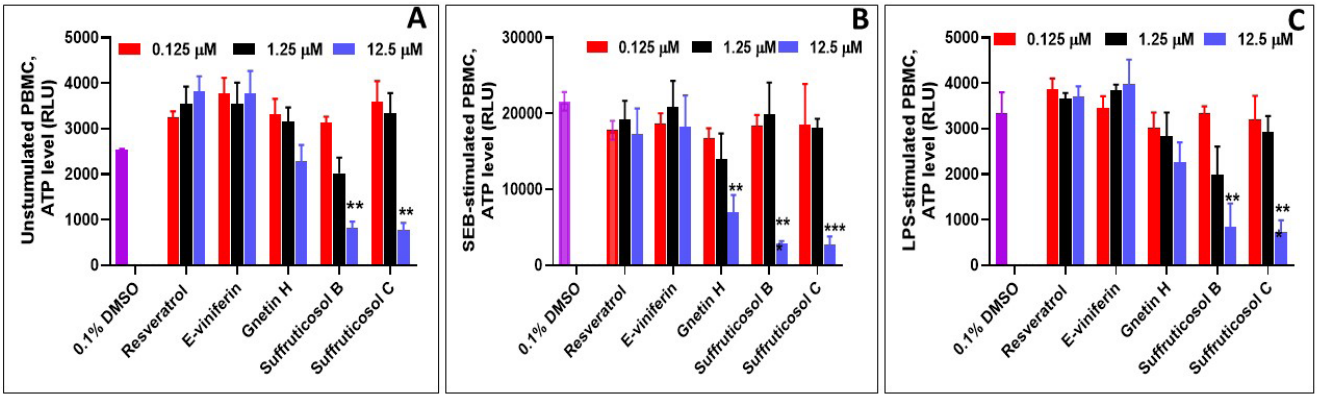

Figure 3. Effects of compounds on growth of human PBMC in the presence and absence of stimuli. Normal PBMCs were isolated from various donors of human blood and cultured in cell plates for 16 h and treated with serially diluted test compounds at concentrations ranging from 0.125-12.5 μM. Following an additional 3 days (Panel A, unstimulated or Panel B, SEB stimulated PBMC) or 1 day (Panel C, LPS stimulated PBMC) of incubation, cell proliferation was determined. Results shown are means ± SD from three experiments (n=3). Analyses for multiple group comparisons were performed with 1-way ANOVA. * P < 0.05, ** P < 0.01 and *** P < 0.001 (compound treated vs 0.1% DMSO control).

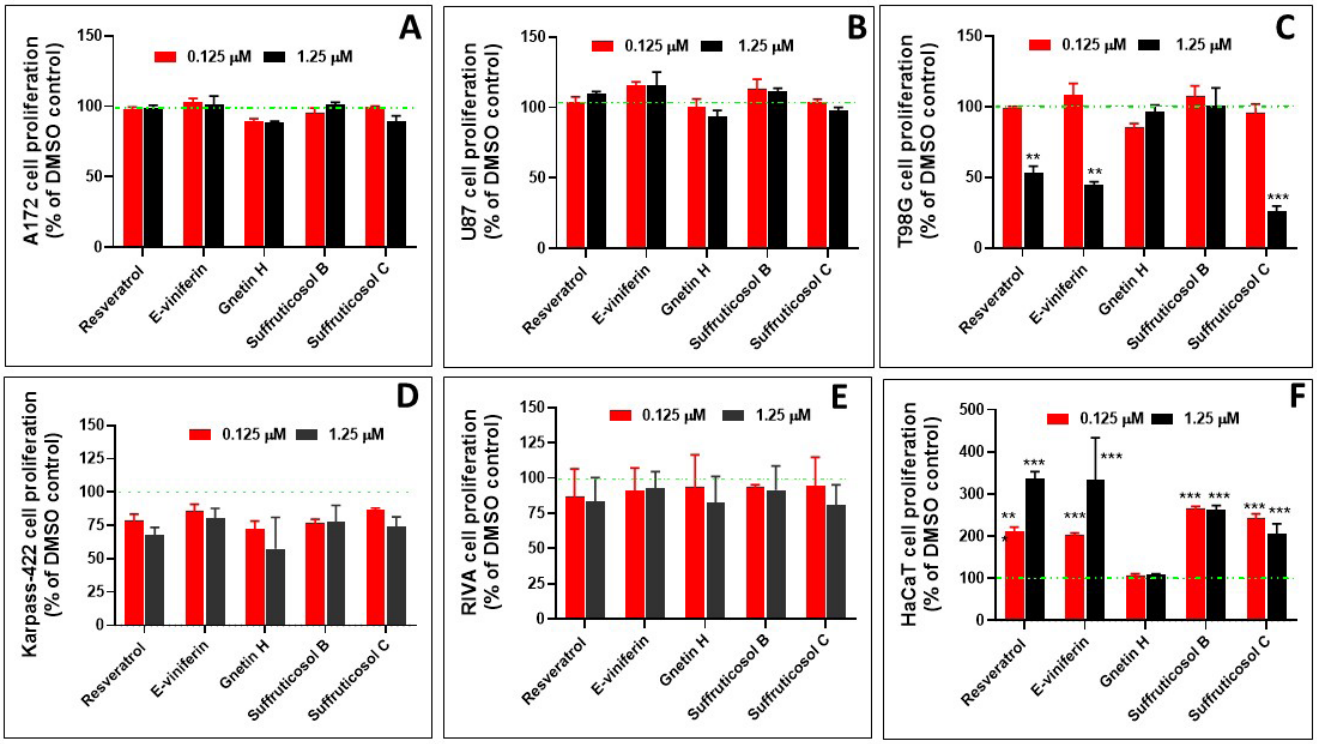

Figure 4. Effects of compounds on proliferation of various human cancer cells and keratinocytes from normal skin. Human cancer cells or skin cells were cultured in cell plates for 16 h and the treated with serially diluted test compounds at concentrations ranging from 0.125-1.25µM. Following additional 3 days of incubation, cell proliferation was determined. Results shown are means ± SD from three experiments (n = 3). Analyses for multiple group comparisons were performed with 1-way ANOVA. * P < 0.05, ** P < 0.01 and *** P < 0.001 (compound treated vs 0.1% DMSO control).

Interestingly, all these stilbenoids (except gnetin H) were able to significantly (*p*<0.01) enhance, by about 100-200%, the proliferation of HaCaT cells, a spontaneously immortalized human keratinocytes from normal skins (10) (**Figure 4**).

The immunomodulatory effect of resveratrol is not very well studied and little is known about effects of its oligomers. To explore the potential immunomodulatory activities of these stilbenoids, we isolate PBMCs from 2 normal donors and stimulated cells with 500 ng/ml of staphylococcal enterotoxin B (SEB). SEB is a superantigen because of its ability to stimulate a large fraction of T cells via interaction with T cell receptors (TCR) and class II MHC molecules (11). The simultaneous binding of SEB outside of the MHC on antigen presenting cells and to TCRs results in eliciting T cell activation and cytokine responses (12). Using Luminex beads-based multiplex cytokine immunoassays, we found that SEB significantly stimulated expression and secretion of many cytokines and chemokines involved in immune responses, inflammation, cell differentiation and growth. Among most of these cytokines, stilbenoids could clearly upregulate their production to various degrees, for example, GRO (growth-regulated oncogene) was induced by ε-viniferin (**Figure 5A**); IL (interleukin)-10 by ε-viniferin and resveratrol (ε-viniferin > resveratrol) (**Figure 5B**); IL-6 by all 5 stilbenoids except gnetin H (**Figure 5C**); GM-CSF (granulocyte-macrophage colony-stimulating factor) by all 5 stilbenoids (**Figure 5D**); and many others (**Figure 5E-H**). However, there were marked downregulation of some cytokines, such as IFN-γ by all compounds except resveratrol and ε-viniferin (**Figure 5J**); IL-10 by gnetin H and suffruticosol B (**Figure 5B**), MIP(macrophage inflammatory protein)-1β by gnetin H (**Figure 5E**) and VEGF (vascular endothelial growth factor) by all compounds except suffruticosol C and ε-viniferin (**Figure 5H**).

Our immune system is highly complex self-balanced network with many subsets of cells which interact with each other and secrete various cytokines or chemokines. To further examine immunomodulatory activities of these stilbenoids on other subsets of immune cells, PBMCs were stimulated with another important stimulus, lipopolysaccharide (LPS) at 1 ng/ml. LPS is a large molecule consisting of a lipid and a polysaccharide and is found in the outer membrane of Gram-negative bacteria. LPS acts as the prototypical endotoxin because it binds the CD14/TLR4/MD2 receptor complex on many immune cell types, especially monocytes, dendritic cells (DC), macrophages and B cells, which then promotes the secretion of pro-inflammatory cytokines, nitric oxide, and eicosanoids (13). In our experiments, the tested stilbenoids could modulate production of many anti- and pro-inflammatory cytokines and chemokines. As shown in **Figure 6**, 24 h of stimulation with 1 ng/ml LPS caused marked increase in production of many cytokines from PBMCs. While the stilbenoids at 0.125 µM had a weak effect on the most of these cytokines, 0.125 µM ε-viniferin could clearly upregulate the production of IL-6 (**Figure 6A**). Although most of these stilbenoids (except

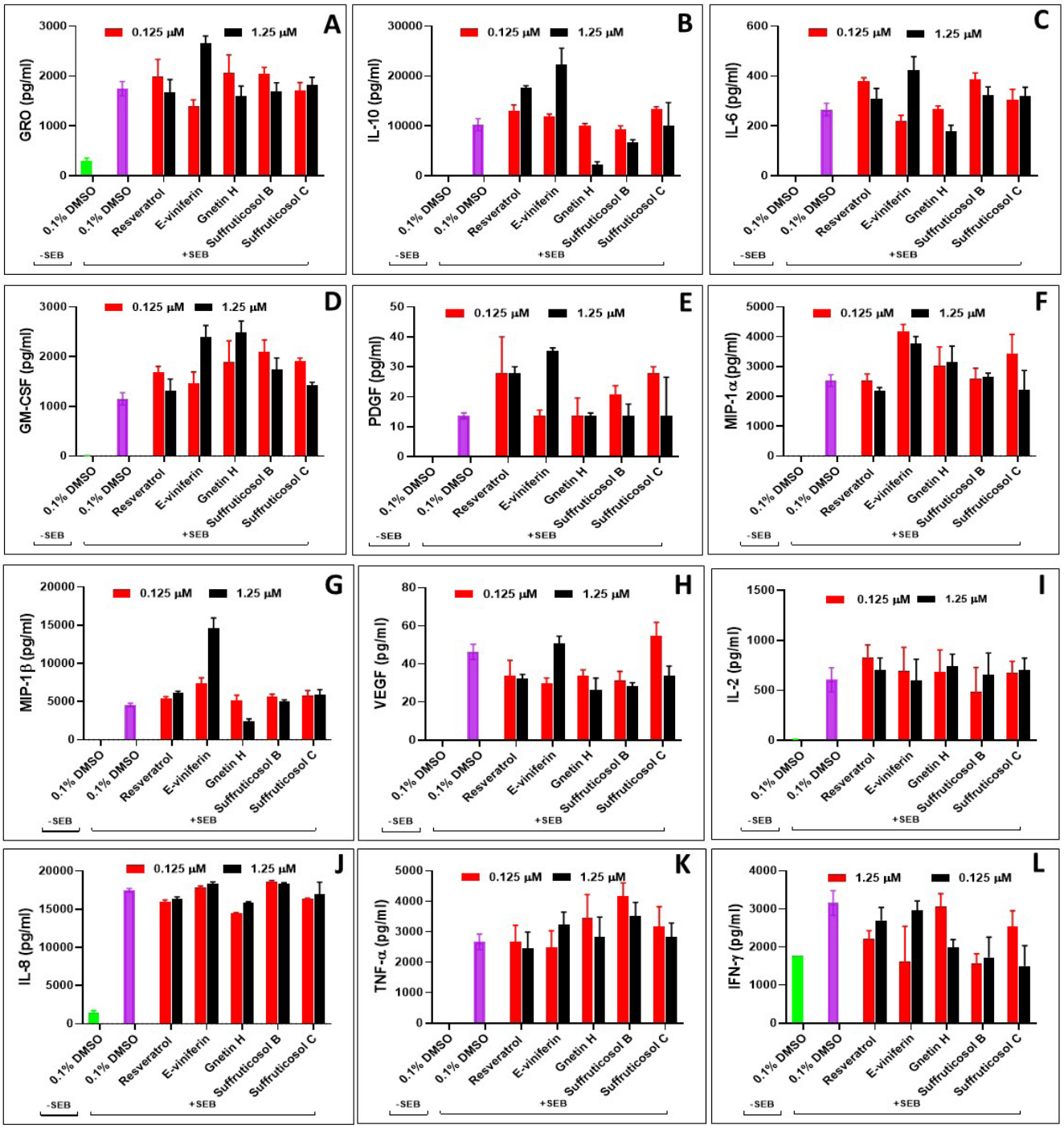

Figure 5. Effects of compounds on cytokine production by SEB induced human PBMC. Normal human PBMC cultures were pre-treated for 30 min with test compounds. The cells were then subject to a further 72-hour stimulation of 500 ng/ml SEB. Following these treatments, cell culture supernatants were harvested for the Luminex-based cytokine assay. The green bar is for unstimulated PBMC control; the purple bar is for SEB-stimulated PBMC control. Results shown are means ± SD from two separate experiments using 2 donors (n=2).

resveratrol or gnetin H) at 12.5 μM were found to have a general toxicity to PBMCs, 12.5 μM resveratrol or gnetin H were able to upregulate the production of several cytokines including IP (interferon-γ inducible protein)-10, TNF-α, IL-23 and IL-4 (data not shown), suggesting that some cell subsets could be activated extensively . In contrast, suffruticosol B and C at 1.25 μM reduced the production of IP-10 (**Figure 6B**), TNF-α (**Figure 6C**), IL-1Rα (**Figure 6D**), IFN-γ (**Figure 6E**) and IL-4 (**Figure 6F**). The production of IL-1 β, IL-10 and IL-23 was relatively unaffected (**Figure 6G-I**). Based on these cytokine data, stilbenoids could possess immunomodulatory activities on T cells, B cells, monocytes, and other immune

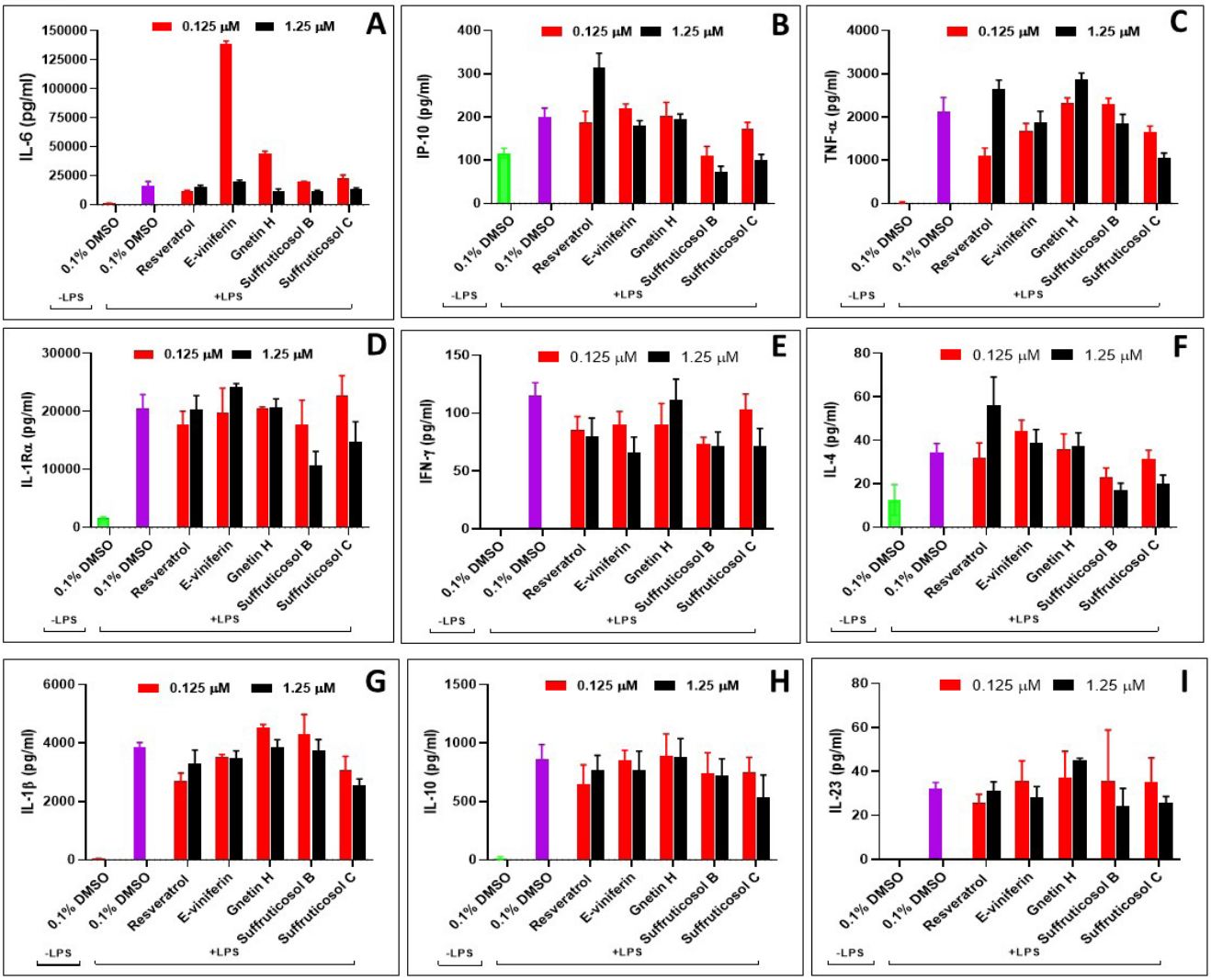

Figure 6. Effects of compounds on cytokine production by LPS induced human PBMC. Normal human PBMC cultures were pre-treated for 30 min with serially diluted test compounds. The cells were then subject to a further 24-hour stimulation of 1 ng/ml LPS. Following these treatments, cell culture supernatants were harvested for the Luminex-based cytokine assay. The green bar is for unstimulated PBMC control; the purple bar is for SEB-stimulated PBMC control. Results shown are means ± SD from two separate experiments using 2 donors (n=2).

cells. Although, it is of note, that the activities appeared not correlated with the degree of oligomerization. It definitely needs further studies to dissect which specific immune cell subsets and cytokines are consistently modulated using more donors of PBMCs or immune cells.

DISCUSSION

In 1985, Kimura, *et al* reported that resveratrol and other monomer stilbenoids could have anti-inflammatory activity by inhibiting arachidonate metabolism in rat leukocytes *in vitro* (14). In 1997, the cancer chemo-preventive activity of resveratrol through antioxidant and antimutagen effects was discovered (8). In the latest decade, more and more natural stilbenoids, including monomers and oligomers, have been isolated from various plants (15). In this study, we aimed to compare resveratrol and its oligomers (2 dimers and 2 trimers) for their cytotoxic, anti-cancer, immunomodulatory and anti-inflammatory activities.

Our data show that resveratrol appeared to have less toxicity to normal blood cells in the presence and absence of stimuli, while dimers and trimers show more toxicity to normal PBMC. The order of cytotoxicity is: suffruticosol C (trimer) > suffruticosol B (trimer) > gnetin H (dimer) > ε-viniferin (dimer) ≈ resveratrol. It is unclear why oligomers appeared to be more cytotoxic. However, more oligomers should be investigated in order to conclude any correlation between the oligomerization degree and toxicity.

Tested at non-toxic lower concentrations, three stilbenoids were found to have some anticancer activities. Particularly, the proliferation of T98G human glioblastoma cells was clearly blocked by resveratrol, ε-viniferin and suffruticosol C. It will be interesting to test these compounds using more lines of cancer cells originated from various tissues. Our preliminary data warrant a further study to understand why T98G cells

were more sensitive to some of these stilbenoids than other cancer cells tested, and the potential molecular mechanism involved in the anticancer activity.

Zhou (16) and Park *et al.* (17) reported photoprotection properties of resveratrol: resveratrol at 10 μM significantly protect HaCaT cells from apoptosis caused by UVB irradiation through upregulating expression of HSP27 (heat shock protein 27), increasing Bcl-2/Bax ratio, inhibiting activity of caspase-3 and -8 and expression of proapoptotic proteins such as p65 and Bax, and reducing production of reactive oxygen species. Their data also showed that resveratrol at 10-100 μM could reduce caspase-3 activity and increase phosphorylation of Rb protein in HaCaT cells without UVB pre-exposure. To our surprise, resveratrol and other stilbenoids at as low as 0.125 μM could actually promote proliferation of HaCaT keratinocytes even without UVB stress. During cancer targeted therapy, especially for non-small cell lung cancer and metastatic colorectal carcinoma, serious cutaneous toxicities from EGFRi (epidermal growth factor receptor inhibitors) treatments are quite common, affecting 45–100% of patients (18). Inhibition of keratinocyte growth and survival is one of major mechanisms of EGFRI toxicity in the skin (19). Our data suggest that these stilbenoids might have a potential to protect keratinocytes from apoptosis to reduce the adverse effects of EGFR-targeting therapies.

It has been reported that repeated doses of resveratrol (1 g/day for 28 days) significantly increased circulating immune cells in healthy individuals, including γδ T cells and regulatory T cells. Resveratrol also significantly improved the growth of γδ T cells and regulatory T cells *in vitro* (20, 21). Our data show that resveratrol and oligomers could regulate production of a variety of cytokines from T cells in SEB-activated PBMCs, and well as from monocytes, B cells and other immune cells in LPS-stimulated PBMCs. This data suggests that resveratrol oligomers, similar to resveratrol, could modulate the activity of various subsets of immune cells. Our data warrant more systematic studies to clearly understand resveratrol and its oligomers as immunomodulatory agents due to the complexity of immune cell and cytokine network.

Although our *in vitro* study results provide some preliminary evidence that resveratrol and its novel oligomers have anti-cancer and immunomodulatory activities, our data have limitations and also prompted many questions for future studies. Further studies are needed for these compounds using more variety of cancer cell lines originated from human tissues, and other subsets of immune cells such as natural killers. It will be also interesting to examine activities for immune cell-mediated cell killing of cancer cells. In order to further explore the potential of these novel compounds as preventive or therapeutic agents for cancers or many immune-related diseases, *in vivo* studies using various animal models are definitely needed to confirm the activities we observed before any clinical study can be performed. As far as the superiority of efficacy of these stilbenoids for human wellness, more studies are needed and more factors should be considered such as oral bioavailability, water solubility, stability, safety and others.

MATERIALS AND METHODS

Test compounds

The five stilbenoid compounds were simultaneously purified from the dried seeds of Paeonia suffruticosa Andr. (Paeoniaceae) as described previously (12) and provided by Professor He, CN at Peking Union Medical College, Beijing, China.

PBMC isolation and stimulation

Peripheral blood from three healthy donors was obtained from BioIVT, Co. (Hicksville, NY). PBMCs were isolated by Ficoll®-Paque Premium density gradient centrifugation, following the protocol from the manufacturer (GE Healthcare, Marlborough, MA). The buoyant layer was removed and the PBMC layer collected. Following several washes in PBS to remove platelets, PBMCs were collected and incubated in RPMI-160 medium supplemented with 10% FBS (fetal bovine serum,) and 1× penicillin/ streptomycin/L-glutamine in a humidified incubator at 37°C with 5% CO_2. Following pre-treatment with test compounds for 1 hour, cells were either stimulated by the addition of 500 ng/ml SEB (Toxin Technology, Sarasota, FL) or 1 ng/ml LPS (Millipore Sigma, St Louis, MO) for 24 h before cell culture supernatants were collected for cytokine assays.

Cell culture of cell lines

A-172 (Glioblastoma), T98G (Glioblastoma), U-87 (Glioblastoma), and HaCaT (keratinocytes) were purchased from ATCC (ATCC®, Manassas, VA) and cultured in DMEM medium supplemented with 10% FBS, penicillin (100 units/ml), streptomycin (100 μg/ml), and L-glutamine (292 mg/ml), and maintained in a humidified incubator at 37°C with 5% CO2. Karpas-422 and RIVA cells (human diffuse large B cell lymphoma) were purchased from DSMZ (Braunschweig, Germany) and cultured in the same complete RMPI-1640 medium as used for PBMC.

Cell proliferation assay

Cell proliferation was assessed using the CellTiter-Glo Luminescent Cell Viability Assay (Promega, Madison, WI), per the manufacturer's protocol. Briefly, in 96-well flat-bottom opaque-walled cell culture plates, the medium control wells containing 100 μL /well cell culture medium without cells were used to obtain a value for background luminescence. For treatment wells, cells were seeded at 2,000 cells in 50 μL/well of complete RPMI-1640 or DMEM medium. Following incubation overnight, cells were treated by adding 50 μL/well of the vehicle control (0.1% DMSO) or test compounds at indicated concentrations. After cells were treated for three days at 37°C in a humidified 5% CO_2 incubator, the plates were equilibrated at room temperature for approximately 30 minutes. 100 μL of CellTiter-Glo® Reagent was added into

each well, and then contents were mixed for two minutes on an orbital plate shaker to lyse cells. After the plates were incubated at room temperature for ten minutes, luminescent signals of each well were recorded with a Tecan M200 Plate Reader (Tecan, Switzerland). Cell proliferation in each test sample from the experiments was examined in duplicate. Compound effects on cell growth were normalized against the DMSO control after cell baseline ATP level was subtracted.

Luminex multiplex cytokine assay

After treatment of PBMCs with test compounds, 100 µL of cell culture supernatants from each well was collected and stored at -80°C for Luminex-based multiplex assays using ProCarta cytokine assay kits (Thermo Fisher Scientific, Waltham, MA) for the following cytokines: TNF-α, IFN-γ, IL-1β, IL-2, IL-10, GM-CSF, GRO, IL-1Rα, IL-6, IL-8, IL-12, PDGF, VEGF, IP-10, IL-23, IL-4, MIP-1α and MIP-1β. Assays were run according to the manufacturer's protocol. Briefly, 25 µL culture supernatants, 25 µL assay buffer, 25 µL antibody-coated bead mixture were added into each well in assay plates and incubated overnight at 4°C on a plate shaker. After washing beads, 25 µL per well of biotinylated detection antibody cocktail and then 25 µL per well streptavidin-phycoerythrin (PE) were added. Following 30 min incubation, data was collected using a Bio-Plex 200 system (Bio-Rad, Hercules, CA). A five-parameter regression analysis was used to calculate the cytokine concentrations from standard curves.

Statistical analysis

All experiments were performed in triplicate or repeated for 2-3 times (n=2 or 3), except as otherwise indicated. Data were graphed and analyzed using GraphPad Prism 8.4 (San Diego, CA); analyses for multiple group comparisons were performed with 1-way analysis of variance (ANOVA) followed by Dunnett's posttest. A value of $p < 0.05$ was considered significant in all analyses.

Received:
Accepted:
Published:

REFERENCES

1. Berman, Adi Y *et al*. "The therapeutic potential of resveratrol: a review of clinical trials." *NPJ precision oncology* vol. 1 (2017): 35. doi:10.1038/s41698-017-0038-6
2. Berretta, Massimiliano *et al*. "Resveratrol in Cancer Patients: From Bench to Bedside." *International Journal of Molecular Sciences* vol. 21,8 2945. (2020), doi:10.3390/ijms21082945
3. Shen, Jie *et al*. "Update on Phytochemistry and Pharmacology of Naturally Occurring Resveratrol Oligomers." *Molecules (Basel, Switzerland)* vol. 22,12 (2017), 2050, doi:10.3390/molecules22122050
4. Espinoza, J Luis, and Pleiades T Inaoka. "Gnetin-C and other resveratrol oligomers with cancer chemopreventive potential." *Annals of the New York Academy of Sciences* vol. 1403,1 (2017): 5-14. doi:10.1111/nyas.13450
5. Xue, You-Qiu *et al*. "Resveratrol oligomers for the prevention and treatment of cancers." *Oxidative medicine and cellular longevity* vol. 2014 (2014): 765832. doi:10.1155/2014/765832
6. Petro, Thomas M. "Regulatory role of resveratrol on Th17 in autoimmune disease." *International immunopharmacology* vol. 11,3 (2011): 310-8. doi:10.1016/j.intimp.2010.07.011
7. Guo, Ning-Hong *et al*. "The potential therapeutic benefit of resveratrol on Th17/Treg imbalance in immune thrombocytopenic purpura." *International immunopharmacology* vol. 73 (2019): 181-192. doi:10.1016/j.intimp.2019.04.061
8. Jang, M *et al*. "Cancer chemopreventive activity of resveratrol, a natural product derived from grapes." *Science (New York, N.Y.)* vol. 275,5297 (1997): 218-20. doi:10.1126/science.275.5297.218
9. Empl, Michael T *et al*. "Effects of a Grapevine Shoot Extract Containing Resveratrol and Resveratrol Oligomers on Intestinal Adenoma Development in Mice: *In Vitro* and *In Vivo* Studies." *Molecular nutrition & food research* vol. 62,2 (2018): 10.1002/mnfr.201700450. doi:10.1002/mnfr.201700450
10. Bastianetto, Stéphane *et al*. "Protective action of resveratrol in human skin: possible involvement of specific receptor binding sites." *PloS one* vol. 5,9 e12935. (2010), doi:10.1371/journal.pone.0012935
11. O'Hehir, R E *et al*. "*Staphylococcus aureus* enterotoxin mediated specific non-responsiveness of human T cells." *Immunology letters* vol. 30,2 (1991): 165-70. doi:10.1016/0165-2478(91)90020-b
12. Rödström, Karin E J *et al*. "Two common structural motifs for TCR recognition by staphylococcal enterotoxins." *Scientific reports* vol. 6 25796. (2016), doi:10.1038/srep25796
13. Kaisho, T, and S Akira. "Critical roles of Toll-like receptors in host defense." *Critical reviews in immunology* vol. 20,5 (2000): 393-405.
14. Kimura, Y *et al*. "Effects of stilbenes on arachidonate metabolism in leukocytes." *Biochimica et biophysica acta* vol. 834,2 (1985): 275-8.
15. He, Chun-Nian *et al*. "Three new oligostilbenes from the seeds of Paeonia suffruticosa." *Chemical & pharmaceutical bulletin* vol. 58,6 (2010): 843-7. doi:10.1248/cpb.58.843
16. Zhou, Fen *et al*. "Resveratrol protects HaCaT cells from ultraviolet B-induced photoaging via upregulation of HSP27 and modulation of mitochondrial caspase-dependent apoptotic pathway." *Biochemical and biophysical research communications* vol. 499,3 (2018): 662-668. doi:10.1016/j.bbrc.2018.03.207
17. Park, Kun, and Ji-Hye Lee. "Protective effects of resveratrol on UVB-irradiated HaCaT cells through attenuation of the caspase pathway." *Oncology reports* vol. 19,2 (2008): 413-7.
18. Lacouture, Mario E. "Mechanisms of cutaneous toxicities to EGFR inhibitors." *Nature reviews. Cancer* vol. 6,10 (2006): 803-12. doi:10.1038/nrc1970
19. Peng, Yanmei *et al*. "Update review of skin adverse events during treatment of lung cancer and colorectal carcinoma with epidermal growth receptor factor inhibitors." *Bioscience trends* vol. 12,6 (2019): 537-552. doi:10.5582/bst.2018.01246
20. Espinoza, J Luis *et al*. "The Repeated Administration

of Resveratrol Has Measurable Effects on Circulating T-Cell Subsets in Humans." *Oxidative medicine and cellular longevity* vol. 2017 (2017): 6781872. doi:10.1155/2017/6781872

21. Pan, Pan *et al*. "The immunomodulatory potential of natural compounds in tumor-bearing mice and humans." *Critical reviews in food science and nutrition* vol. 59,6 (2019): 992-1007. doi:10.1080/10408398.2018.1537237

JOURNAL OF
EMERGING INVESTIGATORS

Article

The effect of the human *MeCP2* gene on *Drosophila melanogaster* behavior and p53 inhibition as a model for Rett Syndrome

Chetana Ganga[1] and Amy Devitt[2]
[1]Evergreen Valley High School, San Jose, California
[2]Schmahl Science Workshops, San Jose, California

SUMMARY

The purpose of this study was to explore the effect of introducing the human methyl CPG binding protein 2 gene (*MeCP2*) into the *Drosophila melanogaster* genome, examine how it would affect protein levels of p53, and test how inhibiting p53 with pifithrin-alpha would affect behavioral and physical patterns in fruit flies. One goal was to observe if the symptoms of Rett Syndrome, a neurodegenerative disease in humans, are reflected in *Drosophila melanogaster*. This was achieved by differentiating the behavior and physical aspects of wild-type flies from flies expressing the full-length *MeCP2* gene and the mutated *MeCP2* gene (R106W). Differences in eye structure, climbing (the use of locomotor skills), geotaxis, as well as differences in the flies' abilities to fly were analyzed. In addition, after these series of tests, the MeCP2 protein and the p53 protein, endogenous to *Drosophila*, were extracted and their levels were compared in each of the populations of flies. Then, after the *Drosophila* consumed pifithrin-alpha hydrobromide, their behavior, physical appearance, and protein levels were again monitored. After conducting these experiments, the effects of full-length and mutant *MeCP2* on *Drosophila melanogaster's* psychomotor skills were analyzed, along with their effects on how the treatment of pifithrin-alpha affected the level of MeCP2 and p53 in the various populations of flies. In conclusion, some of the Rett Syndrome symptoms were recapitulated in *Drosophila*, and a subset of those were partially ameliorated by the introduction of pifithrin-alpha.

INTRODUCTION

Rett Syndrome, a neurodegenerative disease, is associated with a loss-of-function mutation on the *MeCP2* (methyl-CpG–binding protein 2) gene in humans. Rett syndrome patients are almost exclusively females because unfortunately males with this mutation do not survive past their infancy (1). This specific syndrome leads to autism and impairs learning abilities such as basic coordination and cognitive skills. Most of those diagnosed with Rett Syndrome are unable to walk, speak, help themselves, or even recognize their loved ones (1).

MeCP2 protein is found in high levels in the brain, particularly neurons, or nerve cells (1). MeCP2 is responsible for the process of alternative splicing of messenger RNA, which contains the instructions to make protein; MeCP2 also is responsible for maintaining synapses, or connections, between neurons (1). If synapses are broken, then neurons cannot communicate and cannot carry out functions necessary for life. Mutations in the *MeCP2* gene cause a variety of disorders and syndromes. Most relevant to this study, insertions and deletions in the amino acid sequence as well as changes in a single base pairs are mutations that are responsible for changing the structure of the protein or decreasing the amount of MeCP2 protein produced, leading to Rett Syndrome (1).

p53 is a protein that is very closely associated with neurodegeneration and apoptosis (2). The activation of p53 induces malfunction in dendritic branching in neurons, which is also a predominant phenotype of Rett Syndrome. A decreased level of MeCP2 protein in the brain, as a result of a change in structure of the protein, has been shown to induce p53 (3), which, as previously mentioned, leads to neuronal damage (2). It has also been proven that inhibiting the induction of p53 restores the reduced MeCP2 protein levels associated with Rett Syndrome, therefore improving neuronal morphology. In this study, we explore if inhibiting the p53 protein and increasing expression of the MeCP2 protein can possibly reverse the effects of Rett Syndrome.

We chose pifithrin-alpha hydrobromide as the main p53 inhibitor, or MeCP2 stimulator, of the reversed pathway. Pifithrin-alpha is a small molecule known to be a potent inhibitor of the p53 protein (3). Using this molecule, we asked whether p53 protein production would be interrupted, whether that would increase the production of MeCP2 protein and whether it would reverse Rett Syndrome behavior.

We used *Drosophila melanogaster* in this study because these fruit flies have a 60% sequence homology to the human genome (7). Although *Drosophila* do not have an ortholog of the full MeCP2 protein, they do have a gene that encodes the methyl-CpG-binding domain (4). Since Rett Syndrome impairs a variety of cognitive functions in humans, one way

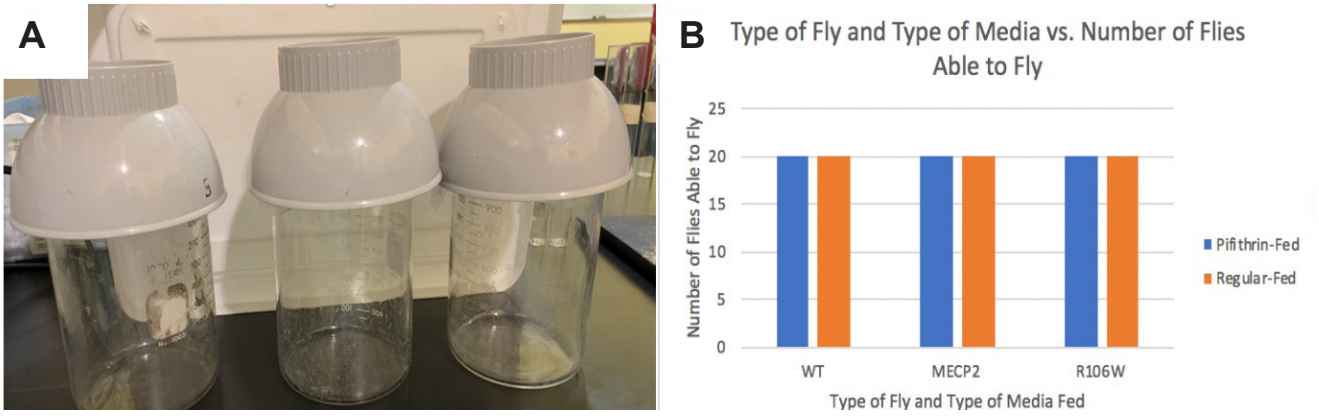

Figure 1. Ability to fly apparatus and results. A) To see if the variously treated flies still retained their ability to fly, three beakers, each covered with bowls, were used as an apparatus. **B)** The number of flies from each group that were able to fly is displayed; the orange bars show the normally fed flies and the blue bars show the pifithrin-fed flies. As seen, there are no error bars for standard deviation since the data for the groups is the same.

to test those cognitive functions in *Drosophila* is by studying their physical behavior. The relationship between cognitive and physical capabilities is established through the concept of psychomotor skills in *Drosophila* (5).We measured differences in psychomotor skills and eye appearance between wild-type flies, flies expressing full-length MeCP2 (FL MeCP2) and flies expressing the mutated MeCP2 (R106W). This was done to detect if the symptoms of Rett Syndrome in humans would be reflected in the flies. The flies were not sexed; this was on the basis that Rett Syndrome is sex-linked in humans and since *Drosophila* do not possess the *MeCP2* gene, there would be no reason to believe it was sex-linked in *Drosophila*. To confirm this, we counted the number of male and female flies in each of the populations and observed them to be equal, before conducting the experiments.

In this project, we compared the physical behavior as well as eye morphology of *Drosophila melanogaster* that consumed regular media to those that consumed pifithrin-alpha infused media. Along with these differences, we measured differences in protein levels of p53 and MeCP2 among the different populations through an ELISA.

RESULTS

Since Rett Syndrome impairs the ability to walk in a human, we tested whether the flying ability in *Drosophila* would be impaired, especially because the *MeCP2* gene is not endogenous to the flies (**Fig. 1A**). Both groups of flies fed with pifithrin-alpha and those not fed the drug for all three of the populations were able to fly (**Fig. 1B**). Throughout the duration of the experiment, we noticed that the wings of the FL MeCP2 flies were positioned higher than that of the other populations, as if electrocuted. They also clearly were moving

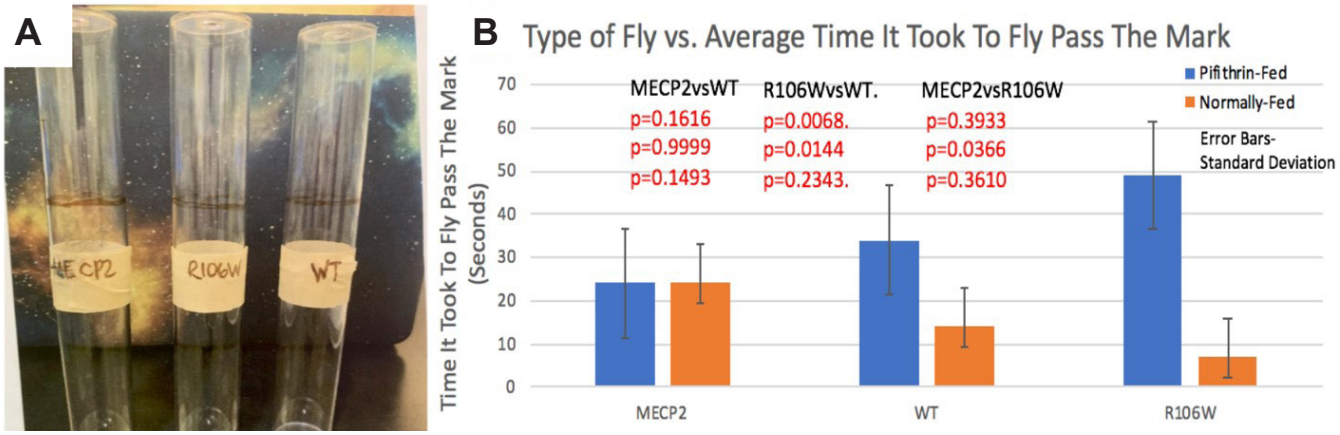

Figure 2. Geotaxis apparatus and results. A) Three of the geotaxis apparatuses are shown. Each one is labeled with its respective group of flies. Each of the apparatuses comprise one upside down vial on top of a right side up vial, taped where the openings meet. The brown mark is 8 cm from the table and is representative of the mark where the flies aimed to pass. **B)** The results of the geotaxis behavioral test are depicted in a bar graph. This data was collected from flies that were fed regular media (orange) and pifithrin media (blue). Ten flies were placed in each of the three apparatuses. The test was repeated for three trials for each apparatus. The mean of the trials is what is displayed on the bar graphs. The same applies for the pifithrin-fed flies. The error bars for standard deviation are shown in black while the resulting *p*-values for the three ANOVAs are shown in red.

at a faster speed than the mutant and the wildtype fly. This was observed subjectively; for example, the FL MeCP2 flies were moving at a pace such that they flew back and forth in the jar three times in the same time that the other flies flew back and forth one time. This is consistent with the hypothesis that decreased levels of MeCP2 protein in the mutant and wild-type fly lead to a slower speed due to a delayed psychomotor ability, similar to how a decreased level of MeCP2 protein in humans impairs walking ability.

To test if the flies still retained their innate ability of negative geotaxis, we performed the geotaxis test (**Fig. 2A**). The pifithrin-fed flies moved slower overall than the flies fed regular food; the pifithrin-fed mutant fly took the longest to regain its negative geotaxis ability (**Fig. 2B**). This is inconsistent with the hypothesis that pifithrin would help the fly enhance one of its psychomotor skills. The three *p*-values from the ANOVAs that were run on this data set are less than 0.05 (5%), which means the null hypothesis can be rejected for those groups: the difference between the normally fed and pifithrin fed groups, the difference between the mutant and wildtype groups, and the difference between the mutant and *FL MeCP2* groups are all significant.

To test the flies' gap-climbing methods and abilities, we observed the technique that the fly utilized to climb across a U-shaped gap, through a camera (**Fig. 3A**). The pifithrin-fed flies used both their front and hind legs in a variety of positions, while the normally fed flies simply used their legs in an upright, simple position while crossing the ledge (**Fig. 3 B-D**). While each pifithrin-fly was traversing the gap individually, their bodies were more spread out and facing different directions, while the legs can be seen to be in various positions, not just upright; this was seen among all the flies (**Fig. 3E-G**). This difference in the way the flies crossed the ledge shows how the pifithrin-fed flies resorted to less traditional, yet more creative ways to gap-climb than the regular-fed flies.

To see if a more physical aspect of the fly differed among the variously affected flies, we assessed eye structure. The pifithrin-fed flies (**Fig. 4D-F**) had a darker eye color as compared to the normal-fed flies (**Fig. 4A-C**). The eye structure of the pifithrin-fed *FL MeCP2* fly was glossier and smoother (**Fig. 4E**) instead of having a defined shape like the other flies, in which the hexagonal, pixel-like pattern of the eye is seen.

To compare the varying MeCP2 and p53 levels in each population, we conducted an ELISA (**Fig. 5**). The data shows that the MeCP2 protein expression starts out at a very low level in the normally fed R106W fly and spikes up with the application of pifithrin, consistent with the hypothesis. The MeCP2 level for the pifithrin-fed mutant fly was the highest, as hypothesized (**Fig. 5B**). We cannot conclude anything about the relationship between p53 and MeCP2 since the p53 ELISA failed (**Fig. 5A**). Since the MeCP2 ELISA did work, three sets of two-way ANOVAs without replication (comparing mutant to wild type, FL MeCP2 to wild type, and FL MeCP2 to mutant, all with respect to pifithrin and normal media) were

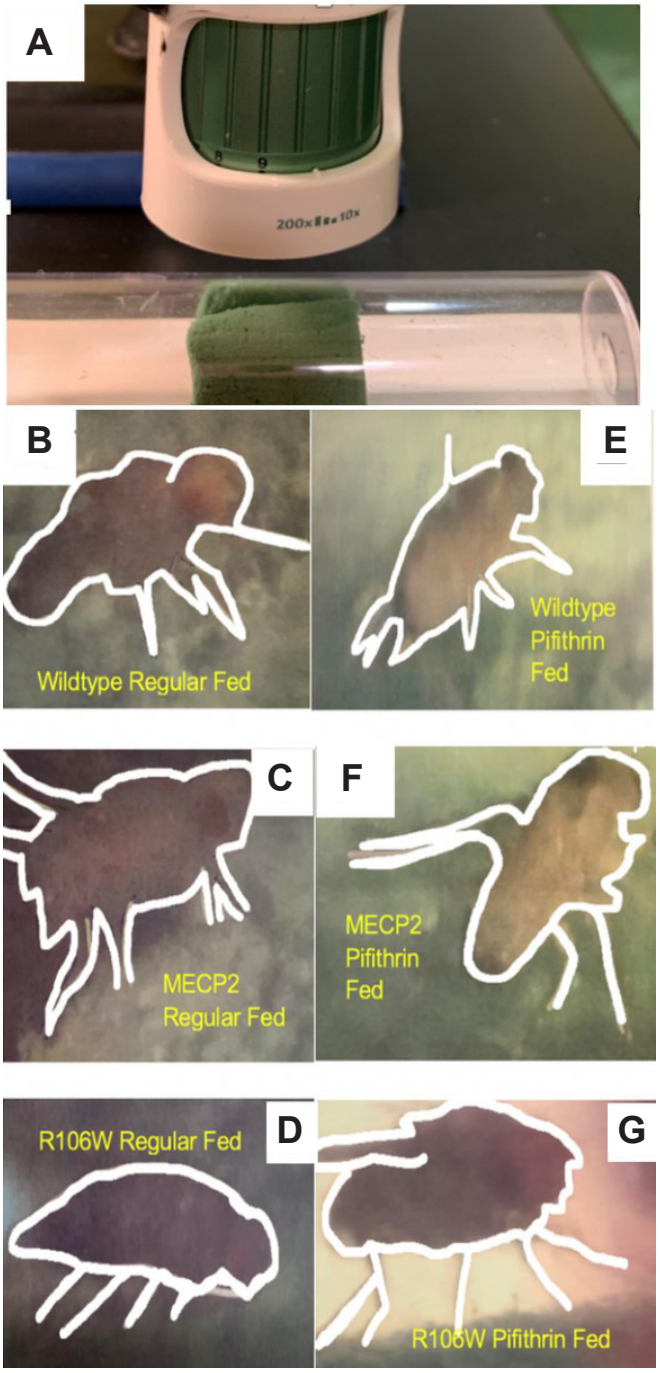

Figure 3. Gap-climbing apparatus and results. A) The apparatus used for the gap-climbing behavioral test is shown. The high-speed camera is held in place with a ring clamp and ring stand. It is situated on top of a vial lying sideways inserted with a piece of green foam with a U-shape cut-out (the gap the flies had to climb to reach the other side of the green foam). **(B-G)** Pictures taken of the regular-fed and pifithrin-fed flies using a high-speed camera are shown. **B)** A wild-type fly fed with regular media is shown. **C)** A MeCP2 fly fed with regular media is shown. **D)** A R106W fly fed with regular media is shown. **(E-G)** there are wild-type, FL MeCP2, and R106W flies, respectively, fed with pifithrin, instead of regular media. Outlines of the flies' head and legs were digitally drawn to identify the flies' methods and their choice of back or front legs to climb the gap.

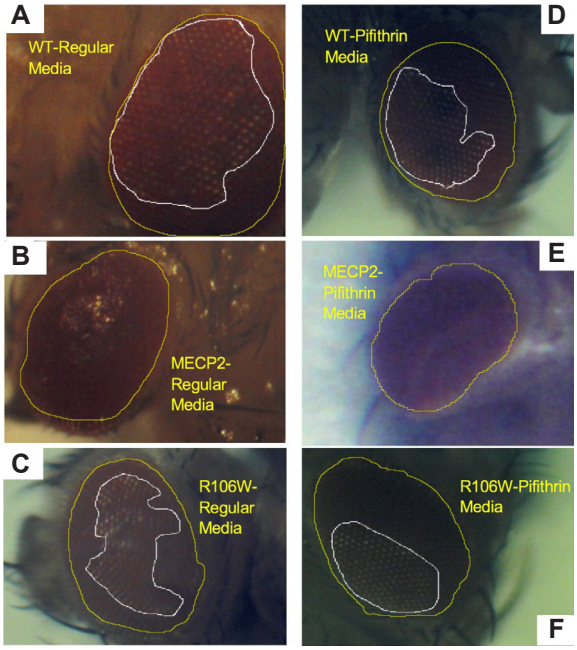

Figure 4. Eye structure results. In this figure, pictures of a zoomed-in view through a microscope of the flies' eye structures are shown. **(A-C)** Once again, in the first column, wild-type, FL MeCP2, and R106W flies respectively are pictured; these were fed with regular media. **(D-F)** Wildtype, FL MeCP2, and R106W flies fed with pifithrin are depicted. The flies' eyes were digitally outlined in white to show the actual eyeball and then outlined in yellow to accentuate the area where the color and pattern of the eyes stands out.

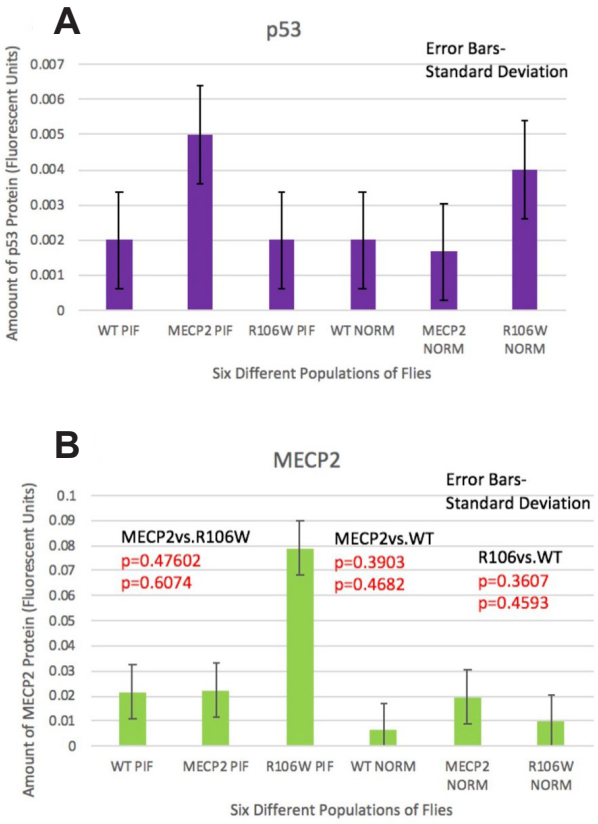

Figure 5. ELISA results. This figure displays bar graphs of the data gathered from the ELISA. **A)** The purple bar graph shows the amount of p53 protein, in fluorescent units, extracted from each of the six different populations of flies. **B)** The green bar graph represents the amount of MeCP2 protein, also in fluorescent units, extracted from each of the six different populations of flies. The error bars for standard deviation are displayed in black. Three sets of two-way ANOVAs with replication (comparing wild type to mutant, wild type to FL MeCP2, and FL MeCP2 to mutant, all with respect to pifithrin and normal media) were used to analyze this data and the resulting *p*-values for sample, column, and interaction are displayed in red.

run on the data. The resulting *p*-values for sample, column, and interaction are displayed in red. In this case, none of the *p*-values were less than 0.05 (5%), which doesn't allow the null hypothesis to be rejected; there is no statistically significant difference between the mutant, wildtype, and FL MeCP2 (normally or pifithrin fed). However, within the graph of the MeCP2 protein amounts, the amounts are visually distinct for each group.

For the MeCP2 ELISA, the MeCP2 levels are consistent with the hypothesis that MeCP2 levels would increase with the insertion of pifithrin-alpha. The protein levels seem to have increased when the flies were fed with pifithrin-alpha, according to what the assay displays. It can be safely concluded that pifithrin-alpha is affecting the level of MeCP2 inversely. We could not identify p53 as the protein affecting MeCP2, since the p53 ELISA did not seem to work. Together, the protein and physical tests respectively confirmed the hypothesized claim that pifithrin-alpha would increase the amount of MeCP2 protein and disproved the prediction that *all* Rett Syndrome symptoms are reflected and reversed when *Drosophila* consume pifithrin, since the flies displayed behaviors that deviated from the expected ones in some of the physical tests.

DISCUSSION

From the data, we safely concluded that pifithrin-alpha is, through some way, affecting the level of MeCP2. However, the p53 ELISA did not work and the reason behind it was explored. Because the range of the fluorescent units is so much larger for MeCP2 than that of p53 (**Fig. 5**), and the p53 signals were lower than the amounts expected for the extracted p53 protein, we propose that the p53 ELISA did not work. The standard curve for the p53 ELISA also did not work as the R^2 value was not close to 1. The p53 ELISA did not function appropriately; in other words, the p53 antibody did not bind with the p53 protein and the amounts of protein displayed on the bar graph therefore cannot be used to draw any conclusions. Therefore, since the results were inconclusive, p53 may or may not be the source through which the pifithrin is affecting the MeCP2. Optimizing the p53 antibodies, testing the assay with different p53 antibodies, and testing other proteins on that pathway to see if they might be responsible for the relationship between pifithrin and MeCP2 are possible projects that could be pursued in the future. As for the MeCP2 ELISA, the ANOVAs proved that there was

no difference between the groups compared. However, when the assay is analyzed by eye, there is clearly a difference between each of the groups. To avoid this discrepancy with the ANOVA in the future, a good addition to the experiment would be to gather multiple replicates for each group in the assay; this may allow for the ANOVA to result in a rejection of the null hypothesis. The reason for the lack of difference could possibly be because of the noisy signal of the ELISA.

The restoration of MeCP2 protein levels repairs the communication between neurons allowing more synapses to be made and therefore prevents dysfunctions of motor skills in a human (4). However, the increase of MeCP2 levels observed in the various flies has proven to enhance and deteriorate certain skills such as their response to negative geotaxis. The statistical analysis for this test proved that there is a difference between the mutant and FL MeCP2 fly, when fed pifithrin, and that the difference is not by chance or sampling error. This difference supports the hypothesis that the mutated fly would be slower than the FL MeCP2 fly when fed with regular media. When we observed the data holistically, the insertion of pifithrin worsened the flies' responses to negative geotaxis, instead of improving it (inclusive of the statistically significant difference between the two groups). In addition, the flies' abilities to fly were also retained, even in the normally fed mutant fly, which we expected to have an impaired flying ability. Meanwhile, the gap-climbing and eye structure test results display binary evidence of the augmentation of certain other motor skills of the *Drosophila* treated with the pifithrin. While the success of these two tests confirm that *Drosophila* may be the ideal species to explore the symptoms of Rett Syndrome through a physical lens, the failure of the other two physical tests point out that different, more specific physiological tests are required to explore the behavior at a more intricate level.

Drosophila do not have an ortholog to *MeCP2* (2), so why the pifithrin seems to increase the expression of MeCP2 in the wildtype flies remains unclear. The flies might have gotten mixed up and/or crossed when breeding. It seems that if the amount of protein as indicated by the ELISA assay is correct, there is some kind of low-level cross reactivity with the MeCP2 antibody and the wild-type *Drosophila*. The data shows that the p53 antibody may not have bound to the *Drosophila* p53 homolog, as the ELISA assay for the p53 did not work. Future projects can possibly test various concentrations and dilutions of different p53 antibodies for the one that will allow for it to bind to the protein.

Overall, the results woven together along with the statistical analysis demonstrate that the reverse pathway model was effective and accurate with regards to MeCP2 and pifithrin. If the p53 ELISA had worked, the model would be even more compelling. There is no confirmation that pifithrin-alpha is an inhibitor of the p53 protein, but there is confirmation that the pifithrin-alpha is a stimulator of MeCP2 expression. Testing the reversed pathway did seem to work, as inserting pifithrin did somehow cause the level of MeCP2 to increase, but by what means and if it specifically improved the neural activity by restoring synapses in the flies remains unclear. As mentioned previously, conducting more specific physiological tests on the flies might provide more insight into neural activity. The MeCP2 protein is found at reduced levels in humans diagnosed with Rett Syndrome, so this project is a contribution to the ways that MeCP2 level as well as cognitive abilities can be restored.

MATERIALS AND METHODS

Physical Study

The flies used for these tests belong to three different populations: the wildtype *Drosophila* (control group), the *Drosophila* inserted with the full length *MeCP2* gene (experimental group), and the *Drosophila* inserted with the mutated *MeCP2* (R106W) gene (experimental group). These strains were provided by Dr. Botas, Department of Molecular and Human Genetics, Baylor College of Medicine, Houston, Texas. These three populations were fed with regular Formula 4-24® Instant Drosophila Medium, Blue. There were two vials for each of the three populations. Each vial contained one tablespoon of the media, nine mL of water, several yeast kernels and ten flies, which means there were 20 flies for each population in total. The flies were age-synchronized in their respective vials; the adults were shifted to new vials after consuming media and breeding for one week. The larvae that were produced in that week were given 12 days to grow (6) before they were tested. The experiments were performed in the span of two hours.

Test 1 (Ability to Fly)

20 flies from each population were placed into separate beakers (**Fig. 1A**) and covered as soon as they were let in. It was observed to see if they took flight to move around the vast space inside the beaker. Flying is a basic locomotor skill for flies, just like how walking is one for humans. Rett Syndrome impairs the ability to walk, which is why this behavioral test is suitable.

Test 2 (Geotaxis)

One empty vial was labeled with a mark around the circumference of the vial 8 cm from the bottom. 10 flies from each population were added to the bottom vial and the second vial (upside down) was quickly taped to the first one, so that no flies escaped (**Fig. 2A**). The apparatus was quickly turned upside down and back to disrupt the flies' center of gravity and then, the flies were tapped down to the bottom. The number of flies that flew above the six cm mark after ten seconds with a timer were measured (**Fig. 2B**). This whole experiment was repeated three times for each population. The purpose of flipping the apparatus over and back is to test the flies' innate ability to ascend the vial as an escape response to being drastically shifted in an environment.

Test 3 (Gap-Climbing)

A piece of foam cut out to shape a U was obtained and placed inside a vial (**Fig. 3A**) (3). A fly was directed to the top-left ledge of the foam and photos were taken using a high-speed video camera (DLite USB Microscope, 5 MegaPixels STR5MP-1213T) as the fly climbed from the left side to the right side of the structure (**Fig. 3B**). Whether the fly used its front or hind legs (or both) to climb across the structure was noted.

Test 4 (Eye Structure)

The eye structure of four flies from each population was individually observed with an OMAX 10X-20X-30X-60X Binocular Student Stereo Microscope with USB Camera. Eye structure is an effective phenotype that is used to identify genetic differences in models for neurological diseases (4). Differences in appearance of the texture of flies' eyes were assessed. Different patterns or different textures of the eye are indicative of a difference in phenotype due to the level of MeCP2 protein (2).

Insertion of Pifithrin-Alpha

Five mg of pifithrin-alpha hydrobromide (Sigma Aldrich) was dissolved in DMSO and water to a concentration of 20 µg/mL. Nine milliliters of this solution were seeded into tubes containing a level scoop of 1 tablespoon of Carolina fly media. For 12 days, the flies consumed the pifithrin-laced media. All four of the behavioral tests were conducted again, using the flies that had consumed the pifithrin for one week.

Protein Study

Protein Extraction

The flies were placed in the freezer for 10 minutes. Twenty flies from each group were used: 20 wild-type normally fed flies, 20 FL MeCP2 normally fed flies, 20 R106W normally fed flies, 20 wild-type pifithrin-fed flies, 20 FL MeCP2 pifithrin-fed flies, and 20 R106W pifithrin-fed flies. Prior to protein extraction using the Protein Purification Kit (Invent Biotechnologies, Inc. 8) the buffers were chilled in the collection tube on ice. Twenty frozen flies were placed in the filter and 200 µL of Buffer A was added to the filter. The frozen flies were ground with a plastic rod 50-60 times with twisting motions. 200 µL of Buffer B was added to the filter and the flies were ground for another 30-60 times. The filter was capped and centrifuged in a microcentrifuge at top speed for one minute. The flow through contained total protein extract. The clear supernatant was transferred to a fresh tube. This was repeated for each of the six groups of flies.

ELISA

The extracted protein from the flies as well as the respective purified MeCP2 or p53 protein (Aviva Systems Biology) were diluted to a final concentration of 20 µg/mL in PBS. 50 µL of the diluted protein solution from the flies was plated in a PVC microtiter plate. Standard curves of the purified MeCP2 protein and the purified p53 protein were made by preparing six 1:5 serial dilutions, with 50 µL in each well. The purpose of including a standard curve on the plate was to extrapolate the yields of the extracted proteins. The plate was covered with an adhesive plastic and incubated at 4°C for three days. The coating solution was removed, and the plate was washed twice by filling the wells with 200 µL PBS. The solutions or washes were removed by flicking the plate over a waste container. The remaining drops were removed by patting the plate on a paper towel. The remaining protein-binding sites in the coated wells were blocked by adding 200 µL of blocking buffer, 5% nonfat dry milk in PBS, per well. The plate was covered with an adhesive plastic and incubated overnight at 4°C. The plate was washed twice with PBS. 100 µL of the respective anti-MeCP2 antibody (Sino Biological) or anti-p53 antibody (Antibodies-Online) was added, diluted at a 1:1000 concentration in the blocking buffer. The plate was covered with an adhesive plastic and incubated over two days at 4°C. The plate was washed two times with PBS. 100 µL of the Anti-Rabbit IgG, HRP-linked Antibody (Cell Signaling Technology) diluted at 1:1000 in the blocking buffer was dispensed into each well. The plate was covered with an adhesive plastic and incubated overnight at 4°C. The plate was washed four times with PBS. 100 µL of TMB Substrate (BioLegend) was added to the wells. It was incubated for 30 minutes and then 50 µL of TMB Stop Solution (BioLegend) was pipetted into the wells. The absorbance (optical density) at 540 nm of each well was read with a microplate reader (9).

Received: April 13, 2020
Accepted: August 18, 2020
Published: September 7, 2020

REFERENCES

1. "MECP2 Gene - Genetics Home Reference - NIH." *U.S. National Library of Medicine*, National Institutes of Health, ghr.nlm.nih.gov/gene/MECP2.
2. Chang, J. Robert, *et a*l. "Role of p53 in Neurodegenerative Diseases." *Neurodegenerative Diseases*, vol. 9, no. 2, 2012, pp. 68–80., doi:10.1159/000329999.
3. Ohashi, Minori, *et al*. "Loss of MECP2 Leads to Activation of P53 and Neuronal Senescence." *Stem Cell Reports*, vol. 10, no. 5, 2018, pp. 1453–1463., doi:10.1016/j.stemcr.2018.04.001.
4. Cukier, Holly N., *et al*. "Genetic Modifiers of MeCP2 Function in Drosophila." *PLoS Genetics*, vol. 4, no. 9, 2008, doi:10.1371/journal.pgen.1000179.
5. Iliadi, Konstantin G., *et al*. "Psychomotor Behavior: A Practical Approach in Drosophila." *Frontiers in Psychiatry*, vol. 7, 2016, doi:10.3389/fpsyt.2016.00153.
6. Vijayalakshmi, M. "Biotechnology - Systems Biology." *NPTEL*, nptel.ac.in/courses/102/106/102106035/.
7. Nagaraja, M. "The Fruit Fly in You." *NASA*, NASA, science.

nasa.gov/science-news/science-at-nasa/2004/03feb_fruitfly/.

Protocols

8. https://cdn.shopify.com/s/files/1/0063/4575/2687/files/4-SB-004_v2.pdf?10427244911784195526
9. https://www.abcam.com/ps/pdf/protocols/Sandwich_ELISA.pdf

JOURNAL OF
EMERGING INVESTIGATORS

Article

Assigning lightning seasons to different regions in the United States

Elyse Hawkins and Chelsea Barreto
Summit High School, Summit, New Jersey

SUMMARY

Climate change is predicted to increase the frequency of severe thunderstorm events in coming years (1). Severe thunderstorms are often accompanied by lightning, which causes an average of 243 injuries and 27 deaths per year in the United States (US) alone (2). With these predicted increases in lightning events, it is important to understand and practice safety during severe thunderstorms. We examined severe thunderstorm data from the National Oceanic and Atmospheric (NOAA) database in seven states in the US (Colorado, Florida, Maine, Minnesota, New Jersey, Washington and West Virginia) to characterize lightning seasons over three years (2000, 2008, and 2017). We hypothesized that (i) the majority of severe thunderstorm events will occur in the summer months in all states examined for all years analyzed, (ii) climate change will cause an unusual number of severe thunderstorm events in winter months in all states, (iii) thundersnow would be observed in Colorado, and (iv.) there would be no difference in the number of severe thunderstorm events between states in any given year examined. We were able to classify lightning seasons in all states observed, with the most severe thunderstorm events occurring in May, June, July, and August. Colorado, New Jersey, Washington, and West Virginia were found to have severe thunderstorm events in the winter, which could be explained by increased winter storms due to climate change (1). Overall, it is important to quantify when lightning seasons occur to avoid lightning-related injuries or death.

INTRODUCTION

It is predicted that climate change will cause an increase in the frequency of lightning and severe thunderstorm events in coming years (1). This is due to increases in the global mean temperature, precipitation, and convective available potential energy (CAPE) that comes with climate change (1). Lightning frequency itself is predicted to increase by 12-15% for every 1°C of warming, projected to result in an increase of as much as 50% over the next century (1). With this predicted increase in lightning events in coming years, it is important to classify when lightning seasons may occur and what locations across the United States are most at risk. Lightning seasons can occur year-round in some locations in the US (2). However, defining a lightning season as when lightning strikes are most likely to occur can ensure safety precautions are put in place (2).

A lightning season is the time of the year when thunderstorms are most likely to develop and occur. There is an average of 243 injuries and 27 deaths per year due to lightning in the United States (3). Lightning injuries can occur when people are outdoors and are unaware of an incoming storm. Outdoor activities that pose a danger to lightning include outdoor sports such as golf (which involves metal poles that attract lightning strikes), swimming (especially in areas with flat, wide beaches), hiking (particularly at high elevations), soccer (on open fields), boating (in open ocean) and camping. Thundersnow can also cause lightning strikes during such sports as skiing and snowboarding (4). Lightning strikes can lead to serious injuries or death, whether they occur outdoors or indoors. With the predicted increase in lightning flashes due to climate change, storm-related injuries are also likely to increase (1).

According to the National Oceanic and Atmospheric Association (NOAA), severe thunderstorm events are a common late spring and summer occurrence in the United States, and they are defined as having winds of over 58 miles per hour, quarter-sized hail (24.26 mm in diameter), and frequent lightning (3). Other regions of the world experience severe thunderstorm events at different times. Globally, the most frequent lightning strikes occur in regions such as Lake Maracaibo, Venezuela; Kabare, Democratic Republic of Congo; and regions close to the equator that have large bodies of water that create near constant lightning storms (5). Uncommon events that occur during severe thunderstorms events include tornadoes, golf ball- to baseball-sized (1.68 to 2.875 inches in diameter) hail, downdrafts of wind (including more severe microbursts), and derechos (fast-moving windy thunderstorms) (3). Severe and large wildfires are known to produce their own weather effects, in some cases producing thunderstorms, and in certain conditions, generating a fire tornado (6). Volcanic eruptions can also produce lightning from clouds of volcanic ash. Lightning can even strike in an area with a clear sky 5-10 miles ahead of a severe thunderstorm (3). Lightning can also be produced from snow-bearing clouds; this is commonly referred to as thundersnow (2).Though very rare, thundersnow storms have been recorded in the Rocky Mountain Region as well as the

Great Lake Region (6). Since lightning can occur in multiple types of weather events, more awareness and caution should be taken to avoid injury during severe weather phenomena.

To date, there are no studies that quantitatively assign lightning seasons in the United States. Research on lightning is limited to lightning maps that show lighting frequency across the United States, which have been generated by NOAA and the National Lightning Detection Network. These nationwide organizations utilize resources for data collection such as lightning mapping arrays, which are sensors set up to track lightning through very high frequency (VHF) impulses (7). These sensors can detect the exact location of a lightning strike (7). Using the NOAA database, lighting seasons can be quantified by finding the average amount of severe thunderstorm events with lightning strikes for each month of the year every state in the US. Using these averages can help us determine the time of year when the most lightning strikes will occur in a given state. It is important to quantify when lightning seasons occur to avoid lightning-related injuries or death.

In this study, we examine the frequency of lightning in different regions in the US to assign lightning seasons using the parameters specified. We examined severe thunderstorm events in regions that had geographical importance or large populations. The seven states chosen were Colorado, Florida, Maine, Minnesota, New Jersey, Washington, and West Virginia. The purpose of examining severe thunderstorm events in different regions (Northeast, Southeast, Midwest, and Northwest) is to find specific patterns in the seasons (months) that have the most severe thunderstorm events, including the most frequent lightning events. We chose three different years to examine over a span of approximately two decades: 2000, 2008, and 2017. These years were chosen to look at how severe thunderstorm events have changed over a longer period of time, as well as how those changes relate to larger climate change patterns. We hypothesize that (i.) the majority of severe thunderstorm events would occur in the summer months in all states examined for the years 2000, 2008, and 2017; (ii.) climate change would cause unusually severe thunderstorm events in winter months in all states examined; (iii.) thundersnow would be observed in Colorado, as thundersnow is most common in that region; and (iv.) there would be no difference in the number of severe thunderstorm events between states in any given year examined.

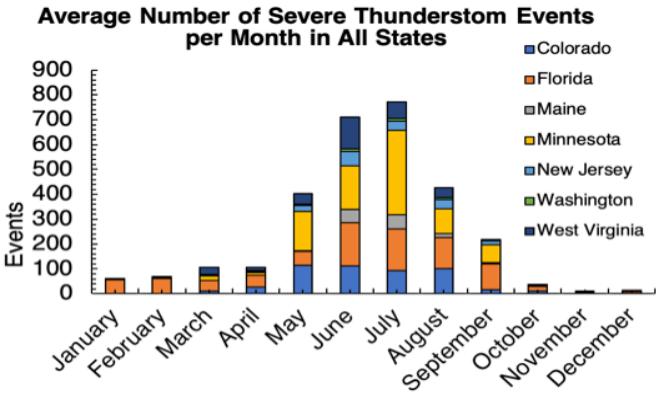

Figure 1. Summary of monthly severe storm events.

RESULTS

We collected data for seven states across the U.S: Colorado, Florida, Maine, Minnesota, New Jersey, Washington, and West Virginia. These states were chosen to represent a broad array of climates and geographical locations (**Figure 1**). For each of the seven states, severe thunderstorm events were recorded by month, and the averages were determined for the three years chosen (2000, 2008, and 2017). In all states, over 60% of the severe thunderstorm events occurred between May and August, with the summer months (June, July, and August) having the highest average severe thunderstorm events (**Table 1**). This was true for Colorado, Florida, Minnesota, Washington, and West Virginia. There was a significant difference between the monthly averages from each state over the years 2000, 2008, and 2017 (*p*-value=0.003, F=3.5) (**Table 2**).

Severe thunderstorm events occurred in winter months in Colorado, New Jersey, Washington, and Florida (**Figures 2-4**). Colorado observed three lightning related events in February of 2000 and 2008 (**Figure 2**). New Jersey received severe thunderstorm events in February of 2017 (seven total) and December of 2000 (two total), skewing the monthly average over the three years and reflected in the standard error bars (**Figure 4**). Washington also had tornadic events in winter months, specifically in January (one in 2008 and one in 2000), as well as five severe thunderstorm events not related to tornadic events (**Figure 4**). Florida received an average of 56.7 and 61 severe thunderstorm events

Table 1: Severe thunderstorm event monthly data for all states

Groups	*Sum*	*Average*	*Standard Error (SE)*	*% storms May-Aug*
Colorado	486.7	40.6	14.1	86.6
Florida	865.7	72.1	16.6	60.2
Maine	138.7	11.6	6.1	94.2
Minnesota	874.7	72.9	30.4	88.3
New Jersey	194.0	16.2	5.3	79.2
Washington	45.0	3.8	1.3	84.4
West Virginia	331.3	27.6	10.8	82.2

Table 2: One-way ANOVA table of monthly average data for all states across all three years (*p*-value = 0.003; F = 2.22)

Source of Variation	*SS*	*df*	*MS*	*F*	*P-value*	*F critical*
Between Groups	57377.3478	6	9562.8913	3.52972011	0.00386786	2.21881674
Within Groups	208612.186	77	2709.24917			
Total	265989.534	83				

respectively for January and February over the three years examined (**Figure 2**).

DISCUSSION

In this study, we classified lightning seasons in all states observed, with the most severe thunderstorm events occurring in May, June, July, and August. Colorado, New Jersey, Washington, and West Virginia were found to have severe thunderstorm events in the winter, which could be explained by increased winter storms due to climate change (1).

Lightning and thunderstorms occur in every state in the US. With climate change increasing the frequency of severe thunderstorms, it is important to quantify when lightning seasons occur to remain safe while outdoors (8). We hypothesized that the late spring and summer months (May, June, July, and August) would have the most frequently reported severe thunderstorm events in every US state due to the higher annual temperatures that occur in the Northern Hemisphere during these months. We also hypothesized that there would be severe thunderstorm events occurring in late fall or winter months that could be attributed to climate change, and that thundersnow events would occur in Colorado, where thundersnow storms have been previously reported (2).

Severe thunderstorm events seem to be most frequent during the months of May, June, July, and August. This is likely due to the convective available potential energy (CAPE), which is created in warmer climates (1). Since the late spring (May) and summer (June, July, and August) months are typically the warmest months of the year for all regions of the US, these months were expected to have the most frequent severe thunderstorm events. Though this was true, there were also reports of severe thunderstorms in winter months as well, which could be driven in part by climate change (1). Because Colorado has been known to have thundersnow, we wanted to examine whether thundersnow events would increase the severe thunderstorm event averages in winter months. Though we could not conclude that the severe thunderstorm events seen in the winter in Colorado were from thundersnow events, Colorado, New Jersey, Washington, and West Virginia all observed severe thunderstorm events in winter months. New Jersey received the largest number of severe thunderstorm events in winter months (December through February) with an

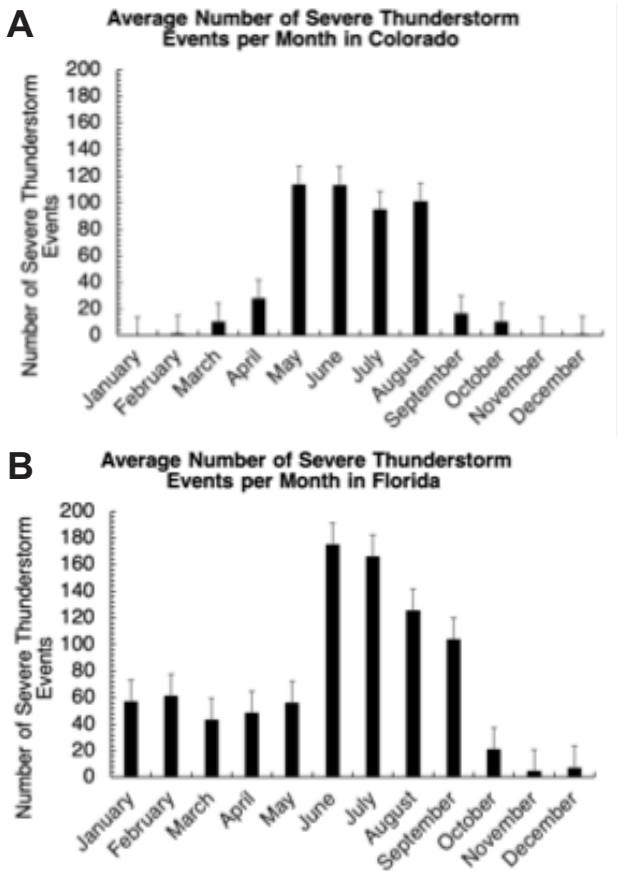

Figure 2. Severe thunderstorm events in Colorado and Florida. **(A)** Average number of severe thunderstorm events per month in Colorado. Mean of 40.56 storm events per month. Standard error of 14.1. **(B)** Average number of severe thunderstorm events per month in Florida. Mean of 72.139 reports per month. Standard error of 16.6.

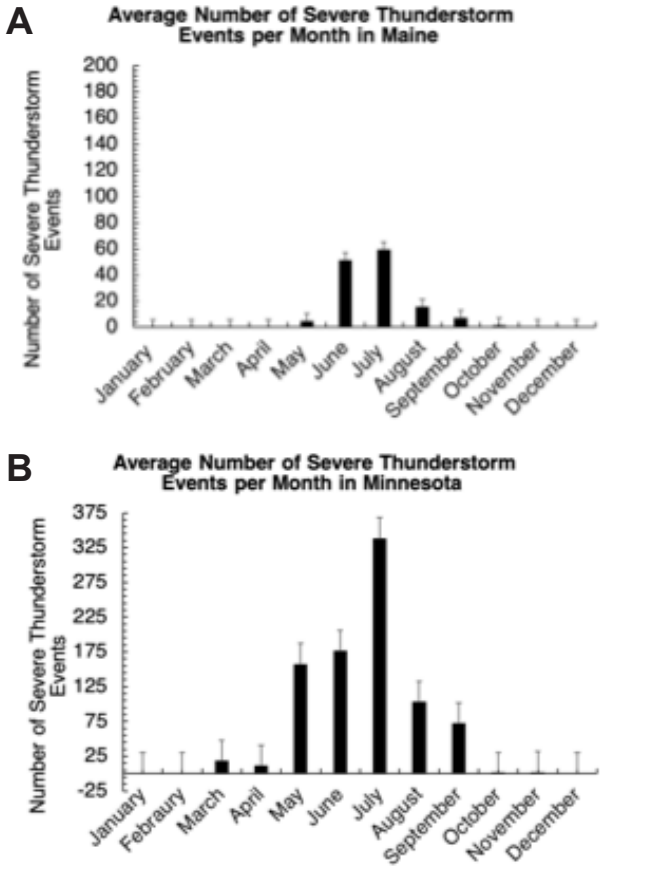

Figure 3. Severe thunderstorm events in Maine and Minnesota. **(A)** Average number of severe thunderstorm events per month in Maine. Mean of 11.55 reports per month. Standard error of 6.1. **(B)** Average number of severe thunderstorm events per Month in Minnesota. Mean of 72.89 reports per month. Standard Error of 30.4.

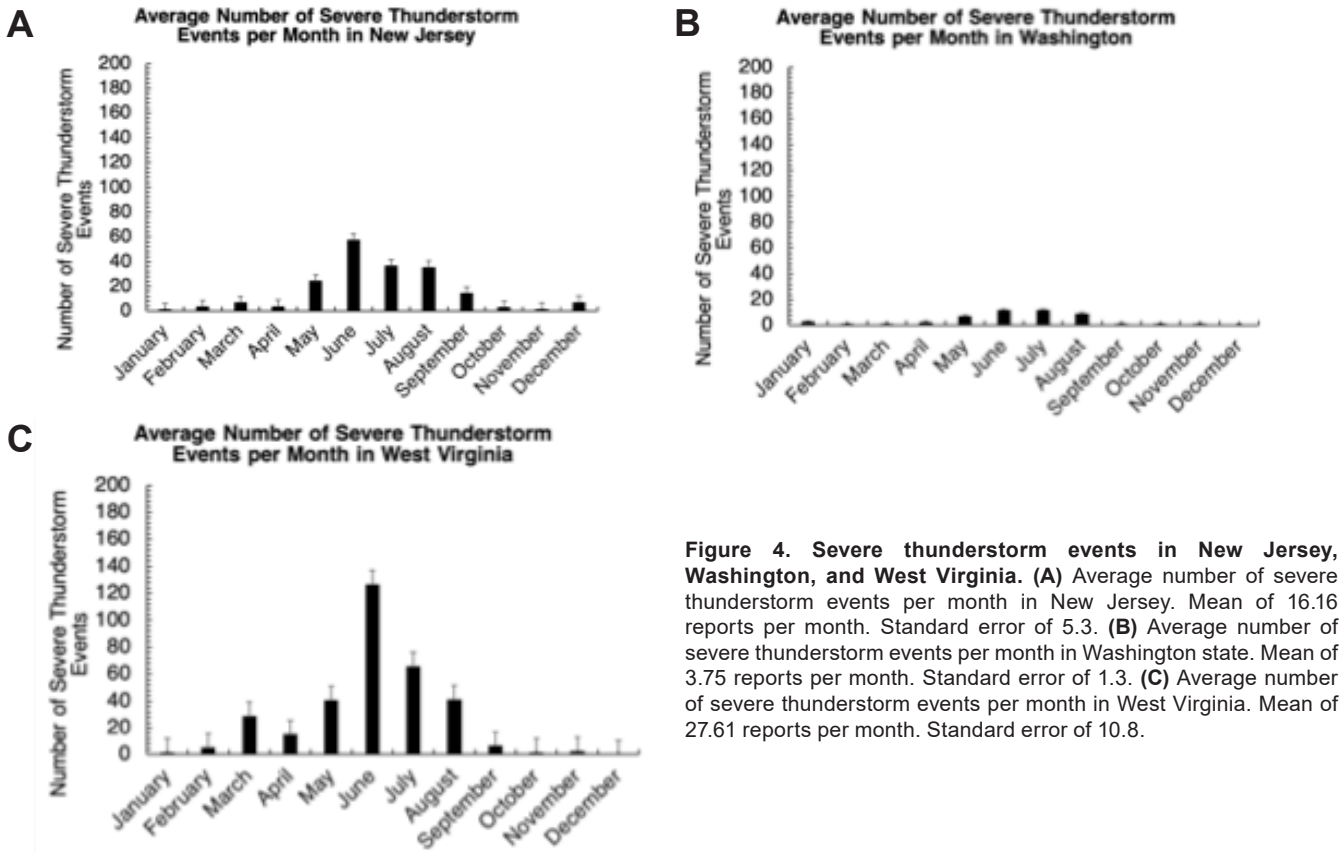

Figure 4. Severe thunderstorm events in New Jersey, Washington, and West Virginia. (A) Average number of severe thunderstorm events per month in New Jersey. Mean of 16.16 reports per month. Standard error of 5.3. **(B)** Average number of severe thunderstorm events per month in Washington state. Mean of 3.75 reports per month. Standard error of 1.3. **(C)** Average number of severe thunderstorm events per month in West Virginia. Mean of 27.61 reports per month. Standard error of 10.8.

average total of 11.33, although this is still much less than the summer months' average of 129.33. Washington's severe thunderstorm events in the winter were from tornadic events, which could also be driven by increased temperatures due to climate change (1).

Start and end dates to lightning seasons in each state varied, as was determined by data collected from the NOAA database. Colorado's lightning season was assigned from May to August; these months had the highest average severe thunderstorm events, most likely due to the number of tornadoes seen in the late spring. As Colorado falls partially into the Plains region of the US, it is more prone to tornadoes than most states, which can explain the late spring severe thunderstorm events (9).

Florida's lightning season was assigned from June to September. Florida was moderately active with severe thunderstorm events for almost every month of the year except the late fall and early winter months (October, November, and December). The most active months in Florida were June, July, August, and September. The amount of severe thunderstorm events in September can be explained by Florida's propensity to get hit by tropical storms and hurricanes during early fall, which were counted as severe thunderstorm "related" events (6). The activeness of storms throughout most of the year in Florida can be explained by the subtropical environment of the state, which allows for high to moderate temperatures throughout every season (6).

Maine's lightning season was assigned from June to July. Its relative inactivity as compared to other states can be explained by its geographical location, since it is one of the northernmost states in the US. (7). Therefore, its winters are longer and summers are briefer (7).

Minnesota's lightning season was assigned from May to September. Minnesota had the highest reported number of severe thunderstorm events, with a monthly average of 337.67 for July (over all three years). Given that Florida is known as the "Lightning Capital of the U.S," it is surprising that Minnesota surpassed Florida during a peak lightning month. Minnesota is very active because of its Northern position and extremely cold weather; it is also situated in the prairie biome that gathers moisture from the many lakes in the state (8).

New Jersey's lighting season was assigned from June to August. New Jersey was a relatively inactive state, with the most active months including June, July, and August. This can be explained by its temperate climate and rolling hills, which make it hard for severe weather phenomena such as tornadoes to strongly form (10).

Washington's lighting season was assigned from June to July. Washington had less severe thunderstorm events than New Jersey, making it the least active state of the states examined; June and July were its most active months. Washington's inactivity can be explained by its

temperate climate and geographical location, lying within the Cascade Mountain range. Its temperature remains fairly cool throughout the majority of the year, ranging from the low 40s °F to the mid-60s °F (11).

Lastly, West Virginia was a moderately active state, with its lightning season ranging from May to August. Its activity can be explained by its location (Southeast), which receives greater temperatures than New Jersey, Maine, Minnesota, Colorado, and Washington. This is because of the state's proximity to the equator, allowing the warmer temperatures to form the cumulus clouds that create thunderstorms (1). West Virginia also borders the Midwestern states that receive severe weather due to their climate (12).

Overall, the monthly severe thunderstorm event averages (across all years) from all seven states were significantly different from each other, as revealed by a one-way ANOVA. This rejects our hypothesis that there would be no difference between the monthly averages of all seven states. This was most likely due to their differing geographic locations and importance.

Lightning safety continues to remain a concern, as severe thunderstorm events are likely to increase in coming years due to climate change (1). In this study, we assigned lightning seasons to seven states in the US, all of which differ in geography and climate. Future studies will continue to assign lighting seasons to the remaining states. Repeating this collection over many years recorded in the NOAA database could also make up for any variation in the data, given that only three years were looked at. Lighting seasons could potentially vary with a larger sample size. We also plan to look at countries with similar climates and topography to understand how lightning seasons may differ from the US. With global change comes changing weather. Understanding how lightning seasons are changing over time could help us educate the public and prevent lightning-related injuries or death.

MATERIALS AND METHODS

Collecting Data

The data presented in the study was collected from the NOAA Storm Events Database. Data collected from the database consisted of severe thunderstorm events such as thunderstorm with wind and hail, tornados, funnel clouds, lightning, hurricanes, tropical storms, and tornadic waterspouts. We collected data for three years (2017, 2008, and 2000) for each of the following states: Colorado, Florida, Maine, Minnesota, New Jersey, Washington, and West Virginia, and categorized them by county and month of the year. The years 2017, 2008, and 2008 were chosen as a representative sampling of the past two decades. Climates differed greatly between the chosen states, representing the following biomes: temperate deciduous forest (New Jersey, West Virginia, Maine, parts of Florida, parts of Minnesota), coniferous forest (Washington, parts of Florida), prairie grassland (parts of Minnesota, parts of Florida), savannah (parts of Florida), and alpine tundra (Colorado).

Determining Lightning Seasons

The total number of severe thunderstorm events for each state was collected and broken down by month and year. We determined the mean severe thunderstorm events per month (over years selected) by calculating the sum of severe thunderstorm events for each month (in each year) and dividing the total by three (for the three years examined). A histogram was created to depict the average number of severe thunderstorm events over the three years by month. The average number of severe thunderstorm events for each state was used to determine lightning seasons.

Statistical Analyses

We assessed the counties of each state to determine the highest average annual severe thunderstorm events over the three years chosen. A one-way ANOVA was performed on the severe thunderstorm data from all seven states (an average per month). For statistical analysis, we applied a *p*-value of 0.05 as the threshold for significance. Data analyses were performed using Google Sheets. We also calculated the percentage of average severe thunderstorm events that occurred in May, June, July, and August, the months that we hypothesized would have the most events.

ACKNOWLEDGEMENTS

We would like to thank the Summit Public Schools Board of Education office for providing us with the opportunity to do this research. Thanks to Christine Stelmach, Tom O'Dowd, and Stacy Grimaldi for your guidance and support on this project.

Received: June 11, 2019
Accepted: July 24, 2020
Published: September 7, 2020

REFERENCES

1. Romps, DM., Seeley, Jacob T, Vollaro, D, and M John. "Projected increase in lightning strikes in the United States due to global warming." *Science*, vol. 245, no. 6211, 2014, pp. 851-854, DOI: 10.1126/science.1259100.
2. "Lightning Emergency Management." *Florida State University.*
3. "Storm Data Publication". *NOAA Storm Data Publication Database.*
4. Kumjian, MR and D Wiebke. "Analysis of Thundersnow Storms over Northern Colorado". *Weather & Forecasting*, vol. 30, no. 6, 2015, pp. 1469-1490. doi:10.1175/waf-d-15-0007.1
5. Ferry, D. "The World's 10 Biggest Lightning Hot Spots" *Outside Online.* 2016. https://www.outsideonline.com/2080701/worlds-10-biggest-lightning-hot-spots.

6. Sandlin, L. “Storm Kings: America’s First Tornado Chasers”. *Severe Weather 101- Lightning Basics.* Pantheon Books, 2013.
7. Shultz, C. “Lightning Mapping Arrays”. *The Wide World of SPoRT.* 2019. https://nasasport.wordpress.com/category/lightning-mapping-array/
8. Spring, J. “Lightning Deaths and Injuries, by the Numbers”. *Outside Online.* 2013. https://www.outsideonline.com/1912401/lightning-deaths-and-injuries-numbers.
9. “Weather Safety Preparedness.” *US Department of Commerce, NOAA, National Weather Service.*
10. Norrell, RJ. and Fuson, RH. “Florida”. *Brittanica.* https://www.britannica.com/place/Florida.
11. Muskie, ES, Cole, JN and ED Ross. “Maine”. *Brittanica.* https://www.britannica.com/place/Maine-state.
12. Gustafson, NC and JS Adams. “Minnesota”. *Brittanica. https://www.britannica.com/place/Minnesota.*

JOURNAL OF
EMERGING INVESTIGATORS

Article

Variations in Heat Absorption and Release of Earth Surfaces During Fall in Laramie, Wyoming

Padmalakshmi Ramesh[1] and Ramesh Sivanpillai[2]
[1] Laramie Middle School, Laramie, WY 82072, USA
[2] Wyoming GIS Center, University of Wyoming, Laramie, WY 82071, USA

SUMMARY

All Earth surfaces absorb heat at different rates and release it afterwards. If surfaces release less heat than they absorb, they will remain warmer. Heat retained by man-made surfaces and human activities are the two major contributors of the Urban Heat Island (UHI) effect witnessed in cities worldwide. Though the effects of UHI are well studied in summer and winter months, UHI effects are not widely studied in other seasons and smaller cities. We conducted this study to document the contributions of man-made surfaces in Laramie, Wyoming to the UHI effect. Heat absorption and release by five surfaces were measured in the autumn of 2018. We hypothesized that heat retention by all surfaces will vary throughout the fall season due to differences in ambient air temperature. We recorded temperatures of man-made and natural surfaces at early morning, mid-afternoon, and evening using an infrared thermometer. Results from this study showed that man-made surfaces retained more heat in fall than natural surfaces. The amount of heat retained by all surfaces was higher in early fall and less in late fall. Presence of smoke, haze, snow, and clouds altered the pattern of heat absorption and release. Future studies could expand to other cities, include more surfaces, and measure temperature more frequently to estimate their contribution to UHI.

INTRODUCTION

Earth surfaces absorb energy emitted by the sun in the form of electromagnetic (EM) waves. These surfaces then convert the absorbed energy to heat, which increases their temperature, and release the energy later in the day or throughout the night (1). For example, bare ground absorbs sunlight in the morning and early afternoon which raises its temperature. Later in the day, bare ground releases the absorbed energy and returns to its original temperature. This radiation inflow and outflow is expressed as the surface energy budget (Equation 1):

$$Q^* + Q_F = Q_H + Q_E + \Delta Q_S + \Delta Q_A \quad [1]$$

where Q^* is the net all-wave radiation, Q_F is the heat released by combustion, Q_H is the sensible heat flux density, Q_E is the latent heat flux density, ΔQ_S is the net heat storage, and ΔQ_A is the net heat advection (2). The net all-wave radiation, Q^*, is estimated using Equation 2:

$$Q^* = K\downarrow - K\uparrow + L\downarrow - L\uparrow \quad [2]$$

where, $K\downarrow$ and $L\downarrow$ is the incoming short-wave and long-wave radiation respectively, $K\uparrow$ is the reflected short-wave radiation, and $L\uparrow$ outgoing long-wave radiation, which can be emitted and reflected by earth surfaces.

Natural surfaces such as bare ground, rocks, and vegetation release most of what they absorbed during the course of the day (3, 4). However, many man-made or built surfaces such as asphalt roads, cement sidewalks, parking lots, building roofs, steel skyscrapers, etc. release less heat than what they absorbed. This results in man-made surfaces retaining more heat, so they are relatively warmer than natural surfaces later in the day (3, 4). For example, if a surface has a starting temperature of 10 ˚C, gains 10 ˚C during the course of a day, and loses only 8 ˚C in the evening, its resulting temperature will be warmer than its starting value. Also, if man-made surfaces release less heat at night, the next day they tend to be warmer. If this process continues every day, the overall temperature of the surface will increase over a course of time.

In urban areas, natural surfaces such as bare ground and vegetation are replaced by buildings, roads, sidewalks etc. Vegetation cools the Earth's surface through a process known as evapotranspiration (4, 5). At higher temperatures, plants and trees release water through their stomata to cool themselves. This process is termed as evapotranspiration, and it cools the surrounding area (6). With less evapotranspiration, urban areas trap more heat. When more and more natural surfaces are replaced by urban infrastructure, this phenomenon is worsened. In addition to these man-made infrastructures, urban areas also generate heat from automobiles, people, industries, etc. (5). This heat is trapped in the lower levels of the atmosphere (3). As a result, urban areas retain more heat than surrounding rural areas during night time (7). This phenomenon is termed as Urban Heat Island (UHI) (4, 5, 7, 8). UHI is a problem for most cities around the world. When cities are warmer during night than surrounding rural areas, it can cause the morning (or starting) temperature to be warmer the next day. If this process continues, cities will be warmer than rural areas. As cities get warmer, the residents will use more energy to cool themselves. This increased energy usage contributes more heat to the ecosystem. This can impact many fragile ecosystems. Densely populated

cities with more activities experience a higher UHI effect.

Previous studies have analyzed UHI effects and reported that this phenomenon is prevalent in many major cities throughout the world (9-11). According to a study published in 2015 (12), the following 5 US cities exhibited the most intense UHI effect: Salt Lake City, Miami (FL), Louisville, Los Angeles, and Las Vegas. Many studies have reported warmer night time temperatures in summer and winter months (10) but fewer studies have reported the pattern in autumn.

Further, not many studies have been conducted in small cities and towns to quantify the effects of UHI because they do not have many buildings and smaller population. These small urban areas can also experience the similar problems that are faced by large metropolitan areas. The combined contribution of these small cities and towns can be equivalent to several large ones. Therefore, we must study the effects of UHI in smaller cities and towns.

The objective of this study was to determine if natural and man-made Earth surfaces in Laramie, Wyoming absorbed and released heat differently during the 2018 fall season. Laramie is a small city in Wyoming (USA) with a population of approximately 32,479 (2018 estimate). We hypothesized that heat retention by surfaces will vary throughout the fall season, since the ambient air temperature will be higher in early in comparison to late fall.

RESULTS

Surface temperatures were measured in weeks 1, 2, 3, 5, 8, 12, 13, of the fall 2018 season, totaling seven weeks. No readings were recorded for the rest of the weeks since the study area was covered by ice/snow or it rained.

Smoke and haze from wildfires covered the city of Laramie in weeks one and two, which reduced the amount of sunlight reaching the surfaces (13). Clouds and smoke have similar effects, since they are made up of small particles that reflect incoming light(14). In week eight, there were thick clouds, and light snow was present on most of the surfaces. Thus, these three weeks were termed as anomalous, since the amount of heat absorbed and released was affected by the weather conditions. The rest of the weeks were considered as normal. After the data were grouped into normal and anomalous, the mean was calculated for each surface every week.

Further data were split into early and late fall, since the air temperature was higher at the start of the season (15.2 ˚C) than at the end (-4.5˚C). In early fall, the sun's rays reach the earth at a steeper angle, while in the later part of this season the rays reach at a shallower angle. This causes warmer air temperatures in early fall (15).

Normal Weeks

(i) Early fall (Weeks 3 and 5)

At the start of the day, the average temperature of each surface was lower than two degrees Celsius **(Table 1**). At 1 pm, their temperature reached above mid-twenty degrees Celsius. By 7 pm, temperatures of the surfaces did not return to their starting values. Grass lawn was the closest to its starting temperature **(Table 1).** Standard deviation values were highest for cement sidewalk at 1 pm (most variation within the surface), and the lowest value was for pebbles at 7 am (the least variation).

Surface	Average temperature (Standard deviation)		
	7 am	1 pm	7 pm
Pebbles (n=7)	-1.2˚C (0.80)	33.7˚C (2.30)	6.8˚C (1.64)
Bare ground (n=7)	-1.3˚C (1.17)	28.6˚C (1.44)	7.0˚C (0.96)
Asphalt road (n=7)	1.8˚C (1.32)	29.9˚C (1.86)	11.6˚C (1.05)
Cement sidewalk (n=7)	0.8˚C (1.00)	26.9˚C (2.73)	12.1˚C (2.18)
Grass lawn (n=7)	-1.3˚C (1.00)	27.6˚C (2.28)	1.5˚C (1.03)

Table 1: Temperature and standard deviation values during normal weeks in early fall. Average temperature and standard deviation values measured at 7 am, 1 pm and 7 pm in early fall (weeks 3 and 5) under clear weather conditions. Temperature values were measured at 7 locations for each of the five surfaces, and their average and standard deviation values were computed.

Results from the *t*-test with Bonferroni corrected alpha value of 0.0167, indicated that the average temperature measured for pebbles, asphalt road, and cement at 1 pm was significantly higher ($p < 0.001$) than their 7 am values. Similarly, the average temperature of each surface dropped by 7 pm, and that value was significantly lower ($p < 0.001$) than 1 pm. The 7 am and 7 pm temperatures were significantly different ($p < 0.001$).

The average maximum air temperature for the normal early fall weeks (3 and 5) was 12.8˚C. Pebbles and bare ground absorbed and released different amounts of heat but retained approximately similar amounts **(Figure 1a).** Pebbles gained 34.9˚C and released 26.9˚C, and bare ground gained 29.9 ˚C and released 21.6 ˚C. The net heat gain of pebbles was 8.0˚C and bare ground was 8.3˚C.

Among man-made surfaces, asphalt road absorbed and released the most heat **(Figure 1a)**. Asphalt gained 28.1˚C in the AM and lost 18.3˚C in the PM. Asphalt's net heat gain was 9.8˚C. For cement sidewalk, the absorption was 26.1˚C and the release was 14.8˚C, resulting in a net gain of 11.3˚C. Among the two man-made surfaces, cement sidewalk retained the most heat at the end of the day.

Grass lawn released nearly as much heat as it absorbed **(Figure 1a).** Grass lawn gained 28.9 ˚C (AM gain) and lost 26.1 ˚C (PM loss) resulting in a net heat gain of 2.8 ˚C.

(ii) Late fall (Weeks 12 and 13)

At the start of day, the average temperature of each surface was below 0˚C **(Table 2).** At 1 pm, surface temperatures did not exceed 8˚C. Surface temperatures at 7 pm were very close to their respective starting values at 7 am. Standard deviation values were highest for pebbles at 1 pm (most variation within this surface), and the lowest value was

for cement sidewalk at 7 pm (least variation). The variation in the temperature readings **(Table 2)** was higher in late fall in comparison to the corresponding values in early fall **(Table 1).**

Surface	Average temperature (Standard deviation)		
	7 am	1 pm	7 pm
Pebbles (n=7)	-10.5˚C (4.05)	5.6˚C (5.40)	-10.2˚C (2.99)
Bare ground (n=7)	N/R	N/R	N/R
Asphalt road (n=7)	-10.2˚C (3.38)	7.7˚C (3.05)	-10.0˚C (2.88)
Cement sidewalk (n=7)	-11.3˚C (3.45)	4.5˚C (4.42)	-8.0˚C (2.37)
Grass (n=7)	N/R	N/R	N/R

NOTES: N/R – Not recorded

Table 2: Temperature and standard deviation values during normal weeks in late fall. Average temperature and standard deviation values measured at 7 am, 1 pm and 7 pm in late fall (weeks 12 and 13) under clear weather conditions. Temperature values were measured at 7 locations for each of the five surfaces, and their average and standard deviation values were computed.

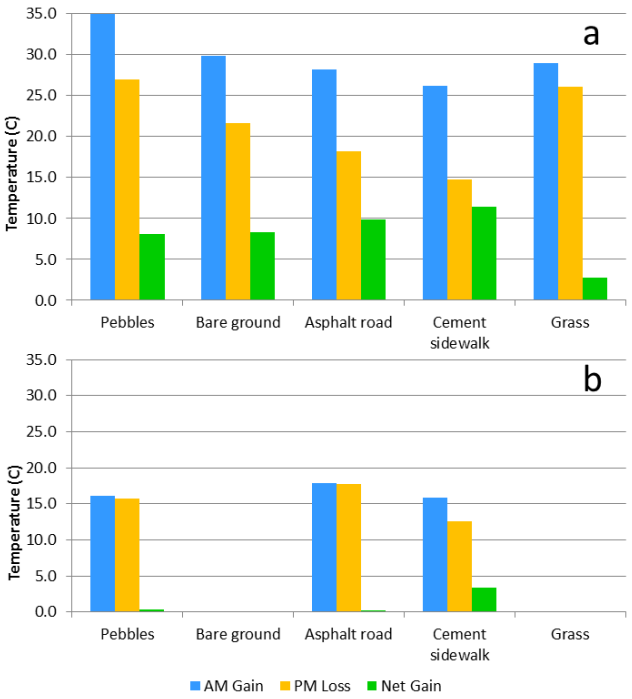

Figure 1: Heat gained, released, and retained by five surfaces in early (a) and late (b) fall. The heat gained (blue bar) between 7 am and 1 pm and released (yellow bar) between 1 pm and 7 pm shows that man-made surfaces (asphalt road and cement sidewalk) retained more heat (green bar) than the natural surfaces and grass lawn. In late fall only cement sidewalk retained some heat that it gained during the day. No readings were taken for bare ground and grass since they were covered in snow.

Results from the *t*-test indicated that the average temperature measured for each surface at 1 pm was significantly higher ($p < 0.001$) than their 7 am values. Similarly, the average temperature of each surface dropped by 7 pm, that value was significantly lower ($p < 0.001$) than 1 pm. However, the 7 am and 7 pm values were not significantly different ($p < 0.05$) for asphalt and pebbles. For cement sidewalk, the values were still significantly different ($p < 0.01$).

The average maximum air temperature for the normal late fall weeks was 3.6 ˚C. Among the natural surfaces, readings were measured only for pebbles since bare ground was covered by snow. Pebbles absorbed 16.1˚C and released 15.8˚C, thus retaining 0.3˚C **(Figure 1b).**

Among the man-made surfaces, cement sidewalk had the highest net heat gain. Asphalt's AM gain and PM loss was 17.9˚C and 17.7˚C, respectively. Asphalt's net heat gain was 0.2˚C. For cement sidewalk, the absorption was 15.8˚C and its release was 12.5˚C; resulting in a net heat gain of 3.3˚C **(Figure 1b)**.

No readings were taken for grass lawn as the surface was covered by snow.

Anomalous Weeks

(i) Early fall (Weeks 1 and 2)

Surface	Average temperature (Standard deviation)		
	7 am	1 pm	7 pm
Pebbles (n=7)	4.3˚C (1.24)	34.0˚C (2.18)	15.1˚C (0.89)
Bare ground (n=7)	6.7˚C (0.70)	33.8˚C (1.08)	15.8˚C (0.61)
Asphalt road (n=7)	10.2˚C (0.58)	32.7˚C (0.82)	19.6˚C (0.39)
Cement sidewalk (n=7)	7.9˚C (0.77)	27.6˚C (2.43)	19.1˚C (0.82)
Grass (n=7)	1.8˚C (1.16)	25.1˚C (2.69)	9.2˚C (1.54)

Table 3: Temperature and standard deviation values during anomalous weeks in early fall. Temperature and standard deviation values during anomalous weeks in early fall. Average temperature and standard deviation values measured at 7 am, 1 pm and 7 pm in early fall (weeks 1 and 2) under smoke and hazy conditions. Temperature values were measured at 7 locations for each of the

The average maximum air temperature for the early fall weeks with smoke and haze was 24.2˚C. Smoke and haze from a wildfire near the study area were present in weeks 1 and 2. The amount of sunlight that reached the surfaces was limited due to the presence of smoke (12).

Among natural surfaces, pebbles had the highest absorption and release. Pebbles' AM gain was 29.7˚C and their PM loss was 18.9˚C. The net heat gain was 10.8˚C **(Figure 2).** For bare ground, the absorption was 27.1˚C and its release was 18.0˚C. Bare ground's net heat gain was 9.1˚C **(Figure 2).**

Among man-made surfaces, asphalt had the highest absorption and release. For asphalt, the AM gain was 22.5˚C and its release was 13.1˚C. Asphalt's net heat gain was 9.4˚C **(Figure 2)**. For cement sidewalk, the absorption was 19.7 ˚C; the release of cement sidewalk was 8.5˚C. Cement sidewalk's net heat gain was 11.2˚C **(Figure 2).**

Unlike weeks 3 and 5 (clear conditions), grass lawn did

not release as much heat as it absorbed under smoke and haze conditions. The AM gain was 23.3˚C and the PM loss was 15.9˚C. Grass lawn's net heat gain was 7.4˚C **(Figure 2).**

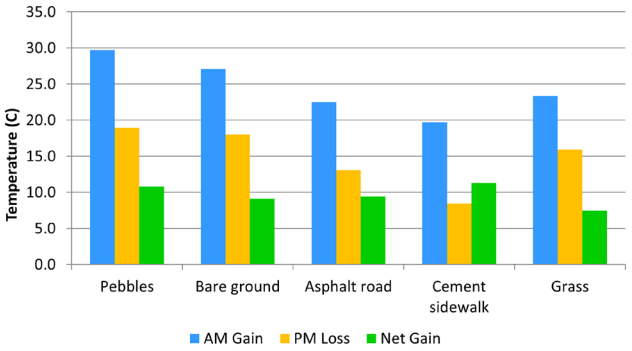

Figure 2: Heat gained, released, and retained by five surfaces in early fall under smoke and hazy conditions. The heat gained (blue bar) between 7 am and 1 pm and released (yellow bar) between 1 pm and 7 pm shows that pebbles and cement sidewalk retained more heat (green bar) than the rest of the surfaces. Man-made surfaces gained less heat than the natural surfaces.

(ii) Late fall (Week 8)

Surface	Average temperature (Standard deviation)		
	7 am	1 pm	7 pm
Pebbles	-6.9˚C (1.26)	4.9˚C (0.93)	-16.4˚C (1.26)
Bare ground	-10.6˚C (1.59)	2.8˚C (0.53)	-9.0˚C (0.99)
Asphalt road	-4.6˚C (1.45)	6.0˚C (0.45)	-12.1˚C (0.53)
Cement sidewalk	-4.9˚C (1.37)	5.1˚C (0.81)	-9.1˚C (0.30)
Grass	-10.1˚C (0.47)	0.6˚C (1.64)	-13.6˚C (1.60)

Table 4: Temperature and standard deviation values during anomalous week eight. Average temperature and standard deviation values measured at 7 am, 1 pm and 7 pm in early fall (week 8) under heavy cloud cover and light snow conditions. Temperature values were measured at 7 locations for each of the five surfaces, and their average and standard deviation values were computed.

The maximum air temperature was -5.6 ˚C for the late fall week. In week 8, snow, cloud cover, and windy conditions were present, hence the air temperature was noticeably cooler than normal weeks (3 and 5). All surfaces, except bare ground, released more heat than what they absorbed.

Among natural surfaces, bare ground had the highest absorption and the lowest release. For bare ground, the absorption was 13.4˚C and its release was 11.8˚C. The net heat gain for bare ground was 1.6˚C **(Figure 3)**. Pebbles absorbed (AM gain) 11.8˚C, released 21.3˚C (PM loss), hence the net heat loss was 9.5˚C **(Figure 3).**

Among man-made surfaces, asphalt both absorbed and released the most heat. For asphalt, the absorption and release were 10.6˚C and 18.1˚C respectively. The net heat loss of asphalt was 7.5˚C. Cement sidewalk's absorption was 10.0˚C and its release was 14.2˚C. Cement sidewalk's net heat loss was 4.2˚C. Under snow, cloud cover, and windy conditions, cement sidewalk had the highest net heat gain in comparison to asphalt road **(Figure 3)**.

In week 8, grass lawn actually had the lowest net heat loss of 3.5˚C. The absorption and release were 10.7˚C and 14.2˚C, respectively.

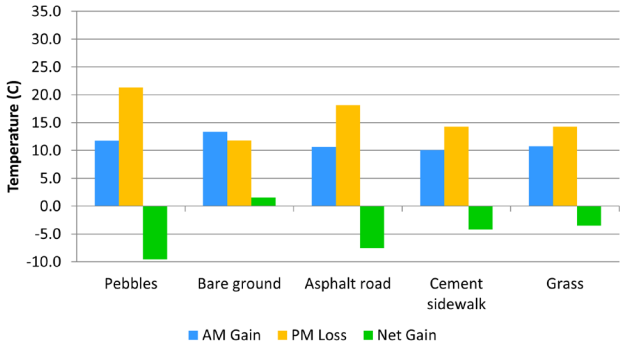

Figure 3: Heat gained, released, and retained by five surfaces on a cloudy day in late fall. The heat gained (blue bar) between 7 am and 1 pm and released (yellow bar) between 1 pm and 7 pm shows that all surfaces except bare ground released more heat than they absorbed.

DISCUSSION

This study shows that man-made features in Laramie, WY retained more heat during the first five weeks of fall 2018. Later in the fall season, the amount of heat retained by man-made surfaces was lower. This excess heat retained by these surfaces increases the ΔQ_S, the net heat storage in the surface energy budget equation. This study shows that man-made features in a small city are contributing to UHI in fall. This effect present in small urban areas may appear small, but when added up they could also have a big impact on a state's or region's UHI. Therefore, scientists should monitor smaller urban areas during fall season.

The results of this study support the hypothesis that man-made surfaces retain more heat than natural surfaces in the fall season. As hypothesized, there was also a variation in the amount of heat retained throughout the fall season. During normal early fall weeks, when the maximum ambient temperature was 12.8˚C, surfaces retained more heat than in late fall, when maximum ambient temperature was 3.6˚C.

The maximum ambient temperature for the first 2 weeks was much higher (24.2˚C), but the surface heat retention was only slightly higher than what was observed in weeks 3 and 5. The presence of smoke and haze in those weeks could have reduced the amount of incoming radiation.

In this study, cement sidewalk retained the most heat in all weeks except when all surfaces were covered by thick cloud cover and high winds (week 8). As reported by NASA, dark surfaces absorb almost all light and convert it into heat (16). The more light surfaces absorb, the more heat they emit. Lighter surfaces, on the other hand, reflect almost all light, therefore they do not emit as much heat (16, 17). Man-made surfaces retained more heat than natural surfaces, due to the

materials present in them. Asphalt road, the darkest surface in this study, retained less heat than cement sidewalk, most likely due to its color. Cement sidewalk always absorbed the least amount of heat, but it released even less. Among all surfaces, cement sidewalk retained the most heat.

Natural surfaces released most of the energy they absorbed. Pebbles released most of the heat they absorbed. Bare ground, which is a lighter surface, had a higher net heat gain than pebbles. In summary, light colored cement sidewalk and bare ground retained relatively more heat than the corresponding darker surfaces in each category (16, 17). Grass lawn was always cooler than all other surfaces, except in anomaly week eight (snow, cloud cover, and windy conditions). Plants transpire and naturally cool the surrounding area. Hence, many cities are adapting to the idea of green roofs on buildings to reduce their UHI effect. This idea is that plants are planted on roofs to help maintain a cooler temperature.

In this study, there could have been some sources of error that could have influenced the outcome. One source of error could have been changes in the pattern of weather and shadows within a day. Small changes in temperature and other weather factors could have influenced the absorption of the surfaces. Shadows may be another source of error as they change throughout the day, due to the movement of the sun. Shadows would cool the area they are shading, which would influence the temperature reading. In this study, this was avoided these problems by selecting areas that were not surrounded by objects (parked vehicles, trees, road signs, and buildings) that would shade them.

On windy days, there will be a difference in the convection pattern (18). On non-windy days, heat rises vertically (convection), whereas on windy days the process occurs horizontally (advection,19). Advection does not allow surfaces to be heated as they normally would have under non-windy conditions. Therefore, on windy days multiple readings much be taken at each sample point and the average value must be recorded.

When smoke from nearby wildfires covered the study area in weeks 1 and 2, surfaces absorbed and released less energy. This was due to the absorption and scattering of incoming sunlight by aerosols present in the smoke (13). Under smoke and cloud conditions, less sunlight reached the surfaces.

To further confirm the findings of this study, additional readings must be taken in normal, windy, cloudy, and hazy conditions in fall season. Readings should also include a larger variety of surfaces of various colors and textures. Sites must be selected to avoid chances of being covered in shadows as an abundance of buildings, trees, fences, etc. in or near the site may affect the temperatures of the sample points. This study could be expanded to other cities and towns in Wyoming to further assess the contribution of man-made features to UHI.

MATERIALS AND METHODS

In 2018, the fall season started on September 22 and ended on December 21 (nasa.gov). The first and last readings were recorded on September 23 and December 16, respectively.

Five earth surfaces were selected for this study: bare ground and pebbles (natural), asphalt road and cement sidewalk (man-made), and grass lawn (live). Bare ground was a light brown color **(Figure 4a)** and pebbles were medium to dark shades of gray **(Figure 4b).** The asphalt road was dark grey in color **(Figure 4c),** and the cement sidewalk was light tan in color **(Figure 4d).** Grass was mostly green **(Figure 4e)** at the start of the fall season and gradually changed to yellow and light brown colors by the end of the season. These surfaces chosen were not shaded by trees, fences, buildings, parked vehicles, etc., and received more or less the same amount of sunlight each day during the study.

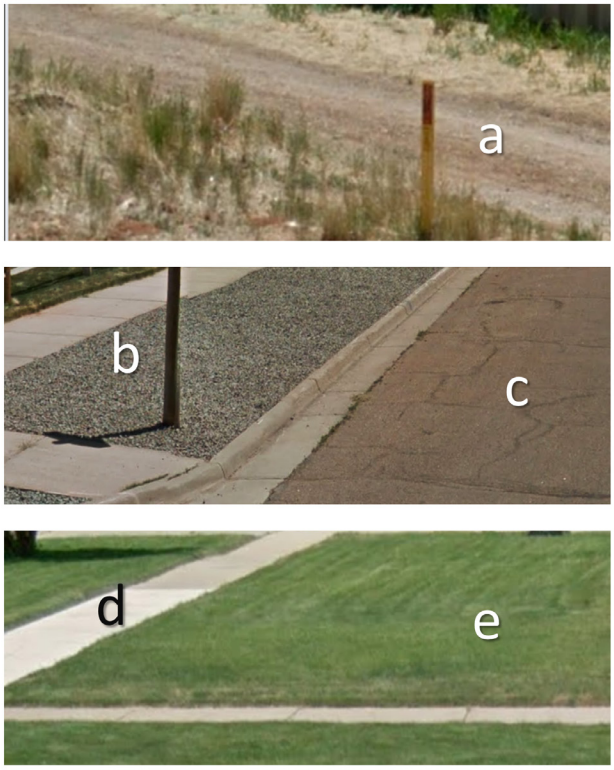

Figure 4: Natural and man-made surfaces included in this study. Two natural surfaces were light brown bare ground (a) and grey colored pebbles (b). Two man-made surfaces included dark grey asphalt road (c) and light colored cement sidewalk (d). Grass lawn (e) was the live surface.

Surface temperatures were measured using a Fluke© 63 Infrared Thermometer (Everett, WA). This thermometer is recommended by NASA's GLOBE program (20) and can accurately measure temperatures ranging from -32 ˚C to 535 ˚C (www.fluke.com). For measuring the temperature of any surface or object, this instrument has to be pointed towards it. The area in which the temperature is being taken will be

highlighted when the trigger is pressed. The digital display will show the temperature in either in Fahrenheit or Celsius, based on the user preference. This instrument was used to take readings on weeks 1, 2, 3, 5, 8, 12, and 13. No readings were taken during the rest of weeks when the weather conditions were windy, cloudy, snowy, etc.

Sundays were selected as sampling days. On that day, the first set of temperature readings was recorded shortly before sunrise, approximately between seven and eight AM. Prior to the reading, the starting time, along with the air temperature and weather conditions were recorded. One of the five surfaces was randomly selected, and its temperature was measured at 7 different locations that were at least 0.5 m apart. This step was repeated for the remaining four surfaces. After all readings were recorded (7 locations x 5 surfaces = 35 readings), the ending time was noted. The second and third set of temperature readings for each sampling day were taken after six hours (between 1 and 2 PM) and twelve hours (between 7 and 8 PM) starting from the first reading, respectively. At the end of a sampling day, we collected 105 readings/sampling day (35 readings x 3 times/day). The day-time high temperature for each observation day was recorded from the Weather Underground (21).

During weeks 1 – 3, 5, and 8 readings were recorded for all five surfaces. However, in weeks 12 and 13, readings were not recorded for bare ground and grass lawn because they were covered in snow and ice.

For each surface, average temperature and standard deviation values were calculated for morning (7 am), afternoon (1 pm), and evening (7 pm) values using Microsoft Excel™. This step was repeated for the remaining surfaces. Temperature measurements were compared for a) increase (between 7 am and 1 pm), b) decrease (between 1 pm and 7 pm), and c) net gain (between 7 am and 7 pm) using one tailed *t*-test. Since three comparisons were made with the temperature measurements we applied Bonferroni correction to the alpha value of 0.05:

$$\alpha_{corrected} = \alpha/c \quad [3]$$

where, α = 0.05, and c= 3 (number of comparisons). Bonferroni correction reduces the likelihood of reporting significant results by chance alone. In this study we used the adjusted alpha value of 0.01667. This test showed whether the afternoon temperature for each surface was statistically different from its morning or evening temperatures.

The average temperature value measured at 7 am was subtracted from the average value measured at 1 pm and was termed as AM heat gain.

AM heat gain = Average afternoon temperature – Average morning temperature [4]

Similarly, the afternoon heat loss was termed as the difference between the afternoon and evening temperatures.

PM heat loss = Average afternoon temperature – Average evening temperature [5]

Difference between the morning heat gain and afternoon heat loss was termed as net heat gain or retained.

Net heat gain =AM heat gain – PM heat loss [6]

Average temperature value of each surface at 7 am, 1 pm, and 7 pm was used for estimating the AM gain, PM loss, and Net gain for each sampling day.

ACKNOWLEDGEMENTS

Thanks to Ms. Erin Stoesz, Wyoming State Science Fair Director, for suggesting and encouraging me to submit my sixth grade science project as a paper. I thank Ms. Morgan Krysl for helping me with my science fair project. I thank the JEI Managing Editor and reviewers for providing valuable comments and suggestions which improved the quality of this paper

Received: March 23, 2020
Accepted: August 22, 2020
Published: September 8, 2020

REFERENCES

1 Lindsey, Rebecca. *Climate and Earth's Energy Budget*. NASA Earth Observatory, 14 Jan. 2009, earthobservatory.nasa.gov/features/EnergyBalance. Accessed 29 Mar. 2020.

2 Oke, T. R. "The Urban Energy Balance." *Progress in Physical Geography: Earth and Environment*, Vol. 12, no. 3, 1988, pp: 471-508. DOI: 10.1177/030913338801200401.

3 Urban Heat Islands. *UCAR*, 2011, scied.ucar.edu/longcontent/urban-heat-islands. Accessed 29 Mar. 2020.

4 What is an Urban Heat Island? *NASA Climate Kids*, 28 Jan. 2020, climatekids.nasa.gov/heat-islands/. Accessed 29 Mar. 2020.

5 Magee, N et al. "The Urban Heat Island Effect at Fairbanks, Alaska." *Theoretical and Applied Climatology,* Vol 64, 1999, pp 39-47.

6. Allen, Richard G., et al., "Satellite-based energy balance for mapping evapotranspiration with internalized calibration (METRIC)-model." *Journal of Irrigation and Drainage Engineering,* vol. 133, no. 4, 2007, pp380-394.

7 Learn About Heat Islands. *EPA,* 21 Nov. 2019, www.epa.gov/heat-islands/learn-about-heat-islands. Accessed 29 Mar. 2020.

8 Phelan, Patrick, et al. "Urban Heat Island: Mechanisms,

Implications, and Possible Remedies." *Annual Review of Environment and Resources,* vol. 40, no. 1, 2015, pp. 285-307.

9 Taha, Haider, et al. "Residential cooling loads and the urban heat island – the effects of albedo." *Building and Environment,* vol. 23, no. 4, 1988, pp: 271-283.

10 Tan, Jianguo, et al. "The urban heat island and its impact on heat waves and human health in Shanghai." *International Journal of Biometeorology,* vol. 54, 2010, pp: 75-84.

11 Kolokotroni, M, et al. "The effect of the London urban heat island on building summer cooling demand and night ventilation strategies." *Solar Energy*, vol. 80, no. 4, 2006, pp: 383-392.

12 Debbage, Neil J., and Marshall Shepherd. "The urban heat island effect and city contiguity." *Computers, Environment and Urban Systems*, Vol 54, 2015, pp. 181-194.

13 Brown, Josh and Joe Atkinson, "Smoke from wildfires can have lasting climate impact." *NASA*, https://climate.nasa.gov/news/2597/smoke-from-wildfires-can-have-lasting-climate-impact/. Accessed 3 July 2020.

14 Blinn, James, F., "Light reflection functions for simulation of clouds and dusty surfaces." *Computer Graphics*, vol. 16, no. 3, 1982, pp: 21-29.

15 What Causes the Seasons?. *NASA,* 2020, https://spaceplace.nasa.gov/seasons/en/ Accessed 4 July 2020

16 Meteorology: An Educator's Resource for Inquiry-Based Learning for Grades 5-9. *NASA*, 2006, www.nasa.gov/audience/foreducators/topnav/materials/listbytype/Meteorology_Guide.html. Accessed 29 Mar. 2020.

17 "UCSB ScienceLine." *UCSB-Materials* Research Laboratory, 03 Apr. 2013, scienceline.ucsb.edu/getkey.php?key=3896. Accessed 22 Mar. 2020.

18. Physical Science. *McGraw Hill-Glencoe,* 2008.

19 Mirzaei, Parham, A., and Fariborz Hagihighat. "Approaches to study Urban Heat Island e Abilities and limitations." *Building and Environment,* Vol 45, 2010, pp. 2192-2201.

20 "2015 Surface Temperature Field Campaign." *The Globe Program,* 11 Nov. 2015, www.globe.gov/news-events/globe-news/newsdetail/globe/2015-surface-temperature-field-campain. Accessed 29 Mar. 2020.

21 Weather Underground. *The Weather Company,* 2020, www.wunderground.com. Accessed 30 Mar. 2020.

JOURNAL OF
EMERGING INVESTIGATORS

Article

Effect Of SMC On The Growth Of Bean, Cherry Tomato And Roma Tomato Plant

Nikhith Rao[1], Srihas Rao[2], Christina Palffy[3], Sudha Amineni[4]
[1,2,3,4] Adlai E Stevenson High School

SUMMARY

With a growing demand for organic fruits and vegetables, backyard gardening is becoming increasingly popular. We performed this experiment to determine the effect of Spent Mushroom Compost (SMC) in varying proportions of the soil on optimizing plant growth. We selected bean, cherry tomato, and Roma tomato plants for this study due to their popularity in gardening. Five growth media were prepared with different combinations of soil and SMC such as 0% SMC, 30% SMC, 50% SMC, 70% SMC, and 100% SMC. We hypothesized that the growth media with 30% SMC would optimize plant growth based on evidence from past research showing that moderate amounts of SMC best support the health of the plants. We used the germination rate, plant height, number of leaves, and survival rate as a measurement. We found that SMC increased plant growth of cherry tomato, Roma tomato, and bean plants. We showed that the hypothesized growth media with 30% SMC optimizes seed germination, plant height, number of leaves, and survival rate compared to other combinations of growth media. Our research suggests that SMC is a useful alternative for conventional fertilizers.

INTRODUCTION

Growing organic vegetables and fruits is healthy for individuals and for the environment. Fresh fruits and vegetables are healthier than canned, as they have less chemical exposure and the content of vitamins is higher, especially in phytochemicals, antioxidants, vitamin C, vitamin A, and folate (1). Gardening helps improve individual health, save money on groceries, and provide good exercise and stress relief (2). When growing organic fruits and vegetables, pesticide usage can also be minimized. As the usage of organic vegetables and fruits in gardening is increasing, there is a need to find an alternative source of organic fertilizers to increase plant growth and production. Therefore, we decided to research a potential organic fertilizer, Spent Mushroom Compost (SMC), to provide plants with these benefits.

Mushroom compost is a type of slow-release, organic plant fertilizer (3). Mushroom compost, also called Spent Mushroom Substrate or Spent Mushroom Compost, is suitable for a variety of plants. SMC can be used in pots, gardens or on lawns. This compost is generally made up of a mix of hay, straw, corn, and horse manure. Gardeners commonly use SMC as a soil amendment due to its ability to increase the water-holding capacity of soil, which reduces the amount of water the plants need. We chose Beans (Phaseolus vulgaris), cherry tomato, and Roma tomato (Solanum lycopersicum) plants for this study due to their popularity in gardening cultivation and their similar requirements for growth conditions.

Previous research has found that the application of SMC will increase plant growth (4). However, it is unclear which exact proportions of SMC and soil will maximize tomato and bean plant growth. As a result, for this project we tried to find the SMC quantity that best supported plant growth. Using too much SMC can cause the plants to soak up too much water, thereby resulting in the plants' death. But in moderate amounts, such as 30% SMC safely enriches soil and provides plants with nutrients. We hypothesized that bean, cherry tomato, and Roma tomato plants cultivated in growth media with 30% SMC would have the most significant growth in seed germination, plant height, number of leaves, and survival compared to other growth media ratios. For comparative purposes, we also tested the following ratios: 100% soil, 30% SMC, 50% SMC, 70% SMC, and 100% SMC. The objective of this study was to find the SMC portion mixed with soil that best supports vegetative growth. By identifying the precise conditions under which SMC leads to improvement in plant growth, our research can benefit individual gardeners, farm-to-table growing, and sustainable farming more generally.

RESULTS

We tested the effects of various SMC proportions on plant growth by measuring the germination percentage, plant height, the number of leaves per plant, and the survival rate for bean, cherry tomato, and Roma tomato plants, using five different growth media over the span of six weeks as shown in Figure 1 shows the growth stages of the plants from week 3 to week 6. The addition of SMC led to consistently higher rates of germination and survival for all three types of plants (Table 1). The percentage of seeds that germinated proved to be 100% in all growth media except the medium that received no SMC at all and one additional medium for Roma tomato, 70% SMC. The growth media with 30% SMC showed 100% germination for all three types of seeds, a performance matched only by 100% SMC.

Plant Height: Overall plant height was significantly improved by the addition of SMC to the soil for all three types of plants

at a statistically significant level of p<0.5 (Figure 2). Bean plants grown in the 30% SMC growth media had an average height of 35cm, while those grown in 0% SMC reached only 10cm. The cherry tomato plant height was also significantly improved by the addition of SMC to soil. The cherry tomato plants grown in the growth media with 30% SMC had an average height of 9cm while plants grown in the 0% SMC growth media only reached 2.32cm. Roma tomato plants grown in the 30% SMC growth media had an average height of 7cm while those grown in only SMC or only Soil growth media reached just 2.5cm (Table 2).

Number of Leaves: For all three types of plants, we found that adding SMC to the soil increased the number of leaves (Table 2). For the cherry tomato plants, we found that the number of leaves and average height per plant improved with the addition of SMC to soil. As we hypothesized, plants grown in 30% SMC produced the highest average number of leaves 8 while no SMC had the lowest 3. Roma tomato plants grown in 30% SMC growth media had an average of 6 leaves, while there was only an average of 2 leaves in plants grown in either only SMC or only soil. Bean plants grown with 30% SMC had an average of 10 leaves, while there was an average of 3 was recorded in plants grown with 0% SMC. Thus, for all three plants, the hypothesized 30% SMC had the greatest increases in plant height and number of leaves per plant (Table 2).

Survival: We found that plant survival improved with the addition of SMC to soil for both cherry tomato and Roma tomato (Table 1). Adding SMC increased survival rates in plants as compared to only soil. Only 20% of cherry tomato plants survived without SMC. Only 50% of Roma tomato plants survived without SMC.
As we hypothesized, growth media with SMC 30% showed the greatest positive impact on seed germination, plant height, number of leaves and survival rate for all three plants.

DISCUSSION

SMC supports the growth of healthy and lush plants (5). For the soil, it enhances the soil's texture and structure through the positive effects of mulching. This enhancement of the texture can increase plant growth, as the spaces between soil particles contain air that provides oxygen that living cells, like root cells, use to break down sugars and release the energy needed to live and grow. Additionally, SMC helps the growth of microorganisms in the growth media. By increasing microorganism growth, SMC supports access to high levels of important plant nutrients. Moreover, SMC makes the plants less likely to die. For example, plants are susceptible to disease. Therefore, virus-free compost helps harvest healthy plants resistant to infection. SMC helps by reducing the development of weeds, as it blocks the light out from them. Likewise, pests will not harm the plant as this compost is steam-sterilized, so using pesticides is unnecessary. Thus,

Figure 1: Experimental setup for plant growth. Picture of cherry tomato, Roma tomato, and bean plants during the experiment.

Growth Media	Bean		Cherry Tomato		Roma Tomato	
	Germination	Survival Rate	Germination	Survival Rate	Germination	Survival Rate
SMC 0%	75	100	60	20	60	50
SMC 30%	100	100	100	100	100	100
SMC 50%	100	100	100	100	100	60
SMC 70%	100	100	100	40	66	60
SMC 100%	100	100	100	100	100	100

Table 1: Shows the moderate amounts of SMC increase the seed germination rate (%) and the survival rate (%). The average germination rate of 10 seeds measured at the end of 2nd week from each growth media. Average plant survival rate of 5 plants at the end of six weeks from each growth media.

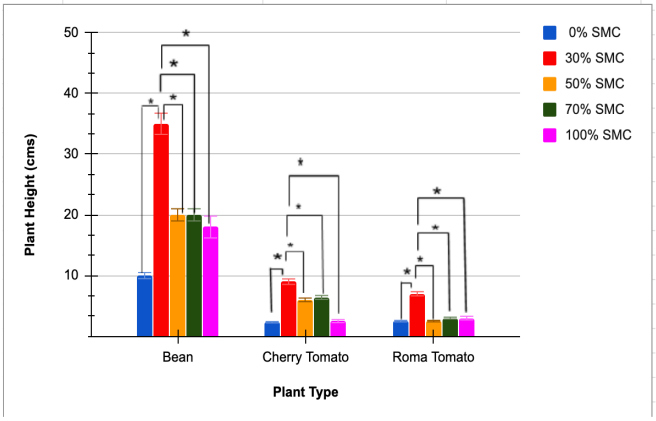

Figure 2: Shows the Moderate amounts of SMC increase plant height. The average height of five plants in centimeters at the end of six weeks from each growth media. Dark blue represents 0% SMC, red represents 30% SMC, orange represents 50% SMC, green represents 70% SMC, and magenta represents 100% SMC. Plants height for growth media of 30% SMC was significantly better than the other growth media. Asterisks (*) show that p<0.05. Error bars set at +/- 5%.

Growth Media	Bean		Cherry Tomato		Roma Tomato	
	Plant Height (cm)	Leaves per plant	Plant Height (cm)	Leaves per plant	Plant Height (cm)	Leaves per plant
SMC 0%	10	3	2.32	3	2.5	2
SMC 30%	35	10	9.00	8	7	6
SMC 50%	20	6	6.00	6	2.5	4
SMC 70%	20	6	6.40	7	3	4
SMC 100%	18	8	2.50	4	3	2

Table 2: Shows the effect of SMC on plant height (cm) and number of leaves (per plant). The average plant height and average number of leaves per plant of five plants in centimeters at the end of six weeks from each growth media.

SMC addition makes growth media more suitable for plant growth (5).

However, there are some drawbacks to using mushroom compost to grow plants (3). Spent Mushroom Compost can have negative effects on the growth of plants. Its high soluble salt levels can kill young germinating seeds and cause damage to sensitive plants. Thus, studies have found reduced growth when mixing increasing amounts of compost into commercial growth media, so we were able to conclude that moderate amounts of SMC would optimize plant growth (5). Plants, specifically seedlings, are sensitive to the high electrical conductivity in compost. SMC can also cause the soil to retain too much water and become waterlogged (6).

For this project, weathered SMC was used, as opposed to fresh SMC, because it is safer for plants. Additionally, SMC undergoes further decomposition for several weeks before farmers utilize it as a soil conditioner. It is better to use weathered SMC to plant crops, due to its lower ammonia gas content, thereby having fewer adverse effects on plants (7). In our experiment, we observed plant growth for 6 weeks. In the future, it would be beneficial to run the experiment over a longer period and measure the size and number of tomatoes/beans produced by each plant and compare that to the relative rate of growth. We were limited by our budget and space to grow plants indoors, so we could not use more than 5 plants per growth media. To gain greater confidence in our results and test for more precise statistical differences between treatments, we could include more replicates for each growth media.

Winter conditions required us to complete this experiment indoors. However, there is a possibility that not all plants obtained the same amount of sunlight through the windows. To overcome this issue, we used a full spectrum light and checked every day to see if plants were getting enough light using a three-way soil meter. Though we tried to mimic the natural environment as closely as possible, we were limited in the amount of change we could make to the temperature and humidity indoors. In future experiments, it would be helpful to have more control over these factors by using either a greenhouse or an outdoor environment.

After analysis, we found that adding SMC has a positive effect on the plant growth of cherry tomato, Roma tomato, and bean plants. Results showed that as stated in our hypothesis, the growth media with 30% of SMC had stronger effects on seed germination, plant height, number of leaves, and survival rate compared to other combinations of growth media. This analysis concludes that a moderate amount of SMC increases the plant growth. Adding the right proportions of SMC will improve soil health, thereby requiring less water.

MATERIALS AND METHODS

To test the effect of SMC, we prepared different growth media with 0% SMC, 30% SMC, 50% SMC, 70% SMC, and 100% SMC. We started the seedling process by following the instructions on the seed packet to ensure optimal conditions for the seeds. Soak seeds in warm water for 2 to 4 hours to soften. Moisten paper towels and spread the seeds evenly and put them in a Ziploc bag for 2 days. Fill planting pots with growth media and put two sprouts into each quad. Regularly irrigate seedling trays with 500 mL deionized water to maintain humidity suitable for plant growing. Using a 3-way soil meter, check every morning and evening to determine if plants are getting enough light.

Sunlight plays an important role in plant growth. Seeds require moderate temperatures of 25°–30°C for germination (8). We used a full spectrum light to maintain the temperature and light illumination. Germinate the seedlings with twelve hours of light for the first two weeks. After this period, increase the time of sunlight to between 14-16 hours daily for the following weeks. The lights allow year-round cultivation. This is important as the plants can get the year-round light that they need.

We measured and recorded the germination growth during the first two weeks. After two weeks we transplanted each plant (5 sprouts per growth media per plant) into 15cm of height biodegradable pots and labeled them using supporting sticks. We collected tap water and let it sit for 24 hours before using it. Seedling trays were regularly irrigated with 500 mL tap water in order to maintain humidity suitable for plant growth. We measured and recorded plant length using a ruler as well as the number of leaves from the 3rd to the 6th week.

Statistical Analysis

To determine whether there were statistically significant differences between different growth media in germination, plant height, number of leaves per plant, and survival rate we applied the t-test using google sheets. 30% SMC data was significant at $p<0.05$ as shown in the Figure 2 with *.

Received: Jun 06, 2020
Accepted: Jul 05, 2020
Published: September 03, 2020

REFERENCES

1. Crinnion, Walter J. “Organic foods contain higher levels of certain nutrients, lower levels of pesticides, and may provide health benefits for the consumer.” Alternative medicine review: a journal of clinical therapeutic vol. 15,1 (2010): 4-12.
2. “The Benefits of Growing a Vegetable Garden.” Burke Rehabilitation Hospital, 26 Apr. 2016.
3. “Mushroom Compost Benefits: Organic Gardening With Mushroom Compost.” Gardening Know How.
4. Gonani, Z., et al. “IMPACT OF USING LEACHED SPENT MUSHROOM COMPOST AS A PARTIAL GROWING MEDIA FOR HORTICULTURAL PLANTS.” Journal of Plant Nutrition, vol. 34, no. 3, 20 Jan. 2011, pp. 337–344, 10.1080/01904167.2011.536876. Accessed 19 Aug. 2020.
5. Weeks, Peter. “Mushroom Compost: Is It Always Good for Your Plants?” The Daily Gardener, 27 Mar. 2019.
6. “Mushroom Compost: What It Is, What It Does, And How

To Make It." Epic Gardening, 8 Mar. 2018.
7. Jonathan, Segun Gbolagade, et al. "Effect of Spent Mushroom Compost of Pleurotus Pulmonarius on Growth Performance of Four Nigerian Vegetables." Mycobiology, vol. 39, no. 3, Sept. 2011, pp. 164–169, 10.5941/myco.2011.39.3.164.
8. Gilbert, Scott F. "Germination." Nih.Gov, Sinauer Associates, 2012.

ACKNOWLEDGEMENTS

In the successful completion of this project, we would like to thank Mrs. Greenberg for their help in preparing and editing this paper for the presentation at the IJAS competition and Stevenson High School Science Department.

JOURNAL OF
EMERGING INVESTIGATORS

Article

Assessing the efficacy of NOX enzyme inhibitors as potential treatments for ischemic stroke *in silico*

Samhita Vinay,* Keertana Yalamanchili,* Sowmya Vinay
Thomas Jefferson High School for Science & Technology, Alexandria, Virginia
*authors contributed equally

SUMMARY

Ischemic stroke occurs when blood flow to the brain is interrupted, causing brain damage. There is evidence that reactive oxygen species, ROS, are produced by the enzyme family NADPH oxidase (NOX) following ischemic stroke, which leads to further brain injury. This study investigated the effectiveness of different NOX inhibitors as treatments for ischemic stroke *in silico*. The ADMET (absorption, distribution, metabolism, excretion, and toxicity) profile of each NOX inhibitor was taken, in which four classifications, namely applicability domain, human intestinal absorption, blood-brain barrier, and human oral bioavailability, were observed. The profile was used to determine the properties of each inhibitor in order to examine the extent to which it will work as a drug candidate. Then, AutoDock Vina was used to model the docking of the inhibitors: VAS2870, GSK2795039, apocynin, and AEBSF to NOX2, an isoform of the NOX family. We hypothesized that VAS2870 would be the most effective inhibitor *in silico* due to its potency to NOX2, not present in the other inhibitors. The binding affinities of each of the inhibitors to NOX2 were recorded, and the value was used to calculate the K_i value of each inhibitor. VAS2870 and apocynin were the most potent NOX2 inhibitors, and all four inhibitors had favorable ADMET profiles. This study helps corroborate previous *in vivo* and *in vitro* studies in an *in silico* format, and can be used towards developing drugs to treat ischemic stroke.

INTRODUCTION

Ischemic stroke is a disease where a blocked blood vessel damages the brain by slowing down or interrupting blood flow (1). It accounts for approximately 88% of all strokes, and its onset can be influenced by several other diseases (2). It develops due to an improper supply of blood to the brain, which results in an inability for sufficient metabolism to occur, therefore restricting oxygen and glucose supply to the brain (3). The lack of sufficient oxygen and glucose supply compromises ion gradients, which allows cations to build up in the cells and further stimulates proteolytic activity causing neuronal apoptosis and the systematic degradation of the extracellular matrix (3). This process breaks the basal lamina, which results in leakage, undermining the integrity of the blood-brain barrier and causing an inflow of inflammatory cells into the brain, ultimately causing neuronal death (4). The blood-brain barrier is vital for controlling homeostasis in the central nervous system and protecting neural tissue from toxic substances (5). Therefore, its disruption can lead to inflammation of the brain, known as vasogenic edema, and a hemorrhage. Following ischemic stroke, reactive oxygen species (ROS) are produced, leading to further brain damage (6). Normally, oxygen-derived free radicals, often known as ROS, play roles in immunity and cell signaling; however, in excess, they lead to several diseases including ischemic stroke (7). Enzymes known as NADPH oxidases, which are in the NOX family, are attributed to producing ROS in human cells. Along with Rac as a binding partner, NOX2 is composed of isoforms and subunits, the former being NOX1-5, Duox1, and Duox2, and the latter being $p22^{phox}$, $p47^{phox}$, $p67^{phox}$, and $p40^{phox}$ (8). As a key element of the electron transport chain in cellular respiration, the ROS are produced by reducing electrons in oxygen. The family of enzymes was first found in the neutrophils and macrophages of the human immune system. Now, however, *in vivo* and *in vitro* studies suggest that NOX1, NOX2, NOX3, and NOX4 are expressed throughout the central nervous system, although their function with respect to the brain is unknown. Various studies have also confirmed that NOX enzymes, along with the ROS produced, play a role in brain injury progression following ischemic stroke (9).

In vivo and *in vitro* studies have determined several viable inhibitors of NOX2, which can be incorporated in ischemic stroke drug treatment. In this study, four inhibitors of the NOX2 isoform were selected including VAS2870, GSK2795039, AEBSF, and Apocynin, and their efficacy as potential ischemic stroke treatments was assessed. These four inhibitors were selected because they were the only inhibitors with 3D structures in the PubChem Database. NOX2 was the enzyme we focused on due to its high expression levels in endothelial cells in the brain (9), as well as the fact that its 3D model was the most accessible out of all the isoforms. VAS2870 is an artificial inhibitor that inhibits all NOX isoforms except NOX3 (10). Studies have demonstrated that VAS2870 leads to neuroprotective effects in mice that are not displayed in control groups (11). GSK2795039 is another artificially constructed inhibitor which competitively

inhibits NOX2 and reduces ROS production (12). In addition, AEBSF can block the binding of the subunits $p47^{phox}$ and $p67^{phox}$ as an irreversible inhibitor (11); however, it also is an inhibitor of serine proteases, which enzymatically break peptide bonds (13). Lastly, apocynin, is an antioxidant, and studies demonstrated that prior to ischemic stroke, the inhibitor showed neuroprotection and reduced blood-brain barrier disruption (11).

Here, we used ADMET (absorption, distribution, metabolism, excretion, and toxicity) to assess the biochemical properties of our four aforementioned inhibitors (14). ADMET is important when discovering new drugs because an accurate prediction of these properties can determine if the drug will work as intended (15). Although the ADMET properties are considered at the end of the drug testing process, they are now accounted for while eliminating potential docking molecules in order to improve efficiency and decrease associated costs. There are several classification systems that are used to assess drug molecules, namely applicability domain, human intestinal absorption, blood-brain barrier, and human oral bioavailability. The applicability domain considers whether the molecule is within the domain of the training set for six different properties: molecular weight, alogP, number of atoms, number of rings, H-bond acceptors, and H-bond donors (16). alogP is an atom-based method for predicting logP, which is the logarithm of the ratio of a solute among two solvents, also known as the partition coefficient (17). The human intestinal absorption classification determines how effectively orally administered drugs are absorbed from the intestine into the bloodstream (18). The blood-brain barrier classification shows how easily molecules can cross through the highly selective semipermeable barrier (19). The human oral bioavailability classification depicts how much of the drug reaches the target area (20). The ADMET properties for each molecule are represented with a predicted value and a predicted probability to display the drug's efficacy (19).

In addition to ADMET properties, we also will utilize molecular docking, which is a modeling technique that is used for discovering new drugs by determining how well one molecule can bind to another molecular structure (21). The orientation with which a molecule binds to a target can be used to assess its effectiveness (22). There are several types of docking, and the more commonly used types include protein-ligand docking and protein-protein docking (23). Protein-ligand docking can be used to determine how a ligand will bind to a protein and whether or not the ligand will act as an inhibitor or an activator (24). Protein-protein docking is an easier technique because the docking between the two proteins can be either flexible or rigid, meaning that precise measurement is not necessary (23). Molecular docking can be performed via various applications. AutoDock is one type of software that simulates an automated docking technique (25). The software contains AutoDock Vina, which is a program that performs protein-ligand docking by using an empirical scoring function and a conformation search based on global optimization (26).

We hypothesized that out of the four inhibitors: VAS2870, GSK2795039, AEBSF, and apocynin, VAS2870 would be the most effective inhibitor *in silico* because previous *in vivo* and *in vitro* studies revealed that it successfully inhibited NOX2, while the efficacy of the other inhibitors was not mentioned (10). The data from the study showed that VAS2870 and apocynin were the most potent NOX2 inhibitors and that all four inhibitors had favorable ADMET profiles. These results can be used for developing medication for ischemic stroke in the future.

RESULTS

The ADMET profiles of the four different inhibitors: apocynin, VAS2870, GSK2795039, and AEBSF were assessed using admetSAR (16). For each inhibitor, four different classifications were observed: the applicability domain, human intestinal absorption, blood-brain barrier, and human oral bioavailability. All four inhibitors are in the applicability domain, meaning that the admetSAR interface can use its training set to predict their properties. In terms of the human intestinal absorption classification, all four inhibitors have a "+" predicted value as well as predicted

Table 1. ADMET properties of different inhibitors.

Inhibitor	*Applicability Domain*	*Human Intestinal Absorption*	*Blood-Brain Barrier*	*Human Oral Bioavailability*
apocynin	In domain	+; 1.0000	+; 0.9483	+; 0.5857
VAS2870	In domain	+; 0.9820	+; 0.9785	+; 0.5286
GSK2795039	In domain	+; 0.9947	+; 0.9750	+; 0.6143
AEBSF	In domain	+; 0.9656	+; 0.9733	+; 0.8857

Note: The "+" or "-" represent whether the molecule does or does not display the particular property, respectively. The predicted probability is depicted by a number between 0 and 1, which shows the probability of the molecule acting as indicated by the previously mentioned predicted value (19). The "In domain" shows that the compound falls into the range established by 99% of the training set.

Table 2. Descriptive statistics of each inhibitor.

Binding Energy (kcal/mol)	Inhibitors			
	apocynin	VAS2870	GSK2795039	AEBSF
Mean	-7.2	-7.2	-6.4	-4.5
Median	-7.2	-7.2	-6.3	-4.4
S.D.	0.0	0.0	0.2	0.1
Number	5	5	5	5
SEM	0.0	0.0	0.1	0.1
K_i	$5.2*10^{-6}$	$5.2*10^{-6}$	$2.0*10^{-5}$	$5.0*10^{-4}$

Note: The values represent the binding energies in kcal/mol. The table includes means, medians, standard deviations, the number of data points used, the standard error of the mean, and inhibitor constants.

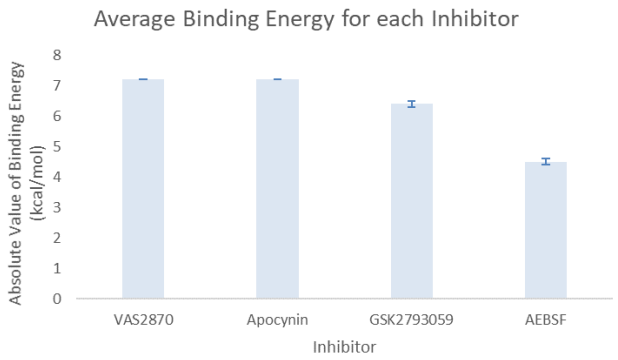

Figure 1. Average binding energy of each inhibitor. The data represents the absolute value of the average binding energies (in kcal/mol) +/- 1 standard error. For each average value, 5 trials were conducted.

probabilities greater than 0.95 (**Table 1**), meaning that they can probably be absorbed from the intestine into the bloodstream. Furthermore, all four inhibitors have a "+" predicted value and a predicted probability greater than 0.945 for the blood-brain barrier classification, meaning that they can probably pass through the membrane effectively (**Table 1**). Lastly, although all four inhibitors have a "+" predicted value (**Table 1**) for the human oral bioavailability classification, their predicted probabilities are low and lie between 0.55 and 0.65, except for AEBSF, which has a predicted probability of 0.8857. Although the human oral bioavailability probabilities of apocynin, VAS2870, and GSK2705039 are closer to 0.5 than to 1, overall, all four inhibitors have favorable ADMET profiles.

Blind docking analysis using AutoDock Vina was used to analyze the efficacy of the four NOX2 inhibitors as potential treatments for ischemic stroke. The average binding affinities of VAS2870 and apocynin were equal, at -7.2 kcal/mol, while that of GSK2795039 and AEBSF were -6.4 kcal/mol and -4.5 kcal/mol respectively (**Table 2**). The negative binding affinities of all the inhibitors suggest binding to NOX2 is stable. The K_i value for each inhibitor, which was calculated for each inhibitor, and the lower the value, the more potent the inhibitor (**Table 2**). The K_i value of $5.2 * 10^{-6}$ was the lowest, demonstrating that VAS2870 and apocynin are predicted to be the most potent inhibitors of NOX2. AEBSF was the least potent NOX2 inhibitor, as its K_i value of $5.0 * 10^{-4}$ was the greatest value. The range of the binding affinity of each inhibitor as displayed by standard deviation was relatively low, with all of them having values at or close to 0.0 (**Table 2**).

Next, we determined the absolute value binding energies of each inhibitor by calculating the average binding energy of five trials for each inhibitor and taking the absolute value of the result (**Figure 1**). There was little to no variation between the absolute values of the binding energies of each inhibitor (**Figure 1**). VAS2870 and apocynin had the same average absolute value binding energy, with standard errors of 0. Both GSK2795039 and AEBSF had slightly larger standard errors of 0.1. The standard errors of GSK2795039 and AEBSF do not overlap (**Figure 1**). Those of VAS2870 and apocynin only overlap because the data was the same with no variation.

Lastly, we used a Kruskal-Wallis test to analyze whether the differences in the binding affinities of the inhibitors were statistically significant or not, as the data was not normally distributed. According to the test, there was a statistically significant difference in the binding energies of the different inhibitors, $\chi^2(3, N = 20) = 18.411$, p-value < 0.001. Results from the Dunn-Bonferroni post-hoc tests revealed that VAS2870 and apocynin were significantly different from AEBSF (p-value 0.001, adjusted to 0.006), but not GSK2795039 (0.015, adjusted to 0.090) in terms of binding energies (kcal/mol). When VAS2870 was compared to apocynin, the p-value and Bonferroni-corrected p-value were both 1.000, since the averages were the same. The pairwise comparison between GSK2795039 and AEBSF resulted in a p-value of 0.391 and a Bonferroni-corrected p-value of 1.000.

DISCUSSION

The purpose of this study was to investigate the effectiveness of four NOX2 inhibitors *in silico* so that they may eventually be candidates for drugs against ischemic stroke. This was accomplished through downloading models of NOX2 and each of the inhibitors and simulating how the inhibitors dock to NOX2 using AutoDock Vina. ADMET profiles of all the inhibitors were also assessed through taking into account the applicability domain, human intestinal absorption, blood-brain barrier, and human oral bioavailability. Following this, the Ki values for each of the inhibitors were calculated to assess the potency of each of the inhibitors. Overall, the data supported our hypothesis that VAS2870 would be the most potent inhibitor of NOX2, but it did not account for the fact that apocynin was equally as potent, and that there was no significant difference between the binding energies of VAS2870/apocynin and GSK2795039. Nevertheless, all the inhibitors were predicted to inhibit the NOX2 enzymes, and they all had favorable ADMET profiles.

In silico studies confer many advantages in early-stage drug development compared to *in vivo* and *in vitro* studies, such as speed and the ability to predict a molecule's properties before synthesis (27). Furthermore, they can be more representative of human body systems than animal models in terms of identifying side effects and determining how effective the drugs are (28). However, there may have been possible errors in the docking methodology. For example, the protein flexibility and molecule conformation may not have been accounted for properly by the AutoDock Vina program, resulting in inaccurate data. Furthermore, *in silico* docking softwares typically use an algorithm based on human properties, whereas *in vivo* and *in vitro* use a variety of other species. As a result, *in silico* findings cannot be considered as a complete replacement for *in vivo* and *in vitro* findings. Instead, they are a way to model and predict what

the docking might look like if it was conducted *in vivo* or *in vitro*.

To our knowledge, this is the first in silico study investigating the NOX2 enzymatic pathway as a possible treatment for ischemic stroke. *In vivo* and *in vitro* studies have illustrated that inhibiting the NOX2 enzyme led to neuroprotective effects following ischemic stroke by reducing ROS production (10-12). Although this study could not assess the behavior of animal models after this treatment, it demonstrates that these pharmacologically important inhibitors have the potential to be incorporated in drugs used to treat brain injury following ischemic stroke. The study also supports the findings of the *in vivo* and *in vitro* studies, as all of the inhibitors modeled were determined to be potent.

Further research on the docking of the NOX2 inhibitors *in vivo* and *in vitro* would be helpful to corroborate the results of this study. The additional research would more accurately consider protein flexibility and molecule conformation when determining the binding affinities of the inhibitors. Other compounds could also be tested and verified as inhibitors in future studies. For example, recombinant tissue plasminogen activator (rtPA), a compound for treating ischemic stroke, has a favorable ADMET profile, with a predicted probability of 0.902 for human intestinal absorption, 0.984 for passing through the blood-brain Barrier, and 0.723 for human oral bioavailability (29). Although rtPA has a higher predicted probability for passing through the blood-brain Barrier than the four inhibitors we observed (VAS2870, apocynin, GSK2795039, and AEBSF), the predicted probability of rtPA for human intestinal absorption is lower than the probabilities predicted for the four inhibitors we observed. In terms of human oral bioavailability, rtPA has a higher predicted probability than VAS2870, apocynin, and GSK295039, but a lower predicted probability than AEBSF. Moreover, it would also show how the docking occurs in different species. Although AutoDock Vina was used due to its user-friendliness, future studies could use additional platforms for molecular docking, such as SwissDock and UCSF Dock Blaster, to test not only the efficacy of AutoDock Vina, but also the consistency of binding scores and docking visualization.

METHODS

ADMET

ADMET Profiling: A unique SMILES (Simplified Molecular Input Line Entry System) notation, representing different molecules, was found for each inhibitor by entering the name of the inhibitor in the search tool in the PubChem website. The SMILES notation for each inhibitor was entered in the search box of the "Predict" tool of the admetSAR web tool. Several of the classifications, particularly the applicability domain, human intestinal absorption, blood-brain barrier, and human oral bioavailability, were taken into account when determining whether the ADMET profile of the inhibitor was favorable or not.

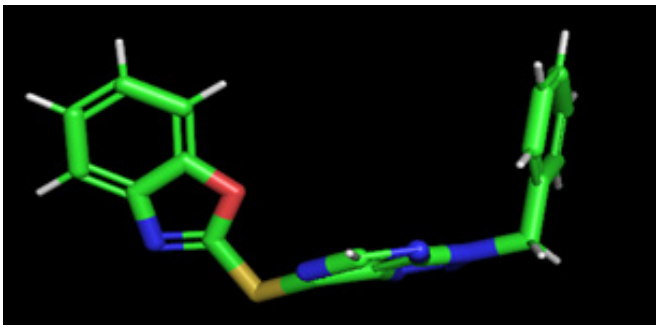

Figure 2. SDF file of VAS2870 displayed in PyMOL. The image shows the 3D structure of the inhibitor. The green parts of the structure represent the carbons, the red signifies oxygen, the blue represents nitrogen, the yellow signifies sulfur, and the gray extensions represent hydrogens.

Downloading & File Modification

Downloading: AutoDock Vina, AutoDock Tools, and PyMOL were downloaded onto the laptop from their respective websites online (30-32). The protein molecule 3A1F (the crystal structure of NOX2) was downloaded from the database RCSB PDB as a PDB file into a folder in the desktop with the licensing of AutoDock Vina (33). The 3D conformation of the inhibitor molecules: VAS2870, GSK2795039, apocynin, and AEBSF were downloaded from the PubChem database as SDF files into the same folder (**Figure 2**; 34-37).

SDF to PDB Conversion: The SDF file of the 3D structure of each inhibitor was uploaded into PyMOL, and then saved as a PDB file to the same folder that the SDF files were initially.
Protein Modification: The PDB file of 3A1F was opened as a text document, and all the lines with "HETATOM" were deleted, as the structure came with the nickel molecule (labeled with "HETATOM") already bound to the protein.
PDB to PDBQT Conversion: AutoDock Tools was opened, and then the PDB file of each of the inhibitors was uploaded and saved as a PDBQT file.

Several modifications were made for the NOX2 PDB conversion including removing waters, since waters are not included in the binding process, and adding hydrogens, because it adds to the stability of the protein (38). Following the chemical modification of the protein, a grid was set up so that the whole protein could be screened for potential binding sites. For this to occur, the number of points in the x, y, and z-dimensions were set to 126. The spacing was set to 0.375 angstroms, and the x, y, and z-centers were set to 15.597, -13.324, and 10.201 respectively. Then, a text file of the grid information was saved in the same folder, along with the protein in PDBQT format.

Configuration File Creation: A configuration file, conf.txt, was created in order to specify the receptor and the ligand molecule to be used for the docking. In the file, the receptor was set to the protein file name, and the ligand was set to the inhibitor file name. The center-x, center-y, and center-z

```
center_x= 15.597

center_y= -13.324

center_z=  10.201
```

Figure 3. Coordinates of the center of NOX2 in the configuration file. The variables center_x, center_y, and center_z represent the x, y, and z coordinates of the grid, respectively. These coordinates were used to align each of the inhibitors to the protein.

were set according to the centers used in the grid dimensions (**Figure 3**), and the sizes of x, y, and z were set to 66, 56, and 54 respectively. The output was set to another PDBQT file named vina_outSO.pdbqt, the log was set to logSO.txt, and the exhaustiveness was set to 8. The ligand of the file was altered each time a new inhibitor was used for docking.

Molecular Docking

Docking: A command prompt was opened, and the desktop folder with all the necessary components was accessed by typing in "cd Desktop" and then "cd Vina". In order to find the binding affinity of the inhibitors with NOX2, "vina.exe" --config conf.txt was typed. This command ran blind docking analysis, assessing all the potential locations in which the inhibitor can bind to NOX2. After the analysis was complete, a table of binding affinities, distance from RMSD lower bound, and distance from RMSD upper bound appeared, detailing the results of each potential binding site for the docking analysis. This process was repeated four times for each inhibitor and for other inhibitors by altering conf.txt and running the blind docking for each inhibitor.

3D Visualization: the output ligand and NOX2 were uploaded into PyMOL, a visualization software. In order to show the interactions between the protein and the ligand, we visualized contacts of chains between 3.0Å, 3.5Å, and 4.0Å, which were shown in a dotted line.

Analysis

K_i value calculation: the average binding affinity was taken for each inhibitor, and then converted to a K_i value, also known as the inhibition constant. The equation, $K_i = e^{(deltaG/(RT))}$, was used for the conversion, where the binding affinity was substituted for the delta G value, R was the gas constant of 1.987 cal/molK, and T was the temperature: 298 K.

Statistical analysis: The standard errors were calculated by dividing the standard deviation by the square root of the number of trials, which was 5. Afterwards, a Kruskal-Wallis test was used to determine the statistical significance of the difference in the binding affinity of each inhibitor. This non-parametric test was used, since a normal distribution is not assumed, and as there were four levels of the independent variable that needed to be analyzed. Following this, a Dunn-Bonferroni post-hoc test was performed to see whether there were statistically significant differences between the groups. A Bonferroni Correction was applied for each significance value to account for errors due to multiple comparisons.

Received: May 20, 2020
Accepted: August 31, 2020
Published: September 18, 2020

REFERENCES

1. "Stroke." *Mayo Clinic*, Mayo Foundation for Medical Education and Research, 24 Apr. 2020, www.mayoclinic.org/diseases-conditions/stroke/symptoms-causes/syc-20350113.
2. "The Internet Stroke Center." *The Internet Stroke Center. An Independent Web Resource for Information about Stroke Care and Research.*, www.strokecenter.org/patients/about-stroke/ischemic-stroke/.
3. Bhattacharya, Pallab, *et al*. "Neuroprotection by μ-Calpain and Matrix Metalloproteinases Inhibition by Piroxicam in Cerebral Ischemia: an in Silico Study." *Medicinal Chemistry Research*, vol. 22, no. 11, 2013, pp. 5112–5119., doi:10.1007/s00044-013-0514-7.
4. Bramlett, Helen M., and W. Dalton Dietrich. "Pathophysiology of Cerebral Ischemia and Brain Trauma: Similarities and Differences." *Journal of Cerebral Blood Flow & Metabolism*, vol. 24, no. 2, 2004, pp. 133–150., doi:10.1097/01.wcb.0000111614.19196.04.
5. Abdullahi, Wazir, *et al*. "Blood-Brain Barrier Dysfunction in Ischemic Stroke: Targeting Tight Junctions and Transporters for Vascular Protection." *American Journal of Physiology-Cell Physiology*, vol. 315, no. 3, 2018, doi:10.1152/ajpcell.00095.2018.
6. Rodrigo, Ramon, *et al*. "Oxidative Stress and Pathophysiology of Ischemic Stroke: Novel Therapeutic Opportunities." *CNS & Neurological Disorders - Drug Targets*, vol. 12, no. 5, 2013, pp. 698–714., doi:10.2174/18715272311312050015.
7. Panday, Arvind, *et al*. "NADPH Oxidases: an Overview from Structure to Innate Immunity-Associated Pathologies." *Cellular & Molecular Immunology*, vol. 12, no. 1, 2014, pp. 5–23., doi:10.1038/cmi.2014.89.
8. Lassègue, Bernard, *et al*. "Biochemistry, Physiology, and Pathophysiology of NADPH Oxidases in the Cardiovascular System." *Circulation Research*, vol. 110, no. 10, 2012, pp. 1364–1390., doi:10.1161/circresaha.111.243972.
9. Zhang, Li, *et al*. "NADPH Oxidase: A Potential Target for Treatment of Stroke." *Oxidative Medicine and Cellular Longevity*, vol. 2016, 2016, pp. 1–9., doi:10.1155/2016/5026984.
10. Augsburger, Fiona, *et al*. "Pharmacological

Characterization of the Seven Human NOX Isoforms and Their Inhibitors." *Redox Biology*, vol. 26, 2019, 101272., doi:10.1016/j.redox.2019.101272.
11. Kim, Jong Youl, *et al.* "NOX Inhibitors - A Promising Avenue for Ischemic Stroke." *Experimental Neurobiology*, vol. 26, no. 4, 2017, pp. 195–205., doi:10.5607/en.2017.26.4.195.
12. Hirano, Kazufumi, *et al.* "Discovery of GSK2795039, a Novel Small Molecule NADPH Oxidase 2 Inhibitor." *Antioxidants & Redox Signaling*, vol. 23, no. 5, 2015, pp. 358–374., doi:10.1089/ars.2014.6202.
13. Poddar, Nitesh Kumar, *et al.* "Role of Serine Proteases and Inhibitors in Cancer." *Proteases in Physiology and Pathology*, 2017, pp. 257–287., doi:10.1007/978-981-10-2513-6_12.
14. Guan, Longfei, *et al.* "ADMET-Score – a Comprehensive Scoring Function for Evaluation of Chemical Drug-Likeness." *MedChemComm*, vol. 10, no. 1, 2019, pp. 148–157., doi:10.1039/c8md00472b.
15. G. P. S. Raghava's Group. *Computational Tools for ADMET*, crdd.osdd.net/admet.php.
16. "Applicability Domain." *AD | AdmetSAR*, lmmd.ecust.edu.cn/admetsar2/about/ad.
17. Ghose, Arup K., *et al.* "Prediction of Hydrophobic (Lipophilic) Properties of Small Organic Molecules Using Fragmental Methods: An Analysis of ALOGP and CLOGP Methods." *The Journal of Physical Chemistry A*, vol. 102, no. 21, 1998, pp. 3762–3772., doi:10.1021/jp980230o.
18. Isle Interactive Ltd. "Human Intestinal Absorption." *Isle Spark*, www.asteris-app.com/technical-info/adme-properties/humanintestinalabsorption.htm.
19. "blood-brain Barrier." *DrugBank Developer Hub*, ev.drugbankplus.com/guides/terms/blood-brain-barrier.
20. Kim, Marlene T., *et al.* "Critical Evaluation of Human Oral Bioavailability for Pharmaceutical Drugs by Using Various Cheminformatics Approaches." *Pharmaceutical Research*, vol. 31, no. 4, 2013, pp. 1002–1014., doi:10.1007/s11095-013-1222-1.
21. Berry, Michael, *et al.* "Practical Considerations in Virtual Screening and Molecular Docking." *Emerging Trends in Computational Biology, Bioinformatics, and Systems Biology*, 2015, pp. 487–502., doi:10.1016/b978-0-12-802508-6.00027-2.
22. Hakes, L., *et al.* "Specificity in Protein Interactions and Its Relationship with Sequence Diversity and Coevolution." *Proceedings of the National Academy of Sciences*, vol. 104, no. 19, 2007, pp. 7999–8004., doi:10.1073/pnas.0609962104.
23. Hernandez-Santoyo, Alejandra, *et al.* "Protein-Protein and Protein-Ligand Docking." *Protein Engineering - Technology and Application*, 2013, doi:10.5772/56376.
24. Smith, Richard D., *et al.* "Biophysical Limits of Protein–Ligand Binding." *Journal of Chemical Information and Modeling*, vol. 52, no. 8, 2012, pp. 2098–2106., doi:10.1021/ci200612f.
25. "AutoDock." *AutoDock - an Overview | ScienceDirect Topics*, www.sciencedirect.com/topics/biochemistry-genetics-and-molecular-biology/autodock.
26. Trott, Oleg, and Arthur J. Olson. "AutoDock Vina: Improving the Speed and Accuracy of Docking with a New Scoring Function, Efficient Optimization, and Multithreading." *Journal of Computational Chemistry*, 2009, doi:10.1002/jcc.21334.
27. Amberg, Alexander. "In Silico Methods." *Drug Discovery and Evaluation: Safety and Pharmacokinetic Assays*, 2013, pp. 1273–1296., doi:10.1007/978-3-642-25240-2_55.
28. Coleman, Robert A. "Human Tissue in the Evaluation of Safety and Efficacy of New Medicines: A Viable Alternative to Animal Models?" *ISRN Pharmaceutics*, vol. 2011, 2011, pp. 1–8., doi:10.5402/2011/806789.
29. Dong, Jie. "Home-ADMElab: ADMET Prediction: ADMET Predictor: QSAR: ADMET Database." *Home-ADMElab: ADMET Prediction|ADMET Predictor|QSAR|ADMET Database*, admet.scbdd.com/.
30. "Download:" *AutoDock Vina - Molecular Docking and Virtual Screening Program*, vina.scripps.edu/download.html.
31. "Downloads." *MGLTools*, mgltools.scripps.edu/downloads.
32. "PyMOL Is a User-Sponsored Molecular Visualization System on an Open-Source Foundation, Maintained and Distributed by Schrödinger. We Are Happy to IntroducePyMOL 2.4!" *PyMOL*, pymol.org/2/#download.
33. Bank, RCSB Protein Data. "3A1F: The Crystal Structure of NADPH Binding Domain of gp91(Phox)." *RCSB PDB*, www.rcsb.org/structure/3a1f.
34. "2-(3-Benzyltriazolo[4,5-d]Pyrimidin-7-Yl)Sulfanyl-1,3-Benzoxazole." *National Center for Biotechnology Information. PubChem Compound Database*, U.S. National Library of Medicine, pubchem.ncbi.nlm.nih.gov/compound/vas2870.
35. "1-Methyl-N-[3-(1-Methyl-2,3-Dihydroindol-6-Yl)-1-Propan-2-Ylpyrrolo[2,3-b]Pyridin-4-Yl]Pyrazole-3-Sulfonamide." *National Center for Biotechnology Information. PubChem Compound Database*, U.S. National Library of Medicine, pubchem.ncbi.nlm.nih.gov/compound/71090129.
36. "Acetovanillone." *National Center for Biotechnology Information. PubChem Compound Database*, U.S. National Library of Medicine, pubchem.ncbi.nlm.nih.gov/compound/2214.
37. "4-(2-Aminoethyl)Benzenesulfonyl Fluoride." *National Center for Biotechnology Information. PubChem Compound Database*, U.S. National Library of Medicine, pubchem.ncbi.nlm.nih.gov/compound/1701.
38. "How to Perform Blind Docking Using AutoDock Vina?" *Bioinformatics Review*, 1 May 2019, bioinformaticsreview.com/20190501/how-to-perform-blind-docking-using-autodock-vina/.

JOURNAL OF
EMERGING INVESTIGATORS

Article

Sepia bandensis ink inhibits polymerase chain reactions

Anna Novoselov, Eric Espinosa
BioCurious, Santa Clara, CA

SUMMARY

While cephalopods serve critical roles in ecosystems and are of significant interest in scientific studies of the nervous system, medicinal toxins, and evolutionary diversification. The absence of a genomic library and the lack of comprehensive gene analysis present challenges to conducting efficient and thorough research. One difficulty in advancing cephalopod genomics is the presence of inhibitors (such as ink) that impede the amplification of DNA samples with PCR. We tested the hypothesis that *Sepia bandensis* (dwarf cuttlefish) ink inhibits PCR by running PCR reactions with and without the back addition of ink to *Turbo fluctuosus* (marine sea snail) DNA with the inclusion of the appropriate positive and negative controls. The experimental results show that ink added to *T. fluctuosus* DNA extracted using two kit-based extraction methods or phenol chloroform extraction prevents the amplification of the cytochrome c oxidase subunit I (COI) mitochondrial gene. Also, while modern extraction methods like quaternary amine resin and silica column isolation failed to produce genomic products viable for PCR from *S. bandensis*, phenol chloroform extraction eliminated the inhibitors and resulted in successful amplification. The results of this investigation could further cephalopod genomic studies and serve as a model for experiments aiming to determine the cause of PCR inhibition.

INTRODUCTION

Mollusks occupy a key role in ecosystems around the world: they purify water by passing it through their internal biological systems, recycle nutrients in the ocean, and serve as integral parts of many food webs (1). However, due to climate change and habitat destruction, their populations may become threatened (2). This fact poses threats to the stability of many ecosystems and to the survival of several species in the mollusk phylum, including those in the Cephalopoda class.

Although cephalopods play significant roles in natural ecosystems and in medical research, there is currently no assembled cephalopod genome, as challenges in accessing samples and keeping cephalopods (specifically oceanic and deep-sea species) in a lab setting have prevented the large scale analysis of their molecular and morphological features (3-5). Thus, there is limited information on mollusk transcriptomes and genomic regulation, but advancements could be made through genetic studies and DNA barcoding. Many sequencing efforts are underway due to the popularization and increased ease of molecular sequencing, yet difficulties, such as repeated regions and gene duplication events, have prevented the compilation of a full genome (1, 4, 6).

Biocurious's cuttlefish project team chose *Sepia bandensis* (the dwarf cuttlefish) as a potential model organism for mollusks due to its small size and diagnostic features, like aligned suckers, chromatophores, and dorsal and ventral protective membranes as shown in **Figure 1** (7, 8).

The initial goal of the project was to sequence the *S. bandensis* genome and study the cephalopod's gene expression, but difficulties arose while attempting to prepare PCR products for genomic sequencing. Originally, the isolation of cuttlefish DNA by silica column and quaternary amine resin failed to produce genomic DNA products that were viable for PCR amplification of a segment of the cytochrome c oxidase subunit one COI mitochondrial gene (unpublished findings). We performed gel electrophoresis and saw no band of the expected 710 base pairs. Since COI is found in all eukaryotic organisms, including the closely related cuttlefish *S. officinalis* (the common cuttlefish), it is highly improbable that *S. bandensis* lacks this gene. We hypothesized that the failure was due to interference from inhibitors or inferior enzymes, as those are well-documented causes of PCR failure.

Repeatedly, inhibitors have been shown to increase error, reduce assay resolution, and produce inaccurate results in both quantitative and qualitative PCR assays (9, 10). Common mechanisms of PCR inhibition include the binding of an inhibitor to the polymerase, erroneous polymerase interaction with DNA, and inhibitor interaction with the polymerase during primer extension. Inhibitor sources may include reagents used during sample preparation, contamination,

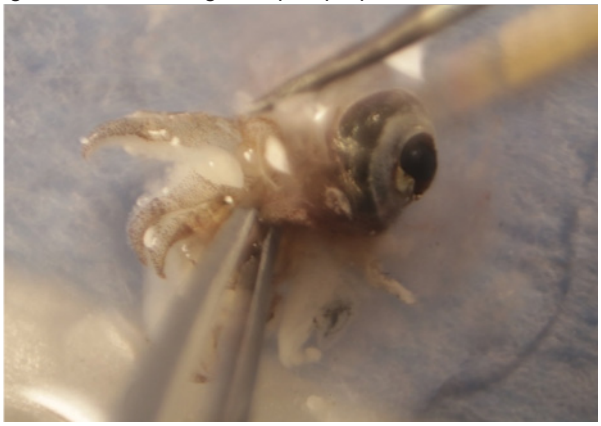

Figure 1. Dissecting *S. bandensis* (Photo credits: Eric Aker).

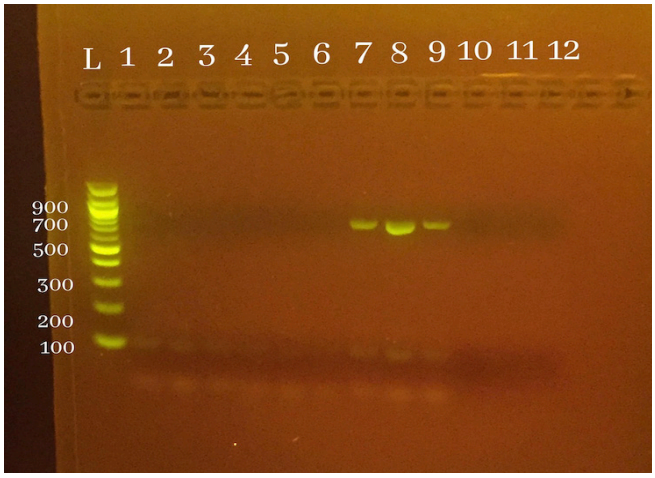

Figure 2. PCR amplification using the three DNA extraction methods with or without ink. Gel electrophoresis shows a clear band of ~710 bp for each of the three extraction methods where no ink was added (#7-10). **L**: 10 µl 100bp ladder, **1**: Phenol chloroform + 0.5 µl ink, **2**: MagListo + 0.5 µl ink, **3**: AccuPrep + 0.5 µl ink, **4**: Phenol chloroform + 1.5 µl ink, **5**: MagListo + 1.5 µl ink, **6**: AccuPrep + 1.5 µl ink, **7**: Phenol chloroform + no ink, **8**: MagListo +no ink, **9**: AccuPrep + no ink, **10**: Phenol chloroform + no primers, **11**: MagListo+ no primers, **12**: AccuPrep + no primers**.** Each PCR product lane has 2 µl 6X loading dye and 7 µl PCR products.

or the sample itself. Some common examples of inhibitors are organic compounds (such as urea, phenol, ethanol, and polysaccharides) and proteins (such as melanin and collagen) (10-12). Differences in relative amplification efficiency and changes in the slope of the exponential amplification curve compared to a non-inhibited control sample may be used to reveal decreased PCR efficiency due to the presence of such inhibitors (13). Furthermore, the concentration of the inhibitor tends to be correlated with the degree of inhibition (11).

S. bandensis ink is negatively charged and composed of heavily glycosylated proteins (specifically monomeric units of dihydroxyphenylalanine (DOPA) and/or cysteinyl-DOPA). It also includes other proteins (such as melanin), peptidoglycan, dissolved amino acids, and metals (14). The ink may inhibit PCR reactions by interacting with the DNA template or by binding to enzymes in the PCR mix. In our case, the S. bandensis DNA isolated with the DNA extraction had a purple tint. This strange coloration led the team to guess that ink was the probable inhibitor.

We guessed that the ink blocked the PCR reaction and that greater concentrations of ink would have stronger inhibitory effects. In order to test the hypothesis that *S. bandensis* ink is a PCR inhibitor, we designed a series of experiments based around the PCR amplification of the COI gene with and without the presence of ink. Appropriate negative and positive controls were included.

In addition, we hypothesized that the mucus may also have inhibitory effects due to its composition of protein-polysaccharide complexes, inorganic salts, and water. Glycoproteins help determine the mucus's properties, while glycosaminoglycans include numerous linear carbohydrate chains and do not notably contribute to the mucus's characteristics; still, more research is required to confirm these observations (15, 16).

We chose to amplify the cytochrome c oxidase subunit I (COI) gene in this study due to its effectiveness in barcoding species. COI is expressed in all cells of all eukaryotic organisms under normal conditions, and mRNA and protein are usually found at stable levels. Importantly, it is heavily conserved among members of the same species but differs significantly by several percentages among different species (17). COI is considered to be a housekeeping gene, as it maintains cellular function due to its key role in the electron transport chain. Furthermore, it plays a role in maintaining homeostasis by converting arachidonic acid to prostaglandin H2, a precursor to other biologically significant prostaglandins (18). Thus, it is very common and well-studied.

Phenol chloroform is an extraction method that has been used when PCR inhibitors are suspected or when the DNA quantity in samples is low (e.g. in forensic analysis). We predicted that this method would separate the glycosylated proteins and lipids as well as the ink and mucous from the DNA through phase separation. Typically, phenol chloroform extraction uses the Proteinase K enzyme and sodium dodecyl sulfate (a detergent) to lyse and digest cells. The addition of phenol prompts phase separation based on differences in solubility. Chloroform helps increase the efficiency of phenol, aids in the denaturation of lipids, and helps prevent phase inversion. When performed effectively, this process yields high-quality DNA in significant quantities (19). However, there are more opportunities for contamination with this method than with modern kit-extraction methods due to the greater procedure complexity and hands-on effort. One additional difficulty includes separating the interphase layer containing DNA from the aqueous and organic layers without mixing (19, 20). Despite these challenges, a modified version of phenol chloroform extraction performed on extracted cuttlefish organs in our study successfully produced viable PCR templates while modern kit-based protocols did not.

Here, we show the inhibitory properties of ink through results that depict PCR failure after back-additions of ink to DNA extracted with two kit-based extractions and phenol chloroform extraction. We also describe a detailed protocol of phenol chloroform extraction optimized for mollusk samples and explain its effectiveness in the presence of inhibitors. The article concludes by exploring this study's implications for mollusk research.

RESULTS

Ink inhibits amplification of COI from *T. fluctuosus*

To test whether ink inhibits COI amplification, we added 0 µl, 0.5 µl, or 1.5 µl of *S. bandensis* ink to extracted *T. fluctuosus* samples. We found that the addition of 0.5 µl and 1.5 µl of ink prevented amplification of COI: all three extraction methods (phenol chloroform, MagListo, and AccuPrep) failed to produce a template that showed a clear band after PCR.

Comparing #1-3 (addition of 0.5 µl ink) to #4-6 (addition of 1.5 µl ink)

	Phenol Chloroform	MagListo	AccuPrep
A260/A230 #1-3 had a lower A260/A230 ratio for MagListo and higher ratios for Phenol-chloroform and AccuPrep	#1 Average: 1.2967 #4 Average: 1.24	#2 Average: 1.0167 #5 Average: 1.4167	#3 Average: 1.0933 #6 Average: 0.78
p value	0.0607	<0.0001	<0.000138
significant?	not significant	highly significant	highly significant
A260/A280 #4-6 had lower A260/A280 ratios than #1-3 across the three extraction methods	#1 Average: 1.75 #4 Average: 1.74	#2 Average: 1.6667 #5 Average: 1.77	#3 Average: 1.7333 #6 Average: 1.6267
p value	0.1587	0.002068	0.023168
significant?	not significant	significant	significant

Comparing #1-3 (addition of 0.5 µl ink) to #7-9 (no addition of ink)

	Phenol Chloroform	MagListo	AccuPrep
A260/A230 #1-3 had lower A260/A230 ratios than #7-9 across the three extraction methods	#1 Average: 1.2967 #7 Average: 1.88	#2 Average: 1.0167 #8 Average: 1.67	#3 Average: 1.0933 #9 Average: 1.5533
p value	0.010658	<0.0001	<0.0001
significant?	significant	highly significant	highly significant
A260/A280 #1-3 had lower A260/A280 ratios than #7-9 across the three extraction methods	#1 Average: 1.75 #7 Average: 1.8167	#2 Average: 1.6667 #8 Average: 1.7667	#3 Average: 1.7333 #9 Average: 1.8
p value	0.013054	0.001892	0.075168
significant?	significant	significant	not significant

Comparing #4-6 (addition of 1.5 µl ink) to #7-9 (no addition of ink)

	Phenol Chloroform	MagListo	AccuPrep
A260/A230 #4-6 had lower A260/A230 ratios than #7-9 across the 3 extraction methods	#4 Average: 1.24 #7 Average: 1.88	#5 Average: 1.4167 #8 Average: 1.67	#6 Average: 0.78 #9 Average: 1.5533
p value	0.008044	0.000408	<0.0001
significant?	significant	highly significant	highly significant
A260/A280 #4-6 had lower A260/A280 ratios than #7-9 for phenol-chloroform and AccuPrep and a higher ratio for MagListo	#4 Average: 1.74 #7 Average: 1.8167	#5 Average: 1.77 #8 Average: 1.7667	#6 Average: 1.6267 #9 Average: 1.8
p value	0.006170	0.643330	0.283891
significant?	significant	not significant	not significant

Table 1. Analysis of spectrophotometer data. A two-tailed t-test was performed using VassarStats to determine the level of significance of the variance in purification ratios. *P*-values <0.0005 are considered statistically highly significant, *p*-values <0.025 are considered statistically significant, and *p*-values >0.025 are considered not significant. Bonferroni's correction was applied to correct for multiple comparisons by dividing the alpha value (0.05 as statistically significant) by 2 (the number of comparisons).

The negative controls (where no primers were added) did not produce a band. In contrast, samples where no ink was added produced distinct bands (**Figure 2**).

Analysis with a spectrophotometer disclosed the effects of the addition of ink to DNA-purity ratios. A ratio of about 1.8 is seen as pure for dsDNA, which generally absorbs at 260 nm. A low A260/230 ratio is often an indication of a contaminant that has an absorbance of 230 nm or less while a low A260/280 ratio is often an indication of a contaminant that absorbs at around 280 nm or less. For reference, proteins absorb at around 280 nm.

A260/A230

Samples with low A260/A230 ratios can indicate the presence of contaminants, such as organic compounds or chaotropic salts. The standard recommended ratio should exceed 1.5, with the ideal being close to 1.8. The average A260/A230 ratios for our PCR products after the addition of 0.5 µl of ink were -0.503, -0.783, and -0.707 away from the recommended 1.8 ratio, and the ratios for the addition of 1.5 µl of ink were -0.560, -0.383, and -1.02 away from the ideal for phenol chloroform, MagListo, and AccuPrep respectively. The average A260/A230 ratios where ink was not added were +0.080, -0.130, and -0.267 away from 1.8 for the three methods (**Table 1 and Figure 3**). When comparing the addition of 0.5 µl of ink to no addition of ink, we observed a significant difference in the A260/A230 ratios as indicated by *p*-values of 0.010658, <0.0001, and <0.0001 for phenol chloroform, MagListo, and AccuPrep respectively. Similar significant differences were seen when comparing the addition of 1.5 µl of ink to no addition of ink (*p*-values 0.008044, 0,000408, and <0.0001).

These results indicate that the reactions where ink was not added had purer DNA with fewer contaminants that absorb at 230 nm (the ratios were closer to 1.8). Except for MagListo, the addition of greater volumes of ink (1.5 µl instead of 0.5 µl) was correlated with lower A260/A230 ratios.

A260/A280

The A260/A280 ratio is often used to assess protein contamination of DNA, for proteins absorb at 280 nm due to their aromatic ring structures. Pure DNA samples have A260/A280 ratios greater than or equal to 1.8. The average A260/

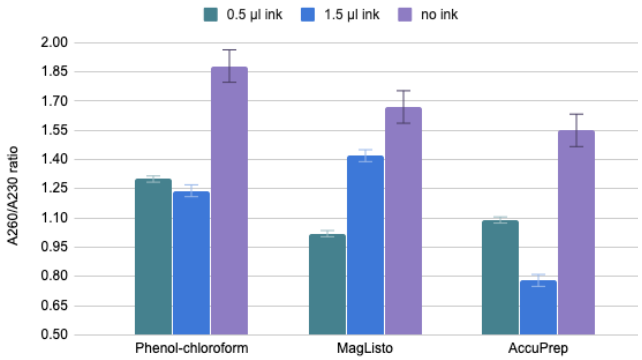

Figure 3. Addition of no ink produced better A260/A230 ratios than the addition of 0.5 µl, and 1.5 µl of ink. Analysis of the samples after PCR amplification focusing on the A260/A230 ratios shows significant contrasts between reactions where ink was added (0.5 µl or 1.5 µl) and reactions where ink was not added. The error was calculated by finding the ± standard deviation: 0.01588 for 0.5 µl ink, 0.0305 for 1.5 µl ink, and 0.083312 for no ink. The values shown are the average of three measurements with the DeNovix spectrophotometer; n=3.

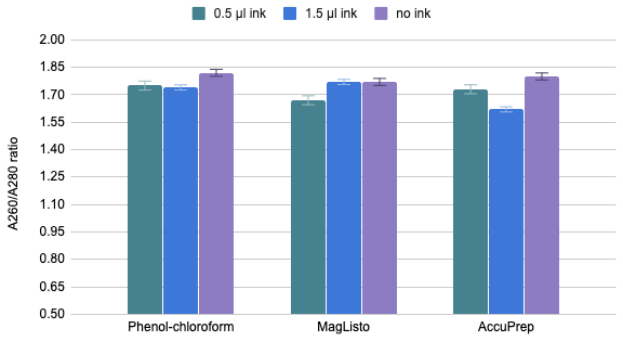

Figure 4. Addition of no ink produced better A260/A280 ratios than the addition of 0.5 µl, and 1.5 µl of ink. Analysis of the samples after PCR replication focusing on the A260/A280 ratios shows significant contrasts between reactions where ink was added (0.5 µl or 1.5 µl) and reactions where ink was not added. The error was calculated by finding the ± standard deviation: 0.0245 for 0.5 µl ink, 0.014048 for 1.5 µl ink, and 0.01913 for no ink. The values shown are the average of three measurements with the DeNovix spectrophotometer; n=3.

A280 ratios after the addition of 0.5 µl of ink were -0.500, -1.33, and -0.067 away from the recommended 1.8 limit, and the ratios for the addition of 1.5 µl of ink were -0.060, -0.030, and -0.173 away from the recommended limit (for phenol chloroform, MagListo, and AccuPrep respectively). The average A260/A230 ratios where ink was not added were +0.0167, -0.0333, and 0 away from 1.8 for the three extraction methods (**Table 1 and Figure 4**).

When comparing the addition of 0.5 µl of ink to no addition of ink, we observed a significant difference in the A260/A280 ratios for phenol chloroform (*p*-value 0.013054) and MagListo (*p*-value 0.001892) but not for AccuPrep (*p*-value 0.075168). When comparing the addition of 1.5 µl of ink to no addition of ink, a significant difference was seen in the phenol chloroform extraction (*p*-value 0.006170).

While the differences in the A260/A280 ratios among the various extraction methods were not as extreme as those of the A230/A260 ratios, the fact that the ratios for PCR samples with no ink were closer to the recommended benchmark of 1.8 indicates higher quality DNA samples.

Mucus

While the mucus may have had some inhibitory effects, they were not significant because PCR amplification was successful even with the MagListo and AccuPrep kits, which did not remove the mucus. Its composition of protein-polysaccharide complexes, inorganic salts, and water did not seem to inhibit the PCR reactions (15, 16). Further studies need to be conducted to confirm this hypothesis.

Successful amplification of COI from *S. bandensis* after extracting DNA with phenol chloroform

Phenol chloroform DNA extraction of *S. bandensis* produced samples viable for PCR. Analysis with gel electrophoresis showed clear amplification of the COI gene from the buccal and tentacle samples, with tentacle DNA having better amplification as indicated by a brighter band. In contrast, DNA templates from the eye, ovary, and ink sac produced very faint bands or no bands at all, perhaps due to the limited amount of COI in those tissues (**Figure 5**). Sanger sequencing showed notable sequence alignment of our sample with the *S. officinalis* genome from NCBI (ranging from 93.80% to 95.08 %).

Analysis with a spectrophotometer produced a value of 1.70 for the A260/230 ratio and 1.76 for the A260/A280 ratio (n=3), as well as a distinct peak in the 260nm wavelength region. The A260 value was 21.95, and there were 1098 ng of DNA per µL of the solution.

In previous runs, a slight peak at 270 nm indicated the presence of residual phenol. The addition of more chloroform counteracted this issue by dissolving the phenol while allowing theDNA to remain in the aqueous layer. While phenol has been shown to denature DNA polymerases, no such properties were noted in this experiment, as the COI was amplified and produced a clear band on a gel as shown in **Figure 2** and **Figure 5** (22).

DISCUSSION

This study shows the effectiveness of phenol chloroform in removing inhibitors from cephalopod samples to produce a viable template for PCR. This can be seen from the distinct bands produced on the gel (**Figure 5**). The brightness of the tentacle band is likely the result of the presence of many copies of the COI gene in tentacle cells due to the high energy metabolism of muscle.

Figure 5. COI gene amplified from the buccal and tentacle samples. The 1.5% agarose gel was loaded with 2 µl 6X loading dye mixed with 8 µl of PCR product. **L**: 10 µl 100bp ladder, **1**: unknown sample, **2**: eyeball, **3**: buccal mass, **4**: tentacle, **5**: ovary.

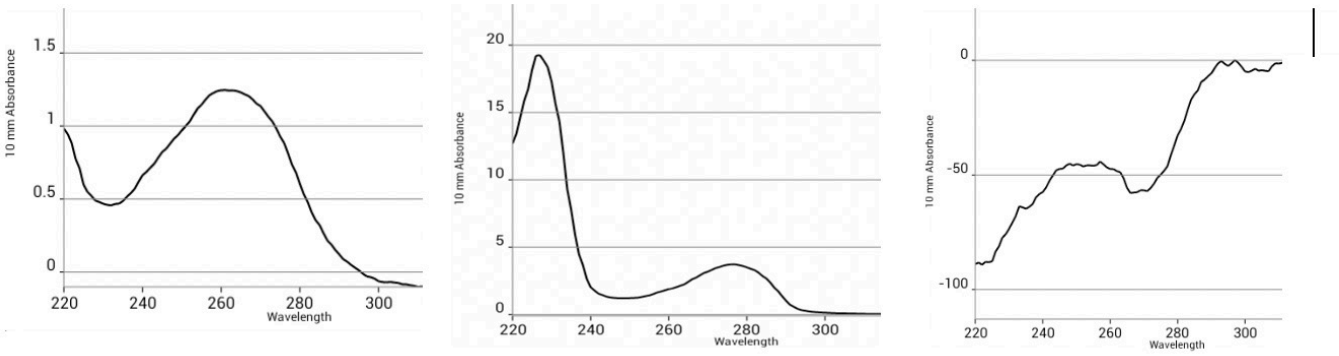

Figure 6. Ink affects spectrophotometer graphs showing wavelength versus 10 nm absorbance. (left to right): Graph generated with *S. bandensis* DNA extracted using the phenol chloroform method, graph generated with *S. bandensis* DNA extracted using the Accuprep kit, and graph generated from a pure ink sample from an isolated *S. bandensis* ink sac.

Because phenol chloroform is immiscible with water, mixing it with the sample permitted the formation of distinct phases due to differences in density. The heavily glycosylated ink entered the dense organic layer, while the nucleic acids entered the less dense aqueous layer. This phase-separation was critical in isolating the DNA and preventing ink contamination of the sample. Other extraction methods—specifically kit-based ones—proved effective in isolating *T. fluctuosus* DNA (no ink), but not *S. bandensis* when ink was present. Analysis of isolated *S. bandensis* samples with a spectrophotometer showed that phenol chloroform extraction produced a clear peak at 260nm, while the MagListo extraction had a high peak at approximately 230nm, a lower peak at 280nm, and an upward-sloping trend between 230nm and 280nm. The Accuprep extraction produced a low peak at about 250nm and a much higher peak at about 290 nm; the plotted data was also irregular, as it did not create smooth curves (**Figure 6**). When using kit-based methods, the ink may have prevented the nucleic acids from effectively binding to the silica gel membrane or flowing through the spin column. More data is needed to support these speculations.

Also, adding ink to *T. fluctuosus* illustrates that ink likely causes PCR inhibition. While all three extraction methods—phenol chloroform, MagListo, and Accuprep—proved effective in isolating samples for PCR, the addition of ink following purification impeded PCR amplification for all three methods (**Figure 2**). By forming a reversible complex with the DNA polymerase, the melanin in the ink may have altered the DNA polymerase, preventing it from binding to the template and elongating the strand (21). Other glycoproteins in the ink may have also compromised the effectiveness of PCR by binding to cofactors or by blocking reaction components (10, 13).

When isolating *T. fluctuosus* with phenol chloroform, the purity of the sample may have been further away from the ideal than samples isolated with MagListo and Accuprep due to residual components left in the product, such as phenol, chloroform, or salts. Contamination may be minimized by taking more care in pipetting the supernatant, centrifuging at higher speeds, or performing additional purification procedures. Other solutions could be performing additional washes or one more round of chloroform extraction; however, this could result in a decrease in the quantity of DNA. The data suggests that phenol chloroform may not be the best extraction method for isolating DNA from tissues without PCR-inhibiting components; nevertheless, it could be superior when inhibitors are present.

These results are notable because an effective procedure to produce PCR templates in the presence of inhibitors is crucial to galvanizing more studies of cephalopods and other organisms whose samples may include interfering compounds. Advances in cephalopod genomics could notably improve the efficiency and effectiveness of cephalopod research by providing scientists with a comprehensive library of the species' genes, identifying critical protein identities, and improving the effectiveness of gene analysis (1). This information would be of significant value to those seeking to understand cephalopod gene expression and mutations as well as to those studying comparative development of metazoans. Future research into cephalopod genomics could also reveal new molecular regulatory mechanisms and protein expression patterns (1).

Analysis on a molecular level of the impact of changing oceanic conditions—such as ocean acidification, warming of waters, and lower oxygen tension in oxygen minimum layers—on mollusks can help predict their responses to new selective pressures (4, 23, 24). Mollusks could also be used to study the broader implications of a changing climate, as their intricate evolutionary history and prevalence in oceanic habitats around the world could offer insights into the adaptations and diversification of traits (3, 4).Furthermore, cephalopods are of special interest to many researchers due to their unique adaptations (such as chromatophores, differentiated brains, and specialized sensory organs) and intricate structures, including vascular systems and neurological mechanisms (4). Studying these features could provide insights into homologous structures and similar regulatory mechanisms in other organisms.

Moreover, members of the Mollusca phylum, especially cephalopods, are used in medical research for developing biologically active substances, in toxicology studies of pollutants and for commercial uses in dietary supplements and cosmetics. Biological compounds isolated from the tissues and ink of cephalopods have been shown to exhibit antioxidant properties; besides that, they may increase lipid metabolism and inhibit angiotensin-converting enzymes involved in high blood pressure and impaired homeostasis (5). Improved procedures to isolate cephalopod DNA would prove useful for these objectives.

Ultimately, the ability to remove inhibitors without compromising DNA quality is crucial to developing isolates that can be amplified. The control experiments performed in this study could serve as a model for experiments aiming to determine the cause of PCR inhibition.

While the control experiments showed that ink was the probable inhibitor, future studies are needed to further analyze the specific components of ink that may be causing this inhibition. Other future studies could examine the effectiveness of phenol chloroform extraction in removing inhibitors from other mollusk samples.

METHODS

Ink Inhibition Experiment

A multi-part control protocol was designed to establish the cause of PCR inhibition by determining whether ink caused the failed amplification. The same PCR conditions and primers as were used for the *S. bandensis* PCR amplification were used to amplify COI from Turbo fluctuosus, which has no ink. Three different extraction methods—phenol chloroform extraction, genomic DNA extraction with Bioneer's MagListo kit, and genomic DNA extraction with Bioneer's AccuPrep kit—were used.

The MagListo kit involves lysing the sample with Proteinase K and RNase and then using chaotropic agents to facilitate the absorption of DNA onto magnetic nano beads. A magnetic plate and a series of washes are used to isolate the DNA. The Accuprep kit involves a series of centrifugations following additions of a tissue lysis buffer, Proteinase K, RNase A, and a binding buffer. After adding absolute ethanol, the sample is washed to remove residual components. Phenol chloroform extraction uses proteinase K to digest tissue and then phenol and chloroform to facilitate phase separation (see the introduction for a thorough explanation of the phenol-chloroform method).

The independent variable for each extraction methods was the amount of ink added (0.5 µl or 1.5 µl). The positive controls were the extracted DNA samples with no addition of ink. The negative controls were the PCR reactions performed without the addition of primers.

First, the sea snail was anesthetized by covering it entirely with 20mM MgCl2 in a beaker for 10 minutes at room temperature (25). The tissue was cut away and put into a tube, where scissors were used to cut it into even smaller pieces. For each extraction method, about 30-60 mg of tissue was used. The ink was obtained from an isolated S. bandensis ink sac.

Before use in PCR, 40 µl of extracted DNA from each of the three methods was cleaned using the AccuPrep PCR Purification Kit from Bioneer according to the manufacturer's protocol. After purifying the template DNA, the three following PCR reactions were prepared using *T. fluctuosus* tissue samples: Phenol chloroform extracted DNA, MagListo extracted DNA, and AcuuPrep extracted DNA. These reactions were done with either 0.5 µl ink, 1.5 µl ink, no ink, and a negative control containing no primers or ink.

Each reaction contained 26 µl of nuclease-free water (30 µl for the negative controls), 4 µl of 10x buffer, 2 µl dNTPs,2 µl of MgCl2, 2 µl of the forward COI primer (omitted for the negative controls), 2 µl of the reverse COI primer (omitted for the negative controls), 1 µl of hot start Taq polymerase, 1 µl of the extracted DNA template combined for a 40 µl total volume in each PCR tube. The PCR products were then analyzed using gel electrophoresis and a spectrophotometer.

Phenol chloroform extraction

All reagents were purchased from Thermo Fisher Scientific. Phenol chloroform extraction was performed to extract DNA samples from cuttlefish organs including the tentacles, muscle from ovaries, eye, stomach, buccal parts, and ink sac tissue. The PCR was performed on a variety of organs to determine which ones resulted in the highest PCR efficiency based on the amount and quality of product. It was predicted that tentacle and buccal samples would be best due to the high metabolic activity of those organs and the high density of muscle cells. The procedure was revised chiefly by Johan Sosa and Eric Espinosa, Ph.D. and optimized using marine snail samples.

After isolating the extracted organs into 25-50 mg tissue samples in separate microcentrifuge tubes, 500 µl of TRIzol (which is composed of phenol, guanidine isothiocyanate, and red dye) was added to each sample to break up the proteins and cell membranes. This reagent was chosen due to its ability to dissolve organic compounds in a solution and to sequentially isolate DNA, RNA, and protein without compromising the structure of the nucleic acids (26). The phenol in TRIzol forms droplets throughout a solution when mixed and due to its lower polarity than water, causes proteins in the water phase to denature and enter the phenol droplets, thus separating nucleic acids from protein.

After the addition of TRIzol, the sample was homogenized. Following incubation for 5 minutes at room temperature to permit the complete dissociation of nucleoprotein complexes, 400 µl of 12.4 M chloroform was added, and the samples were kept at room temperature for another 2-3 minutes. The homogenate was allowed to separate into three distinct layers: a bottom organic layer containing proteins and some DNA, an interphase containing DNA, and a clear upper aqueous layer containing RNA. After centrifugation for 10 minutes at 12,000

rpm, the layers became more distinct. The upper RNA layer was transferred to a new tube by pipetting and discarded. Afterward, 300ul of a solution of 20mM Tris (pH 8), 1% SDS, and 6M urea was added to the remaining sample before centrifuging again for 5 minutes at 12,000 rpm to separate the DNA and organic layers. The DNA was isolated by pipetting into a separate tube and recovered through mixing with 200ul 17.1 M ethanol. The organic layer remained in the original tube and was not used. The separated DNA was purified using the AccuPrep PCR Purification Kit from Bioneer.

The PCR reactions to amplify COI were performed using 1 µl of each primer, 13 µl of nuclease-free water, 2 µl of 10X buffer, 0.5 µl of hot start Taq polymerase, 0.5 µl of the extracted DNA template, 1 µl of MgCl2, and 1 µl of dNTPs (for a total volume of 20 µl). The primers used were the universal cytochrome c oxidase subunit I gene (COI) primers LCO1490: 5'-ggtcaacaaatcataaagatattgg-3' and HC02198: 5'-taaacttcagggtgaccaaaaaatca-3 (27). PCR reaction conditions were as follows: 98°C for 1 min, 98°C for 5 seconds, 48°C for 15 seconds, 68°C for 1 min, repeat steps 2-4 29 more times, bring the temperature up to 72°C for 5 min, 10°C until the end.The Zymo Research DNA Clean and Concentrator kit was used to clean the PCR product before sending it to Elim Biopharmaceuticals for Sanger sequencing.

ACKNOWLEDGEMENTS

I acknowledge the members of the cuttlefish community project at BioCurious for their support and dedication to cephalopod research, especially Johan Sosa, Maria Chavez, and Eric Espinosa Ph.D., who provided valuable feedback on this study. I would also like to thank Jay Hanson for his help with editing and submitting the manuscript, Sum-Yan Ph.D. for her leadership of cuttlefish PCR reactions during community meetings, and Eric Aker for taking the cuttlefish dissection photo.

Received:
Accepted:
Published:

REFERENCES

1. Alberti, Caroline B., *et al*. "Cephalopod genomics: A plan of strategies and organization." *Standards in Genomic Sciences*, vol. 7, no. 1, 2012, pp. 175-88.
2. Reygondeau, Gabriel. "Current and future biogeography of exploited marine exploited groups under climate change." Predicting Future Oceans, 2019, pp. 87-101.
3. Rodhouse, Paul G. "Role of squid in the Southern Ocean pelagic ecosystem and the possible consequences of climate change." *Deep-Sea Research Part II: Topical Studies in Oceanography*, vol. 95, 2013, pp. 129-38.
4. Xavier, Jose C., et al. "Future challenges in cephalopod research." *Journal of the Marine Biological Association of the United Kingdom*, vol. 95, no. 5, 2014, pp. 999-1015.
5. Besednova, Natalya N., *et al*. "Cephalopods: The potential for their use in medicine." Russian Journal of Marine Biology, vol. 43, no. 2, 2017, pp. 101-10.
6. Hallinan, Nathaniel M., and David R. Lindberg. "Comparative analysis of chromosome counts infers three paleopolyploidies in the Mollusca." *Genome Biology and Evolution*, vol. 3, 2011, pp. 1150-217.
7. Adam, W. "Sepia bandensis." Bulltin du Musee royal d'Histoire naturelle de Belgique, vol. 15, no. 18, 1939b, pp. 72-78.
8. Hanlon, Roger T., and John B. Messenger. "Cephalopod Behavior." Cambridge: Cambridge University Press, 1996.
9. Huggett, Jim F., *et al*. "Differential susceptibility of PCR reactions to inhibitors: an important and unrecognised phenomenon." *BMC research notes*, vol. 1, 2008, p. 70.
10. Schrader, Christina, *et al*. "PCR inhibitors - occurrence, properties and removal." *Journal of Applied Microbiology*, vol. 113, no. 5, 2012, pp. 1014-26.
11. Rossen, Lone, *et al*. "Inhibition of PCR by components of food samples, microbial diagnostic assays and DNA-extraction solutions." *Journal of Applied Microbiology*, vol. 113, no. 5, 2012, pp. 1014-26.
12. Ra˚dstro¨m, Peter, *et al*. "Pre- PCR processing: strategies to generate PCR- compatible samples." *Molecular Biotechnology*, vol. 26, 2004, pp. 133-46.
13. Opel, Kerry L., *et al*. "A Study of PCR Inhibition Mechanisms Using Real Time PCR." *Journal of Forensic Sciences*, vol. 55, no. 1, 2010, pp. 25-33.
14. Derby, Charles D. "Cephalopod Ink: Production, Chemistry, Functions and Applications." *Marine Drugs*, vol. 12, no. 5, 2014, pp. 2700-30.
15. Gottschalk, Alfred. Glycoproteins: Their composition, structure, and function. 2nd ed., Elsevier Pub, 1972.
16. Davies, Mark S., and Stephen J. Hawkins. "Mucus from Marine Molluscs." *Advances in Marine Biology*, 1998, pp. 1-71.
17. Bucklin, Ann, *et al*. "DNA Barcoding of marine metazoa." *Annual Review of Marine Science*, vol. 3, 2011.
18. Morita, Ikuo. "Distinct functions of COX-1 and COX-2." *Prostaglandins and Other Lipid Mediators*, vols. 68-69, 2002, pp. 165-75.
19. Köchl, Silvano, *et al*. "DNA Extraction and Quantitation of Forensic Samples Using the Phenol–Chloroform Method and Real-Time PCR." *Forensic DNA Typing Protocols*, n.d., pp. 13-30.
20. McKiernan, Heather E., and Phillip B. Danielson. "Molecular Diagnostic Applications in Forensic Science." *Molecular Diagnostics*, 2017, pp. 371-94.
21. Eckhart, Leopold., *et al*. "Melanin Binds Reversibly to Thermostable DNA Polymerase and Inhibits Its Activity." *Biochemical Biophysical Research Communications*, vol. 271, no. 3, 2000, pp. 726-30.
22. Katcher, Harold L., and I. Schwartz. "A distinctive property of Tth DNA polymerase: enzymatic amplification in the presence of phenol." *Biotechniques*, vol. 16, 1994, pp. 84-92.

23. Bograd, Steven J., *et al.* "Oxygen declines and the shoaling of the hypoxic boundary in the California Current." *Geophysical Research Letters*, vol. 35, no. 12, 28 June 2008, pp. 1-6.
24. Parker, Laura M., *et al.* "Predicting the Response of Molluscs to the Impact of Ocean Acidification." *Biology*, vol. 2, no. 2, 2013, pp. 651-92.
25. Messenger, John B., *et al.* "Magnesium Chloride as an anaesthetic for cephalopods." *Comparative Biochemistry and Physiology Part C: Comparative Pharmacology*, vol. 82, no. 1, 1985, pp. 203-05.
26. Rio, Donald C., *et al.* "Purification of RNA using TRIzol (TRI reagent)." Cold Spring Harbor Protocols, vol. 6, 2010.
27. Folmer, Ole, *et al.* "DNA primers for amplification of mitochondrial Cytochrome C oxidase subunit I from diverse metazoan invertebrates." *Molecular marine biology and biotechnology*, vol. 3, pp. 294-99.

JOURNAL OF
EMERGING INVESTIGATORS

Article

Analysis of the Exoplanet HD 189733b to Confirm its Existence

Pratham Babaria[1] & Ethan Chandra[1]
[1] Harmony School of Endeavor, Austin, Texas

SUMMARY

In this study, we examined the orbital periods, photometry, and radial velocity of one exoplanet in the HD star system: 189733 b. We constructed a high caliber exoplanet transit detection tracker that acts as a means to analyze the data constituted of the Raw Science images that we obtained from a DSLR camera. We used the BATMAN Python programming package to convert our data to light curves and a radial-velocity model. The radial velocity data was taken from multiple high precision research studies, which were then converted to a sinusoidal graph portraying the radial velocity with respect to time. Chi-square tests were performed on the data in order to examine the likelihood that observation was due to mere chance. We hypothesized that the creation of a DSLR camera star tracker would produce results that support previously established studies. The results of our studies were statistically significant and supported our hypothesis and previous studies. This study demonstrates the importance of accurately using the radial velocity and photometry data from high-precision research studies.

INTRODUCTION

Exoplanets are planets that orbit stars other than the Sun (1). In this study, we aimed to detect exoplanets around the HD 189733 b star system using the transit method of planet detection. We built upon an existing methodology that will make exoplanet detection easier and much more efficient for astronomers. By doing so, we can exponentially increase the rate at which we discover exoplanets and make it much faster and simpler. By making equipment that is fast, economical, and usable, civilian scientists will also be able to access this technology. This would not only make exoplanet detection far faster but would also result in increased engagement with exoplanetary science for people of all ages.

The technology we employ is known as a barn door model star tracker. A barn door star tracker is an economical exoplanet detector that relies on an Arduino Uno and a bipolar stepper motor to control the platform where a camera rests. Between these two platforms there is a threaded rod that is spun by the motor. Additionally, using the Arduino IDE software application, we are able to program the motor to move at an identical rate that opposes the rotation of the Earth, resulting in a raw image without motion blur.

Here, we show that the barn door star tracker produces results remarkably similar to advanced space and ground based telescopes, such as the Hubble Space Telescope, Kepler Space telescope, or the Gemini Planet Imager. These research surveys of our universe require significant expertise to operate and use, which make these methods of exoplanet detection out of reach for aspiring scientists and the general populace. Even though these telescopes undoubtedly have better quality and pictures, we hypothesized that our star tracker would produce transit curves similar to those of professional scientific research studies.

Many detection methods for exoplanets exist (2), but the one that has been used most frequently by astronomers and physicists is “the radial velocity method” (3). The radial velocity method relies on detecting the “wobble” of a star, i.e. the movement of a star as it revolves around a center of mass, as a result of the gravitational attraction between the exoplanet and the star. If the radial velocity is cyclical, there is evidence that an unseen planetary companion exists in orbit around the star.

Even though the radial velocity method (4) has been used to detect a vast majority of exoplanets, recently, however, the photometric analysis method has become increasingly useful for the same purpose. Photometry helps scientists discover exoplanets through the obstruction of light by the host star of an exoplanet. Because of this small dip in the measured light intensity, we can then convert this data to a light curve graph. If the resulting curve is cyclical, we can conclude that there is an unknown planetary companion (or orbital body) in orbit around the star of significance. Here, our study was able to analyze and confirm the existence of an already existing extrasolar planet (5) with results similar to the ones acquired from a previous study on the HD 189733 star system. One of the most important steps to our project was to measure the planet’s orbital period through the use of Kepler’s third law (6) and to measure the length of the planetary axis.

Since the exoplanet that we observed has a small orbital radius and a relatively large mass compared to other planets, it has a short orbital period. These planets are known as “Hot Jupiters.” By examining this hot Jupiter, we found that the results -- collected through the observation of an exoplanet in transit around a star using a DSLR camera -- is in direct correlation to a previously conducted study. The results of our study very closely mirror the result of the previous study.

We hypothesized that our development of a star tracker

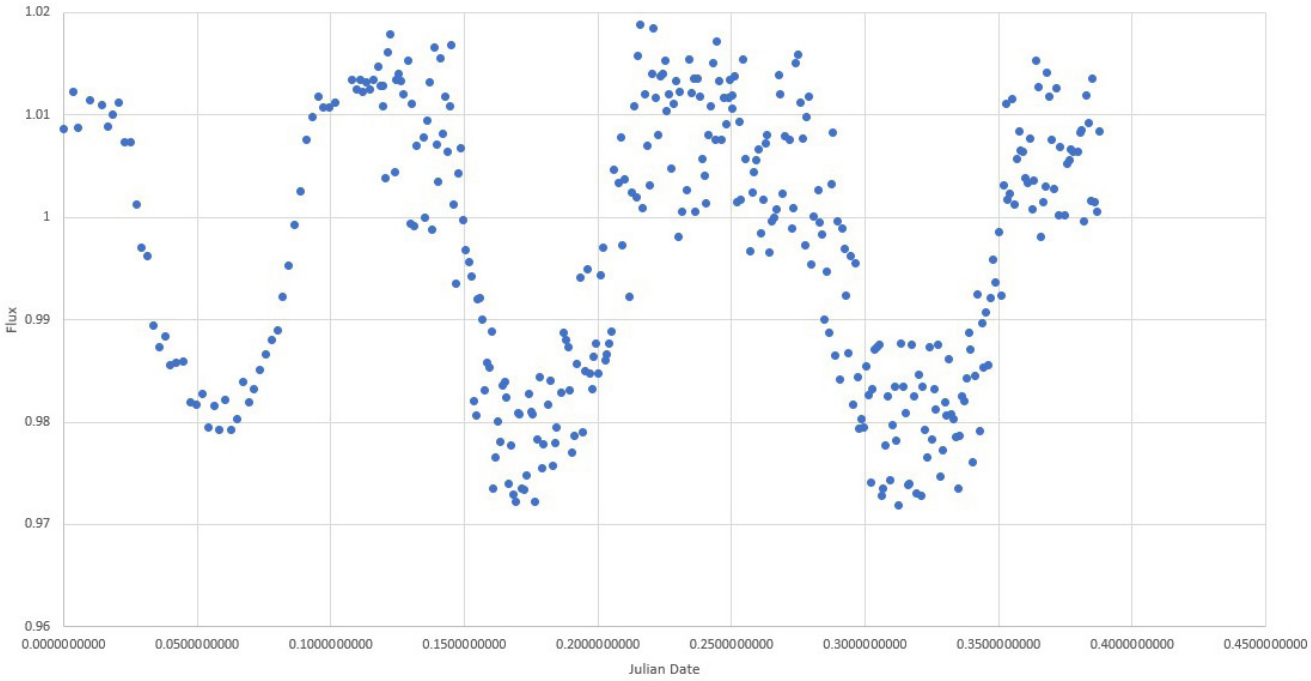

Figure 1. Shows the photometric/light curve of HD 189733b from our first field observation. The cyclical nature of this graph shows that there is indeed an exoplanet that orbits the star. Julian time was converted such that the first value was zero. The succeeding values represent the difference between the current and preceding Julian Time values.

will have similar results to that of the modern exoplanetology technology. The results of our studies were statistically significant, so it supported both our hypothesis and previous studies on the subject. Our study was able to confirm the feasibility of detecting exoplanets by using a far more economical method that produced almost the same results as other studies (7).

This work may help increase the rate at which new exoplanets are found and therefore will help astronomers and physicists discover new worlds that may even be habitable (8) and ready for future colonization by humanity. Furthermore, by learning about exoplanets, we can learn about Earth (and humanity's) place in the universe.

RESULTS

We found that it is feasible to detect exoplanets using inexpensive and readily available technology.

Therefore, our studies show that it is possible for exoplanets within 100 light years from earth to be detected using a barn door star tracker. The radial velocity (4) and photometric analysis surveys that we conducted on the exoplanets supported the existence of hot Jupiters. The data presented here produced a cyclical photometry graph in agreement with the results of previous studies.

Light-Curve Analysis

We began by calculating the radius of the planet. The photometry light curves for HD 189733 b were normalized to a baseline value of 1.0 in order to make the data more readable and understandable. The star in consideration is a K-type star, which implies that it has a solar radius of between 0.7 - 0.96. **Equation 1** describes the relationship between the ratio of the flux change, ΔF, to normalized flux, F, and the radius of the planet squared, R^2_p, to the radius of the star squared, R^2_s, from the point of view of the observer.

Equation 1: $$\Delta F / F = R^2_p / R^2_s$$

Our results support our initial hypothesis as they not only agree with some of the results of a previous study (9), but also shows our predicted photometry and radial velocity curves were accurate (**Figure 1**). We used a Chi Squared ($\chi 2$) test on the data that we gathered. We found that the results of the test were statistically significant and showed a similarity with previous literature values.

Chi-Squared Results

The values in the flux graph indicates that there is an exoplanet around the star we were observing. This is because the exoplanet produced a light curve that was cyclical in nature. Our null hypothesis is that H_0: $\mu = 1$, which implies that there is no exoplanet because of a uniform distribution of points. Our alternative hypothesis was that H_A: $\mu \neq 1$, which suggests that the values do not always center one, and instead, they fluctuate.

The null hypothesis simply states that the values center around a range of values close to one, which would indicate that the exoplanet was transiting around a star. The alternate

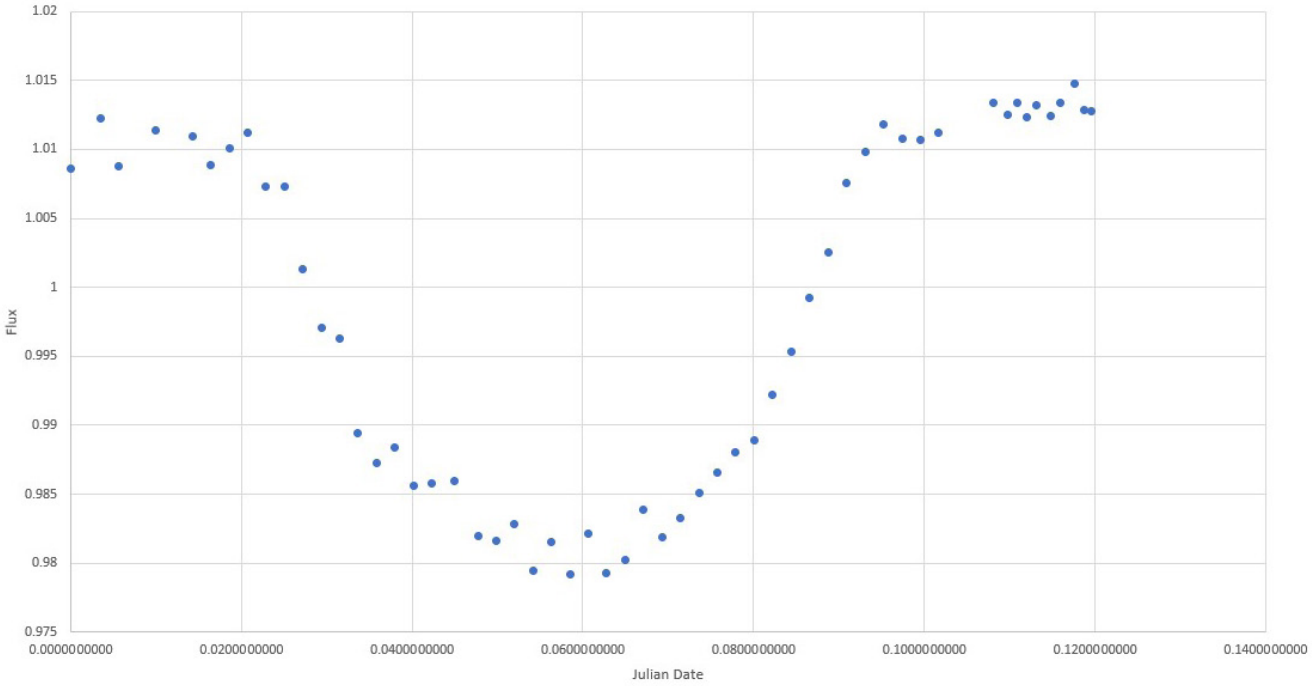

Figure 2. This is the second field observation of the exoplanet. Once again, the graph is shown to be cyclical in nature. Therefore, both of our field observations show that there is an exoplanet in existence.

hypothesis states that the exoplanet would not center around a mean value of one and would not indicate the existence of an exoplanet.

The $\chi 2$ statistic was approximately 22352. The degrees of freedom that we used was 372 (as there were 373 categories). The *p*-value that was calculated was less than 0.05, so we supported our alternative hypothesis and rejected the null hypothesis. This supported our original hypothesis.

DISCUSSION

In this study, we did detect a statistically significant shift in the images obtained by our barn door star tracker. This supported previous studies on the same exoplanet.

This new method will be helpful in discovering more yet unknown exoplanets and show that many studies on exoplanetology must be revamped with the new methods and tools at our disposal. The results that we acquired show the immense importance of updating information about planetary bodies and to actively change information based on new results and discoveries.

A shift in the orbital radius of the planet from when it was last discovered shows that there is a statistically significant shift with the flux change of the exoplanet. This is primarily because of Kepler's third law (**Equation 2**), which describes a proportional relationship between the square of the orbital period (T) and the cube of the semi-major axis (a) (10).

Equation 2: $T^2 \propto a^3$

Because the barn door star tracker that we used to obtain these results was not as sophisticated as professional star trackers, we were limited in the range of opportunities we had to discover and track exoplanets. The main exoplanets that we tracked were ones that were less than 100 light years from the earth.

The technology we had at our disposal made it nearly impossible for us to track and analyze exoplanets which were a significant distance away from our position. We believe that this is one significant drawback of this approach to discover new exoplanets.

Furthermore, the results that we obtained were primarily used to demonstrate the feasibility of using technology that is less advanced than professional telescopes, star trackers, and spectrometers at professional universities, laboratories, and observatories. Great emphasis must be put on the fact that our star tracker does not serve as a replacement of professional star tracker, but rather as a supplement to aid and accelerate the pace at which we detect more exoplanets.

The star tracker technology that we advocate will help civilian scientists help far more in the discovery of exoplanets. We firmly believe that incorporating this star tracker as a lab instrument will greatly help with the discovery of new exoplanets and will help both professional and amateur scientists discover more about the universe.

METHODS

We focused primarily on the transit method (photometric analysis). The transit method is used to observe the shift in brightness as the exoplanet orbits around the star, and radial velocity is observed as the change in frequency (11) caused

Amateur Star Tracker	Professional Star Tracker
The photometric curve produced by a custom made star tracker closely mirrored the one in a previous research study.	Professional telescopes and star trackers can create photometric curves of even dim stars.
Custom star-trackers can only produce the photometric curve of highly visible stars such as the HD star system.	Professional telescopes can detect the radial velocity of any star.
Homemade star trackers cannot plot the radial velocity graph of a star.	Observatory telescopes can easily detect any anomaly in the data and relay it to a team of professionals.

Table 1. Depicts key differences between our amateur star tracker and a professional star tracker. Although our star tracker is more economical, it lacks some of the sophisticated machinery possessed by professional ones. However, ours is able to be used when exoplanets are 100 light years from the earth or less.

by stellar "wobble."

Data Collection

We gathered data through the creation of a star tracker, built using an Arduino microcontroller, stepper motors, and 3D printed parts. The star tracker was created to gain accurate data, enabling us to follow the star and counteract the rotation of the earth. We determined that the tracker needs to move approximately 0.25 degrees per minute, so to accurately move the star tracker, we used bipolar stepper motors and a screw/gear system. In the Arduino programming language, we initialized the ports to specific coils in the stepper motor and set the speed to move at the rate stated previously. Then, we used a Canon DSLR camera with a ball-socket mount and attached it in the center of the apparatus to acquire images. The main reason for following the star was to acquire the flat, dark, and biased frames that were then calibrated.

Data Calibration

We then calibrated our data to acquire the flat, dark, and biased images. A flat image is a frame that determines the correction factor when pixels are exposed to the same amount of light. To acquire this image, we applied a uniformly even source of light with normal exposure time and capture the image. A bias image is a frame, captured with short exposure time and with the camera lens attached, that determines the amount of noise in a camera. This inherent noise is caused by the accumulated electron frequency of the Charged-Coupled Detector (CCD) chip. A dark image is a frame that contains this "bias" and is removed to correct the image to get a pure, dark image. From these frames, we created MasterDark, MasterFlat, and MasterBias images. These master frames were processed through a python program that stacked and averaged all of the images to create an accurate, unbiased image(with the formula below) to be analyzed through AstroImageJ.

The star tracker was calibrated to point towards the star (and exoplanet) that was being observed. A particular date from the exoplanet transit database (12) was picked in order to pick the most opportune time to detect the exoplanet. The star tracker was calibrated to take astronomical photographs every 30 seconds during the entire period of the transit. The image frames were then stacked on an exoplanet imaging software known as SharpCap to be able to compare the values. The result was the exoplanet transit curve.

Data Analysis/Confirmation

We used AstroImageJ to process the data. AstroImageJ is a data imaging graphical user interface that reduces and simplifies the data to create a photometric light curve. To create this light curve, AstroImageJ picks a comparison star that does not contain an exoplanet and compares the change of flux (from a baseline value) in relation to comparable stars. We also conducted research on data previously collected by professional astronomers and physicists. We compared our data to this previously conducted research to ultimately validate our hypothesis.

The BATMAN python programming package was also used in order to generate a curve of best fit for the comparison graph that we generated (13).

ACKNOWLEDGMENTS

We would like to thank the following individuals for helping us with the project: Dr. Eric J. Brugamyer, for providing us with the resources to experiment with data; Professor Yetkin Yildirim from Rice University for providing us with the opportunity to obtain tools necessary to conduct research; Tjiamin Chandra, Software Engineer; Deepak Babaria,

Electrical Engineer.

We would like to thank Rice University for providing us with this excellent research internship.

Received: April 15, 2020
Accepted: September 15, 2020
Published: September 21, 2020

REFERENCES

1. UW Departments Web Server, depts.washington.edu/naivpl/sites/default/files/hz.shtml
2. "Wobbly Stars: The Astrometry Method." *The Planetary Society*, www.planetary.org/explore/space-topics/exoplanets/astrometry.html.
3. Brugamyer, Erik, et al. "Silicon and Oxygen Abundances in Planet-Host Stars." *NASA/ADS,* ui.adsabs.harvard.edu/abs/2011ApJ...738...97B/abstract.
4. "Communications System." What Is the Doppler Effect?, www.qrg.northwestern.edu/projects/vss/docs/communications/3-what-is-the-doppler-effect.html.
5. International Space Hall of Fame, *New Mexico Museum of Space History*, www.nmspacemuseum.org/halloffame/detail.php?id=123.
6. The Editors of Encyclopaedia Britannica. "Kepler's Laws of Planetary Motion." *Encyclopædia Britannica*, Encyclopædia Britannica, Inc., 31 Oct. 2019, www.britannica.com/science/Keplers-laws-of-planetary-motion#ref214571.
7. Díaz, Rodrigo F. "Modelling Light and Velocity Curves of Exoplanet Hosts." *SpringerLink*, Springer, Cham, 1 Jan. 1970, link.springer.com/chapter/10.1007/978-3-319-59315-9_11.
8. Kaltenegger, Lisa, and Nader Haghighipour. "Calculating the Habitable Zone of Binary Star Systems. I. S-Type Binaries." *NASA/ADS*, ui.adsabs.harvard.edu/abs/2013ApJ...777..165K/abstract.
9. Lu, Wenxian, et al. "Light-Curve and Radial Velocity Study of the Contact Binary BD +42 2782." *NASA/ADS,* ui.adsabs.harvard.edu/abs/2007AJ....133..255L/abstract.
10. Kepler's Third Law of Planetary Motion. (n.d.).Retrieved from https://www-istp.gsfc.nasa.gov/stargaze/Skepl1st.html
11. "Doppler Shift." NASA, NASA, imagine.gsfc.nasa.gov/features/yba/M31_velocity/spectrum/doppler_more.html.
12. Chu, Seng. "Chi-Squared Test for Independence in Python." *Coding Disciple*, 4 Mar. 2018, codingdisciple.com/chi-squared-python.html.
13. Kreidberg, Laura. Batman: BAsic Transit Model CAlculatioN in Python, www.cfa.harvard.edu/~lkreidberg/batman/.

JOURNAL OF
EMERGING INVESTIGATORS

Article

An analysis of the distribution of microplastics along the South Shore of Long Island, NY

Kaylee Sanderson[1] and Mary Simons[1]
[1] Seaford High School, Seaford, New York

SUMMARY

Plastic pollution has exponentially increased in recent years, becoming an international concern. Microplastics, or plastic particles measuring less than 5 mm in length, have consequently become ubiquitous and harmful in the marine environment, ultimately putting the biosphere at risk. Scientists recognize the importance of understanding the distribution of microplastics in the environment to develop policy and tools to combat this issue and promote sustainability. In this experiment, we sought to identify the concentrations of microplastic pollution in the sand of various locations along the coastline of the South Shore of Long Island, New York. This study involved an initial collection of sand followed by microplastic extraction with sodium chloride, filtration, and quantification via microscopy. We hypothesized that there would be a higher concentration of microplastics in the sand of the beaches that are closer in proximity to New York City whereas the locations farthest from the city would have lower concentrations of the contaminants. Based on the resulting p-value of 0.75, we concluded that there were no statistically significant differences between the numbers of microplastics collected from each sampling location. However, since microplastics were retrieved from each of these four sampling locations, there is evidence that microplastics are present along the South Shore, which is important to further research.

INTRODUCTION

First escalating after World War II to meet the demands of society, plastic production has exponentially increased from 2.3 million tons in 1950 to 448 million tons in 2015, with this number expected to double by 2050 (1). Combined with the lack of recycling efforts and an increasing "throw-away" consumer culture among society, plastics continue to rapidly accumulate on Earth. For instance, a recent report deduced that European countries recycle between 35% and 45% of their plastic waste, while the United States only recycles a mere 10% (2). This statistic not only highlights the severity of this issue in the United States, but it also depicts a pressing problem that is plaguing the planet, as a shocking majority of plastic waste is not recycled and is left to pollute the Earth. As a result of mediocre recycling practices, the remaining abundance of plastic waste accumulates in landfills or the natural environment and typically enters the marine environment (3). Every year, about 8 million tons of plastic waste escapes into the oceans from coastal nations, which is the equivalent of placing five garbage bags of trash on every foot of coastline of the world (1). Now ubiquitous in the marine environment, plastics put the marine ecosystem at risk.

Once circulating in the world's oceans, plastics can take hundreds of years to fully degrade (1). However, this plastic debris breaks down into smaller particles relatively quickly due to the abundance of wind, sunlight, and wave action, causing the realities and prevalence of plastic pollution in marine environments to sometimes go unnoticed (1). These smaller particles, categorized as microplastics, can measure from only a few micrometers to 5 mm in length (4). To put the size of these plastic particles into perspective, they can be compared to the size of a grain of rice or a sesame seed, and in some cases, they can be invisible to the naked eye. While some microplastics can originate from larger plastic pieces that break down through various weathering processes, termed secondary microplastics, microplastics can also be purposefully produced at their size through manufacturing means for consumer products like cosmetics, which are known as primary microplastics (4). These microplastic contaminants, both primary and secondary, are now recognized on an international scale as one of the most powerful and concerning marine pollutants. A 2017 statement made by the European Union Commission established the significance of microplastics in our world, expressing that microplastics are of great concern due to the negative effects on aquatic life, aquatic environments, biodiversity, and possibly to human health (5). For instance, researchers have determined that microplastics are a detriment to the endocrine and lymphatic systems of marine animals upon frequent mistaken ingestion (6). Evidence also suggests that humans consume a plethora of microplastics through drinking tap water, taking in air, or in some cases, eating shellfish, although the exact threat these particles pose to human health currently remains unknown (6). Proposed consequences to human health include the ingestion of toxic substances and respiratory distress, among other potential complications (7). Ultimately, it is vital to evaluate all aspects of microplastics, yet various critical investigations and studies have yet to be completed.

This issue of microplastic pollution is a growing and relatively new topic of interest, posing a need for further

understanding of the presence and distribution of these microplastics in the environment (8). Increasing our level of comprehension is essential in developing appropriate policy and management tools to address this prominent issue. Further knowledge regarding microplastics will hopefully raise awareness to decrease plastic consumption and advocate for a more sustainable future.

Coinciding with the abundance of microplastics in the marine environment, these particles can turnover in beach environments and appear in the sand. To better understand the presence and distribution of microplastics along shorelines, we analyzed the sand of the beaches along the South Shore of Long Island, New York for microplastics. This location not only provides insight into the environmental conditions of the specific location, but it also serves as a basis for understanding other locations that are both located in close proximity to an urban area and are directly exposed to an ocean. By taking the nearby populous New York City (NYC) into account, we investigated how the distribution of microplastics varied depending on the sampling location in proximity to NYC. These inquires led to the establishment of our research question: how does the distribution of microplastics on the beaches along the South Shore of Long Island, New York vary depending on proximity to NYC, a populated urban area?

Based on the waste disposal problems that coincide with a densely populated area and a recent report that discovered the abundant presence of plastics and microplastics in the waterways surrounding NYC, we hypothesized that there would be a higher concentration of microplastic pollution in the sand from the beaches closer in proximity to NYC whereas the locations farthest from the city would have lower concentrations of the contaminants (9, 10). However, data and statistical analysis revealed a p-value of 0.75, leading us to the conclusion that there were no statistically significant differences between the numbers of microplastics collected from each sampling location.

RESULTS

In order to test our hypothesis and better understand a potential relationship between microplastic distribution and proximity to an urban area, sand was collected both above and below the wrack line from beaches along the South Shore of Long Island. These two locations of sampling were based on the wrack line in an effort to ensure consistency and uniformity among the different samples. The wrack line was also an ideal location for sampling because since it is a line of debris, it would be a probable location for any potential microplastics. After the collection of these sand samples, a floatation solution and microscope were used to gather data.

Type of Microplastic Polymer	Density (g/cm^3)
Expanded Polystyrene (EPS)	0.015-0.03
Polypropylene (PP)	0.89-0.91
Polyethylene (PE)	0.94-0.97
Polystyrene (PS)	1.04-1.08

Table 1. Common Microplastic Polymer Densities. The salt solution chosen (sodium chloride, which has a density of 1.2 g/cm^3) permits that microplastics of lower densities can be extracted via the filtration method (11).

Microplastics can be retrieved from different sediments with the help of various floatation solutions, such as sodium chloride (NaCl) or sodium iodide (NaI) (11). Only sodium chloride was utilized for this project, as it is both inexpensive and environmentally friendly in comparison to other options (11). After testing the sodium chloride negative control, we determined that there were no microplastics present in the solution. This guaranteed that the purified sodium chloride filtration solution was not a potential contaminant to the samples and their results. Sand has a density of approximately 2.65 g/cm^3, sodium chloride has a density of approximately 1.2 g/cm^3, and many microplastics have lower densities than both (**Table 1**) (11). Once the sand and sodium chloride were spun, any potential microplastics would float along the top of the solution with the sand settled at the bottom since substances of lesser densities rise to the top. We conducted ten trials per location, five above the wrack line, or the line of debris and organic material that remains on the

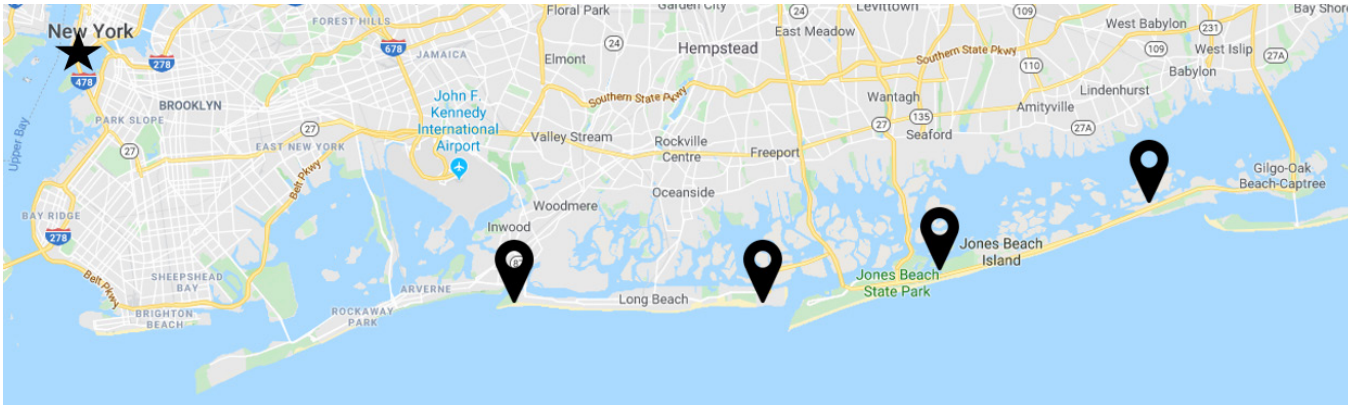

Figure 1. Sampling Locations in Relation to New York City. New York City is starred, and the beach locations are pinned, including Atlantic Beach, Point Lookout Beach, Jones Beach, and Overlook Beach, from west to east respectively.

	Atlantic	Point Lookout	Jones	Overlook
Above Wrack Line	1	3	2	2
Below Wrack Line	2	3	4	3
Total	3	6	6	5

Table 2. Number of Microplastics Retrieved from Each Beach Location. These numbers represent the total number of microplastics found in the given locations (n=10).

shore after high tide recedes, and five below the wrack line. Afterwards, the total number of microplastics retrieved from the four beach locations was organized and recorded (**Table 2**), with Atlantic Beach being the farthest west and closest in proximity to NYC and Overlook Beach being the farthest east and farthest in proximity to NYC (**Figure 1**). In total, both microplastic fibers (**Figure 2**) and microplastic fragments (**Figure 3**) were retrieved and accounted for, while there were no microplastic films found in any of the experimental groups. Overall, 6 of the total retrieved microplastics were fragments, while the remaining 14 collected microplastics were fibers. As evidenced by the data (**Table 2**), there does not seem to be a substantial difference in the total number of microplastics extracted from each location. However, the numbers do suggest that more microplastics were extracted from the sand samples below the wrack line, which is indicative of the idea that these contaminant particles wash up on shore via the ocean.

A Chi-square test was used to analyze the significance of these numerical results, as this test is commonly conducted to test for the difference in the distribution of categorical variables between various groups. In this case, the total number of microplastics from each location were compared using this test. The test resulted in an overriding p-value of 0.75, and since the p-value was greater than the significance level of 0.05, the differences in the number of microplastics across each sampling location were not statistically significant.

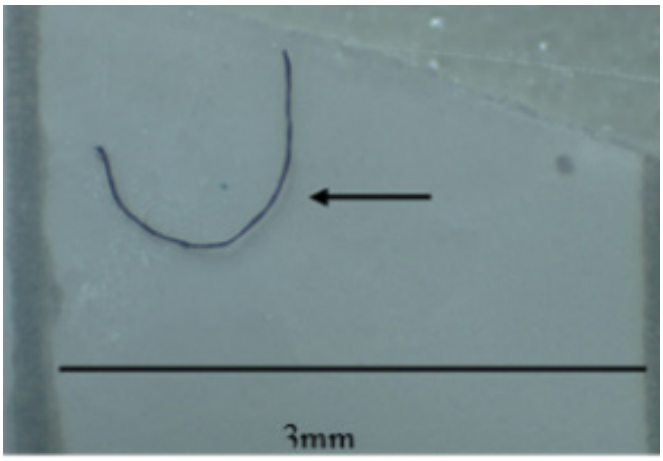

Figure 2. Blue Microplastic Fiber. This microplastic fiber was retrieved from above the wrack line at Atlantic Beach.

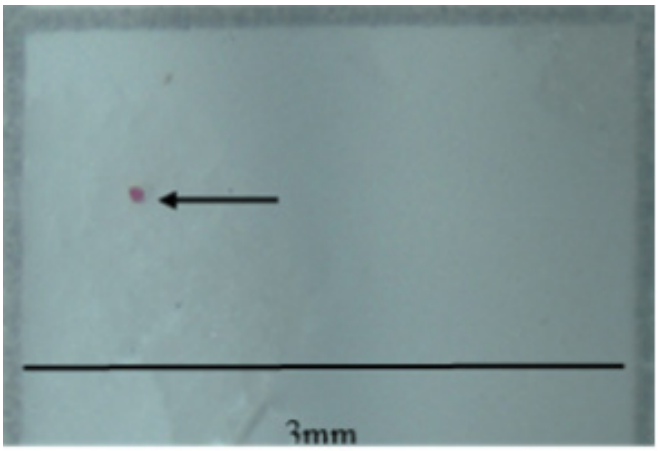

Figure 3. Pink Microplastic Fragment. This microplastic fragment was retrieved from below the wrack line at Jones Beach.

DISCUSSION

Although different numbers of microplastics were found at each location, these differences were not statistically significant. Overall, the calculated p-value could be due to the low number of collected microplastics, as there was not an abundance of data due to laboratory and time constraints. These results led to the conclusion that the beaches sampled do not show a statistically significant relationship between microplastic pollution numbers and proximity to New York City. With this conclusion, the amount of microplastics found on any given beach on the South Shore of Long Island, NY may not be influenced by the beach's location or proximity to New York City. However, a larger sample size could further validate this conclusion.

The statistical results of this study could be deemed surprising compared to existing work, such as the comprehensive study published by Foderaro on the proliferation of plastic in the waterways around New York City (10). Despite the study's findings that the waters surrounding New York City contain an estimated 165 million plastic particles at any given time, the beaches closer to this polluted water did not seem to contain more microplastics compared to the beaches farther east (10).

Additionally, based on a study that investigated various Belgian marine sediments for microplastics, lower numbers of microplastics were retrieved than expected in our research study. Claessens *et al*. extracted 92.8±37.2 microplastics of all forms per 1000 g of dry weight sand collected from beaches along the Belgian coast (12). This can be broken down to an average of approximately 4.64 microplastics per every 50 g of dry weight sand. Compared to our results, which involved 50 g of dry weight sand per trial, we extracted fewer microplastics. While some trials were unsuccessful in finding any microplastics, upwards of three microplastics were found in other trials of 50 g sand increments. Holistically speaking, we did not extract nearly as many microplastics as the aforementioned researchers did. This could be explained by various limitations and sources of error or be evidence that

microplastics are found in lesser quantities at the locations studied.

Though a smaller absolute number of microplastics were recovered, our data collection did reveal that microplastics were, in fact, present in some capacity in the sand from each sampling location along the South Shore of Long Island. These findings support other studies which have previously discovered microplastics in sand and other sediment samples (12). However, this emphasizes a larger problem: the widespread pollution of microplastics. Our study established that the South Shore of Long Island, New York is yet another location that has been marked by the presence of microplastic contaminants, which have the potential to harm local biodiversity and surrounding locations. The need for a solution to this environmental problem and emerging concern is of utmost importance. There should be further efforts and measures taken to limit the amount of plastic pollution to counteract this issue. Now knowing that microplastics are present at the South Shore, management tools and different policies can be enacted specifically in the area, which could contribute to stopping the problem on a larger scale.

It is important to account for the limitations of this research and methodology, as they may have impacted the results of the study. Since this methodology relied on a light microscope and the human eye to observe and quantify any microplastics, there could have been errors in counting the number of microplastics observed. While this is a commonly used method, it is possible that microplastics may have been overlooked. It has been found that while many microplastics are colorful, the ones that are transparent or white are not as easily picked up by the researcher when using a microscope (13). Additionally, Song *et al.* reported that microplastics less than 1 mm in size are hard to distinguish from non-plastic particles (13). As a result, the microplastic count could have been underestimated due to technical limitations. This could serve as the reasoning behind the relatively low number of extracted microplastics in this study, especially when making comparisons and considering other published research.

Sample size is another factor that could have limited the results of this research. Increasing the sample size, or the amount of sand and the number of trials conducted per location, would increase the validity of both the results and resulting p-value. We hope to continue conducting trials in attempts to strengthen the results and findings of this research.

Additionally, sand samples were collected on one day during the month of October due to the timeframe of the research study. There is a possibility that the time of year or season influence the amount of microplastics found along the shoreline. In order to mitigate this potential outside factor, we require studies that span one year during which sand samples from each location are collected and examined for microplastics at multiple, seasonal time points. Other microplastic studies similarly conducted research based on the collection of water samples or sediment samples from one given period and did not account for this potential limitation, however, this variable could be considered for future research studies (12).

Further research should be conducted to determine if other urban areas influence the amount of microplastics present in the sand of nearby beaches. As an example, studies could be conducted along the coastline of the Pacific in relation to Los Angeles, California to determine if the amount of microplastics found in the sand samples varies based on proximity to the city. Los Angeles has many similarities to New York City, as it is located along the coast of a major body of water and is densely populated. Conclusions drawn from an experiment of this caliber, in addition to our research that was done in relation to New York City, could potentially lead to more considerable conclusions regarding the effect of urban areas on the distribution of microplastic pollutants and further add to the conversation regarding microplastics and their distribution. Conducting this same research along the whole South Shore of Long Island, NY may also prove to be similarly beneficial and allow for the collection of more substantial data, as this study did not span the whole coastline. Overall, this knowledge would be vital for developing key management tools and effective policy to control and limit the amount of microplastics in the environment.

Due to the limitations regarding the methodology and the possibility of underestimating the number of microplastics in a sample, there is a need for further research to develop a standardized and validated methodology for microplastic quantification. While microplastic extraction techniques exist and are commonly used by researchers, many are flawed and coexist with some extent of error (13). A standardized methodology for the extraction of microplastics in sediments would be ideal, as it would allow researchers to efficiently and reproducibly extract sample material as well as compare results among various studies with minimal error in this regard.

METHODS

Collection of Sand

The samples of sand for this experiment were collected all on the same day in between times of low and high tide. Each sampling location was approximately equidistant from each other, spanning a total area of about 25 miles along the South Shore of Long Island, New York. The four beaches sampled, in order from west to east, included Atlantic Beach, Point Lookout Beach, Jones Beach, and Overlook Beach, which are all popular beaches on Long Island (**Figure 1**). Using a stainless-steel shovel, the top 5 cm of sand was collected from a 50 cm x 50 cm quadrant in two places at each beach: 1.5 meters below the wrack line and 1.5 meters above the wrack line. The collected samples were labeled accordingly and transported in separate containers to the school laboratory where they were left to dry for 24 hours at room temperature before further experimentation occurred.

Extraction Preparation

A 1 L saturated solution of NaCl was made from 358.9 g of NaCl in distilled water (14). Using sterile glassware to reduce the chance of contamination, the NaCl and water were added to a beaker containing a magnetic stir bar, and the mixture was stirred at 600 rpm for approximately 6 hours, allowing the salt to dissolve. The concentrated salt solution was then purified by filtering it through a 0.45-µm membrane filter into a new sterile flask using a vacuum pump. A vacuum pump was used to quickly and efficiently pulled the solution through the filter. This filter had a very small pore size, which allowed only the sodium chloride to pass through, thereby capturing any impurities. Purifying this sodium chloride was significant, as it reduced the risk of contaminating the samples or introducing any outside particles, which would otherwise impact the results gathered.

Extraction

For the microplastic extraction process, 50 g of dried sand from a given sample was mixed with 200 mL of the concentrated NaCl in a sterile 500 mL flask. The mixture was stirred at 600 rpm for approximately 5 minutes. The stir plate allowed the solution and the sand sample to rigorously combine before leaving them to settle.

After the spinning took place, the samples were left in covered flasks at room temperature for 24 hours. To isolate microplastics, the top 50 mL of the spun mixture was aspirated, or drawn, from the flask using a glass pipette. For each sample and trial, this supernatant, or top layer, which contained any potential microplastics, was filtered through sterile gridded 0.45-µm pore size membrane filter paper into a glass flask using a vacuum pump. Any existing microplastics were left on the filter paper while the remaining solution was contained in the flask. This process was repeated five times for each of the eight samples, as well as with 200 mL of the sodium chloride, which served as the negative control to confirm that the NaCl solution contained no microplastics or other particles that would influence our results.

Quantification

Each 0.45-µm pore size membrane filter paper was stored in a labeled sterile petri dish for 24 hours until placed on a slide to be viewed under a light microscope. A 24-hour waiting period before viewing was essential, as the filters had to be completely dry. Wet filters would have reflected the light of the microscope and limited the ability to view any microplastics (15). The light microscope was set to a 40x magnification, as this setting allowed for the quantification of microplastics measuring between 0.3 and 5 mm (14). Since microplastics measure 5 mm or smaller, this microscope setting enabled the viewing of almost all microplastics except for the smallest of particles. The filter paper utilized was gridded with boxes that had measured lengths of 3 mm to ensure that a suspected microplastic met the requirement of being less than 5 mm. These microplastics were identified and quantified based on published reference pictures and other characteristics, such as firmness and color (16). Since plastics are firm, a potential microplastic can be squeezed with fine tip forceps. Compared to other materials that may be confused with plastics, plastic maintains its shape once squeezed by the forceps. Additionally, plastics are often colorful and can be in the shape or form of fibers, films, or fragments. While microplastic fibers look like thin colorful threads, fragments appear as pieces of plastic, and films are thin pieces of plastic, similar to plastic food wrappers. These guidelines and characterizations were used to carefully draw conclusions regarding the presence of microplastics within a sample with as much accuracy as possible. Pictures were taken of each sample and the number of observed microplastics were recorded in a data table.

Statistical Analysis

Once quantified, the total number of microplastics collected from each of the four sampling locations was calculated. Using a Chi-square test with a significance level of 0.05 and an expected value of 5, the numbers of microplastics retrieved from the different samples were compared to determine if the differences in the number of microplastics from the varying locations were statistically significant or if the numbers of microplastics collected from each beach was independent of its location.

ACKNOWLEDGMENTS

I would like to thank mentors Mr. Richard Kurtz, Mrs. Janine Cupo, and Aiken Besley, as well as Harvard's Journal of Emerging of Investigators Editors for their guidance throughout this research process.

Received: June 9, 2020
Accepted: August 28, 2020
Published: September 21, 2020

REFERENCES

1. Parker, Laura. "The World's Plastic Pollution Crisis Explained." *National Geographic*, www.nationalgeographic.com/environment/habitats/plastic-pollution/. Accessed 20 Apr. 2020.
2. Joyce, Christopher. "U.S. Recycling Industry is Struggling to Figure Out a Future Without China." *National Public Radio*, https://www.npr.org/2019/08/20/750864036/u-s-recycling-industry-is-struggling-to-figure-out-a-future-without-china. Accessed 20 Apr. 2020.
3. Parker, Laura. "A Whopping 91% of Plastic isn't Recycled." *National Geographic*, https://www.nationalgeographic.com/news/2017/07/plastic-produced-recycling-waste-ocean-trash-debris-environment/#close. Accessed 20 Aug. 2020.
4. Andrady, Anthony. "Microplastics in the Marine Environment." *Marine Pollution Bulletin*, vol. 62, no. 8, 2011, pp. 1596-1605.

5. Laskar, Nirban, and Upendra Kumar. "Plastics and Microplastics: A Threat to Environment." *Environmental Technology & Innovation*, vol. 14, 2019, 100352.
6. Stack, Liam. "Wind Spreads Harmful Microplastics, Study Finds." *The New York Times*, 30 Apr. 2019, p. D4.
7. Campanale, Claudia, *et al*. "A Detailed Review Study on Potential Effects of Microplastics and Additives of Concern on Human Health." *International Journal of Environmental Research and Public Health*, vol. 17, no. 4, 2020, p. 1212
8. Gago, Jesus, *et al*. "Microplastics in Seawater: Recommendations from the Marine Strategy Framework Directive Implementation Process." *Frontiers in Marine Science*, vol. 3, no. 219, 2016.
9. National Geographic Society. "Urban Threats." *National Geographic*, www.nationalgeographic.com/environment/habitats/urban-threats/. Accessed 20 Apr. 2020.
10. Foderaro, Lisa W. "Study Shows the Buildup of Plastic in Waterways." *The New York Times*, 19 Feb. 2016, p. A28.
11. Rocha-Santos, Teresa, and Armando C. Duarte. "A Critical Overview of the Analytical Approaches to the Occurrence, the Fate and the Behavior of Microplastics in the Environment." *TrAC Trends in Analytical Chemistry*, vol. 65, 2015, pp. 47-53.
12. Claessens, Michiel, *et al*. "Occurrence and Distribution of Microplastics in Marine Sediments Along the Belgian Coast." *Marine Pollution Bulletin*, vol. 62, no. 10, 2011, pp. 2199-2204.
13. Song, Young Kyoung, *et al*. "A Comparison of Microscopic and Spectroscopic Identification Methods for Analysis of Microplastics in Environmental Samples." *Marine Pollution Bulletin*, vol. 93, no. 1-2, 2015, pp. 202-209.
14. Besley, Aiken, *et al*. "A Standardized Method for Sampling and Extraction Methods for Quantifying Microplastics in Beach Sand." *Marine Pollution Bulletin*, vol. 114, no. 1, 2017, pp. 77-83.
15. Marine & Environmental Research Institute. "Guide to Microplastic Identification." *Marine & Environmental Research Institute*, http://ise.usj.edu.mo/wp-content/uploads/2019/05/MERI_Guide-to-Microplastic-Identification_s.pdf. Accessed 20 Apr. 2020.
16. Sartain, Mandy, *et al*. "Microplastics Sampling and Processing Guidebook." *Mississippi State University,* 2018.

JOURNAL OF
EMERGING INVESTIGATORS

Article

A quantitative assessment of time, frequency, and time-frequency algorithms for automated seizure detection and monitoring

Pratik Vangal, Korin Riske
Sunset High School, Portland, Oregon

SUMMARY

Epilepsy is a chronic brain disorder impacting more than 65 million people worldwide (1% of the population). Its primary symptoms, seizures, can occur without warning and can be deadly. Each year, over 100,000 patients die from Sudden Unexpected Death in Epilepsy (SUDEP). A reliable seizure warning system can help patients stay safe. This work presents a comprehensive, comparative analysis of three different signal processing algorithms for automated seizure/ictal detection. The methods perform feature extraction and seizure detection on scalp electroencephalogram (EEG) signals. The first optimized mathematical model, Approximate Entropy, performed statistical time domain analysis using a new sliding window protocol. The second algorithm performed seizure-specific spectral energy binning using the Fast Fourier Transform in the frequency domain. The third method applied signal decomposition to extract ictal features by implementing a time-frequency Discrete Wavelet Transform method. Each epileptic seizure detection algorithm was successfully validated using >75 hours of recordings from the Boston Children's Hospital's CHB-MIT scalp EEG clinical database. Results indicated that the Discrete Wavelet Transform algorithm performed the best, achieving a seizure detection sensitivity of 92% and a specificity of 98%. The experimental results show that the proposed methods can be effective for accurate automated seizure detection and monitoring in clinical care.

INTRODUCTION

Over 65 million people live with various forms of epilepsy (1). Patients in low- and middle-income countries are at double the risk of being diagnosed with epilepsy (1). Over 30% of epilepsy patients do not respond to antiepileptic drugs (2). Seizures, the principal symptom of epilepsy, often occur unpredictably and can lead to convulsions throughout the entire body (2). Loss of consciousness due to an epileptic event may result in physical injuries and fatal falls based on the location where the seizure occurred (e.g., driving, swimming, etc.), this is known as Sudden Unexpected Death in Epilepsy (SUDEP) (2). Seizure alarm systems can help detect these emergency scenarios as they happen, alerting family members and care providers (3). A comparative analysis of the efficiency of seizure detection algorithms can help provide valuable insights for deployment in the next generation of epileptic patient aid devices.

An electroencephalogram (EEG) is a gold-standard test that tracks and records brain electrical patterns (4). An EEG headset contains several surface electrodes to track the brain's electrical activity. The electrodes are placed on the scalp as per the 10/20 international system (**Figure 1A**) (5). Any neuronal synaptic activity in the brain generates a subtle electrical impulse referred to as a postsynaptic potential (4). This small analog voltage fluctuation, measured at the electrodes, is amplified, digitized, and recorded as a continuous flow of voltages vs. time (time series data). An EEG study can show the origin of abnormal activity in the brain and is one of the main diagnostic tests for epilepsy. An EEG can also play a role in diagnosing other brain disorders, such as Alzheimer's disease and narcolepsy (6).

The Children's Hospital in Boston (CHB) and the Massachusetts Institute of Technology (MIT) provide a free-to-use online scalp EEG database (7). The dataset is from 23 pediatric epilepsy patients, each with several seizure recordings. The entire record consists of 686 data sets, with 198 datasets containing seizures, and over 1,000 hours of EEG recordings. The data was recorded at 256 samples per second (Hz) with a 16-bit resolution. A 23-electrode (or 23-channel) EEG, visualized using the EEGLAB tool (8), shows the clinical onset of a patient seizure (ictal) starting at 2162 seconds (**Figure 1B**), which is characterized by the large signal excursion artifacts caused by muscle reflexes in patient 3, from data set 4.

Over the past three decades, much research has been done using time, frequency, and time-frequency analysis methods for the detection of seizure activity in EEGs (9–11). However, a study that cohesively compares these methods using a common framework with validation against publicly available epileptic datasets is necessary. This work presents a thorough examination of three promising seizure detection methods: Approximate Entropy, Fast Fourier Transform, and the Discrete Wavelet Transform.

Complexity is an essential characteristic of nonlinear

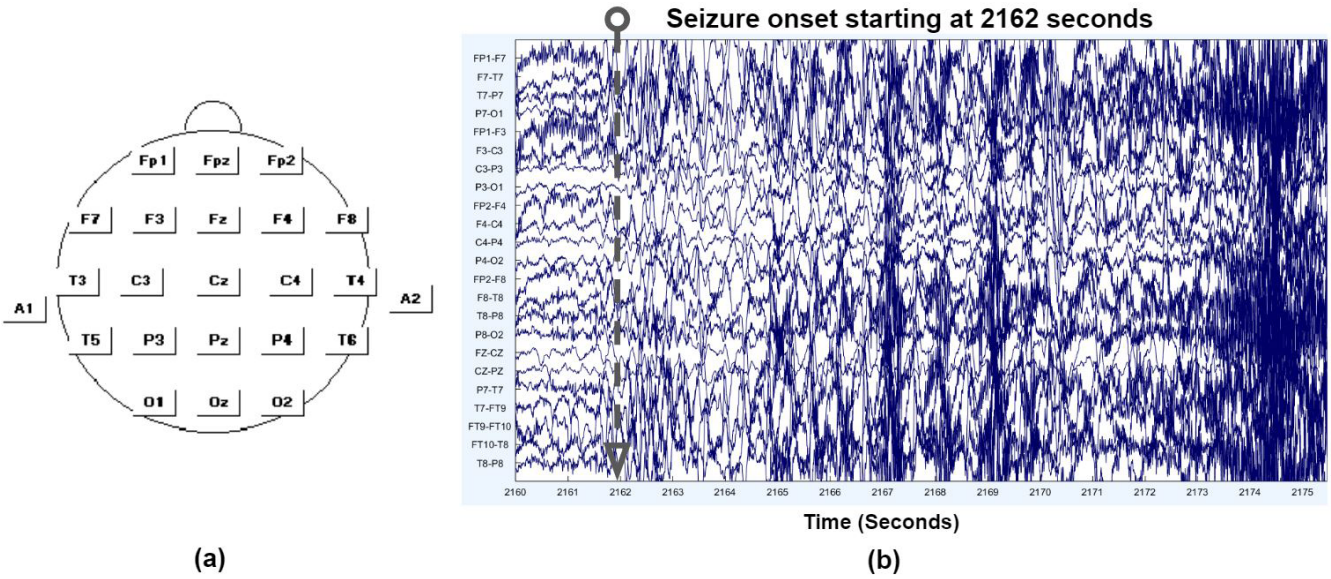

Figure 1. EEG electrode positioning order and EEGLAB examination of an ictal-event. (a) International 10/20 electrode placement system (5) **(b)** A 23-channel scalp EEG showing clinical onset (grey arrow) of patient seizure starting at 2162 seconds, which is characterized by muscle reflexes causing the large signal excursion artifacts (CHB-MIT patient 3, data set 4).

dynamic systems. Approximate entropy (ApEn) is a statistical time domain analysis technique used to quantify waveform regularity and the unpredictability of fluctuations in time series data (12). A time series containing many repetitive patterns has a relatively small approximate entropy, while a less predictable process has a higher ApEn value. The ApEn approach has the following advantages: (1) it requires relatively fewer data points (100 – 5000), and (2) it is robust against noisy data, common in EEG recordings.

The ApEn method has been used to analyze EEG signals of patients under different physiological and cognitive states (13). In this work, an improved ApEn algorithm is proposed to characterize the dynamical properties of the ictal transition in epileptic patients. Based on the observed variations in the ApEn during preictal, interictal and postictal states, the epileptic seizure is detected.

The Fast-Fourier Transform (FFT) converts a signal from the time domain into the frequency domain and has been used for epileptic seizure detection (11). Any time-dependent signal can be broken down into a collection of sinusoids (14). In this way, lengthy and noisy EEG recordings can be rationally plotted in a frequency power-spectrum using the MATLAB discrete *fft()* function (15). Frequency domain FFT analysis was performed on CHB patient data to identify hidden features, applicable for feature extraction.

Wavelets are oscillations with a mean value of zero and can provide adaptive resolution in both time and frequency domains for analysis of non-stationary signals (**Figure 2A**) (16). A coiflet, as an example, is a type of a wavelet with a unique shape that best represents EEG artifacts during a seizure (**Figure 2A**) (17). The wavelet transform has unique higher resolution capabilities in comparison to other restricted, individual time and frequency domain analysis techniques (**Figure 2B**).

The main advantage of using a discrete wavelet transform (DWT) method is that the resolution of time and frequency can be adapted to the frequency content of the examined patterns (18). The DWT filters signals using low-pass and high-pass filters to yield approximate and detailed sub-bands, respectively (**Figure 2C**). With each increasing level (1–7), the signal segment is further decomposed into a lower frequency range. As EEG data is noisy in nature, the DWT approach can help denoise the waveform and enunciate the key features at each level. The MATLAB *wavedec(x, n, wname)* function (19) returns the wavelet decomposition of the 1-D signal *x* at level *n* using the wavelet *wname* (*coif3* in this case).

The effort has the following key goals: develop mathematical models for ictal-event classification and automated seizure detection of scalp EEG data; ensure >80% detection accuracy and minimal false alarm occurrence; and quantitatively assess multiple seizure detection approaches that enable highest overall accuracy. The final ApEn, FFT, and Wavelet algorithms had accuracies of 90%, 92%, and 95% respectively.

RESULTS

A continuous EEG monitoring and automatic seizure detection algorithm framework was proposed and employed throughout this work (**Figure 3**). In step (*i*) the CHB-MIT Scalp EEG database (publicly available at PhysioNet (7)) was converted from a binary EDF format to a readable ASCII format in step (*ii*). The third step (*iii*) was to pre-process the raw EEG signals to separate noise from the signal of

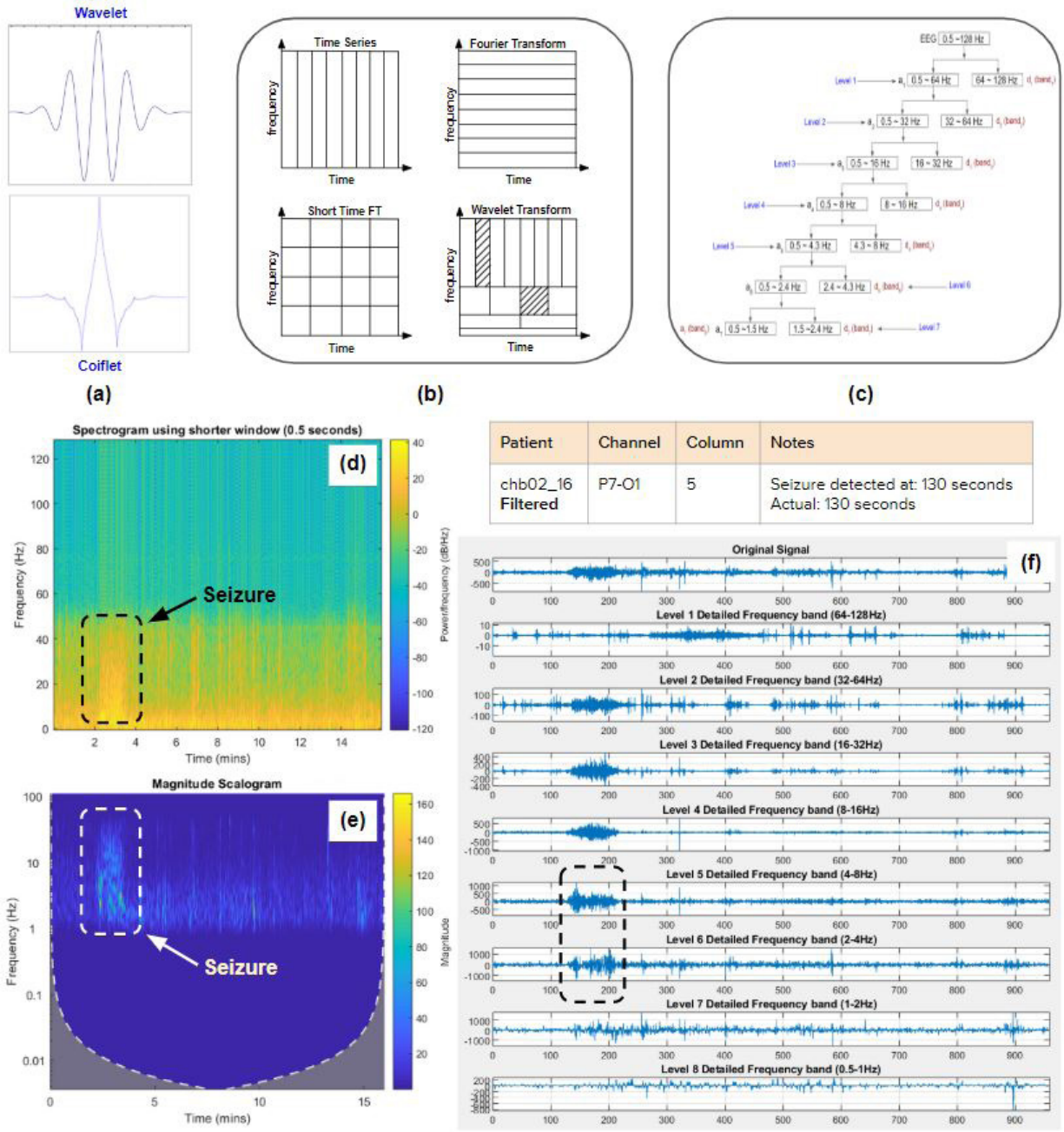

Figure 2. Time-frequency based wavelet analysis accurately identifies ictal events. (a) The coiflet wavelet used for DWT analysis **(b)** Time and frequency resolutions for various transforms **(c)** DWT Frequency band decomposition of an EEG signal **(d)** FFT-based spectrogram clearly reveals the seizure event starting at 130 seconds **(e)** CWT analysis proves to be an effective tool for seizure detection with coefficient values peaking at 130 seconds **(f)** Results from an eight-level DWT show that ictal events are most clearly represented and have the highest magnitude in the 2–8 Hz range at levels 5, 6.

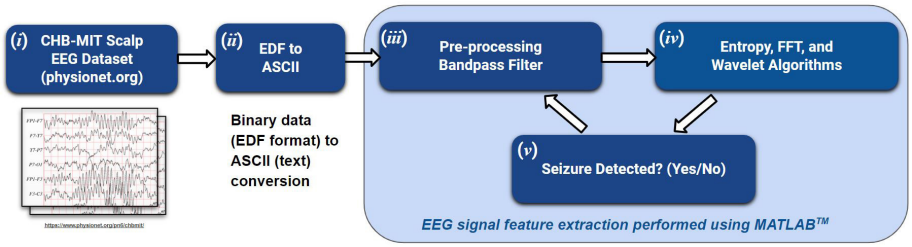

Figure 3. Proposed seizure detection algorithm flow using MATLAB™ numerical computing software.

interest. A digital bandpass filter with a frequency ranging from 0.35 to 45 Hz was used to alleviate the influence of low- and high-frequency noise. Feature extraction is performed on the filtered EEG data using multiple EEG classification methods (step *iv*) and the classifier results are analyzed with appropriate thresholds to reliably detect seizures in step (*v*).

To account for continuous EEG signal acquisition of time series data, steps (*iii*)-(*v*) are repeated in a loop. The entire analysis was coded and simulated using MATLAB (15).

Time Domain EEG Feature Extraction Algorithm

Multiple hours of raw and filtered versions of EEG time series data were first visually inspected using MATLAB to carefully identify the features critical to distinguish normal, interictal (between seizures), and ictal events in EEG signals from other types of brain activity. A single channel 24-minute CHB-MIT raw EEG signal trace for patient 24, data set 1 (**Figure 4A**). Clinically, the ictal event occurs between 480–505 seconds, as observed by a sudden spike in brain activity. Two key observations are made from studying the expanded and closer view of the EEG waveform during a seizure (**Figure 4B**): a substantial increase in signal amplitudes (exceeding 1 mV) due to abnormal discharges in a large number of neurons in the brain and the periodic and synchronous nature of the EEG, resembling a sinusoid. These two fundamental attributes are insightful and crucial for automated ictal event feature extraction. On the other hand, a closer EEG signal view during a non-ictal phase (**Figure 4C**) exhibits a complex signal with a much lower magnitude (typically in the tens of μV) with a high degree of randomness. These discernable characteristics in signal behavior separate ictal and non-ictal intervals (i.e. seizure and 'normal' electrical activity) and can be used to identify transitions between epileptic states.

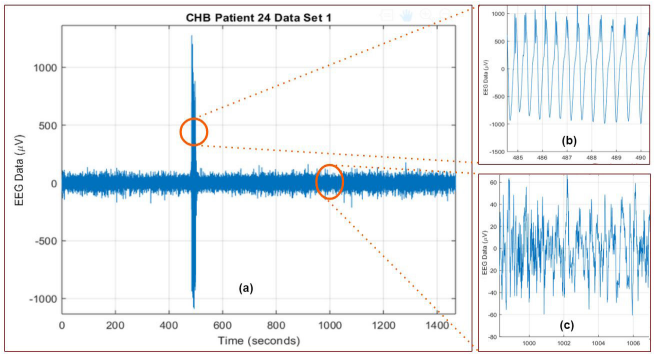

Figure 4. Analysis of CHB-MIT patient 24 reveals the synchronous nature of epileptic seizures. (a) A 24-minute raw EEG signal trace with an ictal-event (seizure) between 480–505 seconds (patient 24 data set 1) **(b)** Expanded EEG (~1mV) and a periodic signal **(c)** Expanded EEG waveform during non-seizure. Note lower signal amplitude (μV) and high randomness.

ApEn algorithm

Given *N* points of a time series data and the similarity criterion *r*, the ApEn is approximately equal to the average natural logarithm of the conditional probability that vectors similar for *m* points remain comparable at the next point. The similarity is validated using a vector distance calculation (12-13) as shown in Step 1 (**Figure 5A**), with the conditional probabilities for each window computed in Step 2. The similarity of two vectors is judged in the final step as a subtraction operation, resulting in a final ApEn value. Intuitively, for a predictable signal (such as a seizure), the conditional probabilities across two adjacent vectors would be similar, producing a small value for ApEn when subtracted. However, a noisy random EEG signal would have diverse conditional probabilities, resulting in high entropy.

The ApEn algorithm was implemented in MATLAB using the CHB-MIT scalp EEG dataset and the framework previously outlined (**Figure 3**). The raw EEG signals are pre-processed to remove high frequency noise. A Butterworth digital bandpass filter of order 5 with a cutoff frequency from 0.35 to 45 Hz (20) was applied. Within this range of frequencies, the complete information about the signals of interest is still retained. Early ApEn analysis showed that obtaining ApEn parameters - vector dimension (*m*), the filtering threshold (*r*) and the ideal window size (*N*) - were critical for reliable feature extraction of seizures. A multi-variable sweep was performed using MATLAB to arrive at the optimal values used in this study (**Figure 5B**).

The frequency response of the bandpass filter displayed

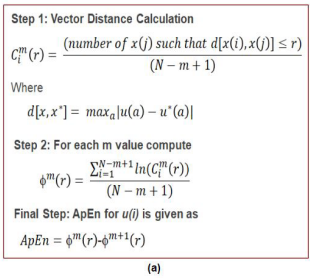

ApEn Parameter	Meaning	Values used (in MATLAB)
m	Vector dimension	*m=2 and m=3*
r	Filtering threshold	1 μV
N	Data points per EEG window	512 (2 seconds)

(b)

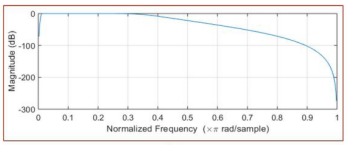

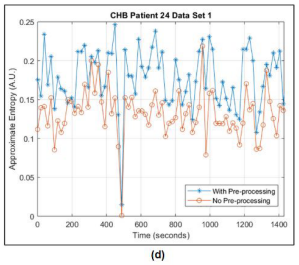

Figure 5. The epileptic EEG signal is preprocessed via a fifth-order Butterworth bandpass filter prior to ApEn analysis. (a) ApEn algorithm (12) with three key steps resulting in a quantified value of waveform regularity. **(b)** Optimal values used for m, r, and N parameters in the ApEn calculation. **(c)** Frequency response of the fifth-order digital Bandpass filter. **(d)** The graph shows the seizure onset at 480 seconds as marked by a sharp drop in ApEn value towards zero. Signal preprocessing improves signal-to-noise ratio by 32%.

expected patterns, ultimately removing high frequency EEG signal noise (**Figure 5C**). The resulting MATLAB plot after ApEn application precisely detects the seizure onset of patient 24, data set 1 at 480 seconds (**Figure 5D**), marked by a conspicuous drop in the ApEn value. The graph also shows the signal preprocessing benefit with an improvement of 32% in ApEn due to enrichment in the average signal-to-noise ratio (SNR).

Implementation of the Sliding Window Protocol on EEG signals

The incoming EEG time series data is often segmented into smaller processing windows, typically in smaller non-overlapping 1–2 second slices (**Figure 6A**). Real-time data computation requires the ApEn calculation in the first window to be completed by the time the next window frame arrives. A sliding window approach was implemented that overlaps the EEG time series slices and ApEn computation (**Figure 6A**), with a 50% (0.5 second) overlap. ApEn results with and without overlapping windows were evaluated for CHB patient 15, data set 6 (**Figure 6B**). The increased number of intermediate ApEn points helps emphasize the ictal features better, allowing for improved seizure detection.

The efficacy of the enhanced ApEn algorithm with the sliding-window approach in MATLAB for CHB patients was evaluated for two patients (**Figures 6C-D**). In each case, the raw EEG data is displayed with the corresponding ApEn results. The proposed approach articulately identified the ictal event that is indicated by a pronounced drop in the computed ApEn values, falling toward zero. The proposed method, even in the presence of noisy EEG input streams, can efficiently identify seizures automatically.

Frequency Domain EEG Feature Extraction Algorithm

A 7 second raw EEG signal trace for patient 24, data set 1, highlighting the periodic seizure signature, is shown (**Figure 7A**). A 128-point FFT was performed to generate the corresponding frequency spectrum (**Figure 7B**). The frequency spectrum shows the dominant peaks in the 2–6 Hz range. Repeating the study on other patient data confirmed that the principal peaks occur in the 2–6 Hz spectrum during an ictal event. This primary observation is used for seizure-specific feature extraction. The spectrum binning to identify seizures was implemented in the core section of the MATLAB code and followed the algorithmic flow previously outlined (**Figure 3**). The raw EEG data in time domain and the dominant spectral components obtained from binning in the frequency domain were collated from FFT analysis on 0.5 second EEG slices for two patients (**Figures 7C-D**). In each case, the spectral peaks during seizures are conspicuous, marked by a clear presence of an assertive slow wave "ictal" component in the 2–6 Hz range.

Time-Frequency Seizure Classification Based on a Wavelet Decomposition Method

Epileptic EEG signal analysis using ApEn and FFT methods revealed that seizures can be accurately identified

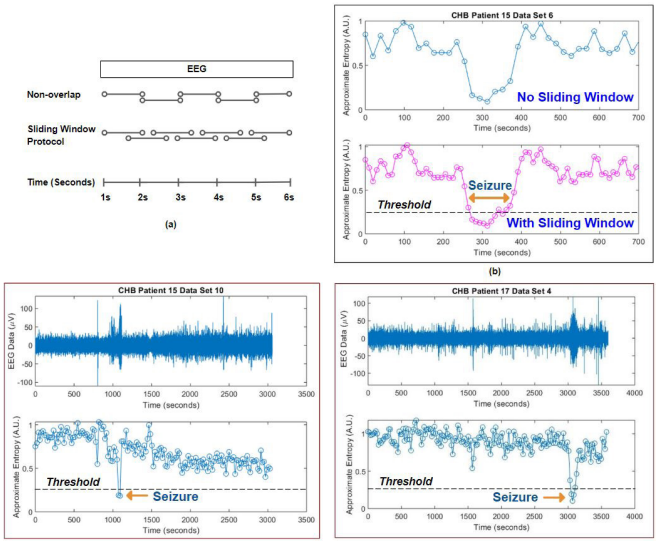

Figure 6. Sliding window protocol benefit and ApEn analysis of two CHB-MIT patients. (a) Sliding window concept by overlapping time series EEG data. **(b)** The benefit of the sliding window approach with a 0.5 second overlap can be observed in the lower subplot. The increased number of points help bring out additional features within the data **(c, d)** show drops in the ApEn values during a seizure onset between 272-390 seconds. These features are used to classify the ictal event as a seizure, if the ApEn values drops below a specified threshold.

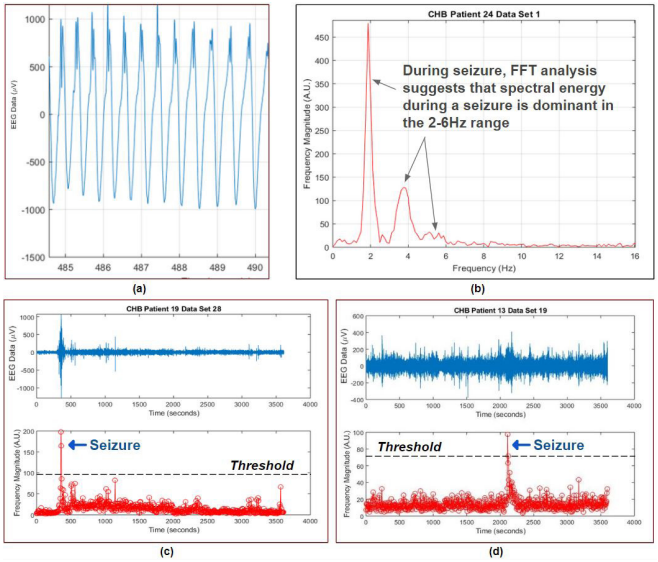

Figure 7. Frequency decomposition of seizure data reveals dominant spectral energy components from FFT analysis of two CHB-MIT patients. (a) Expanded EEG waveform during a seizure, note large signal amplitude (mV) and its periodic nature. **(b)** Frequency spectrum during a seizure (2–6Hz) obtained using MATLAB. **(c, d)** show articulate increases in spectral energy at 300 seconds (patient 19) and 2100 seconds (patient 13) during epileptic events. The spectral peaks are used to classify the ictal event as a seizure, if the spectral magnitude crosses a specified threshold.

in the time domain or in the frequency domain, with both approaches providing good resolution in their respective domains. However, EEG signals are non-stationary in nature, and are best represented using wavelet-based time-frequency interpretations (9).

Wavelet analysis was performed on patient 2 dataset 16 (**Figures 2D**–**F**). A short (0.5 second) window spectrogram derived from an FFT calculation clearly reveals the seizure between 2–4 minutes (**Figure 2D**). A Continuous Wavelet Transform (CWT, MATLAB *cwt()* function), as the name suggests, allows for simultaneous analysis of EEG waveforms rather than discretizing the data into frequency bands as with the DWT method (18). The coefficients from CWT analysis on patient 2 were plotted in a scalogram (**Figure 2E**). The time-frequency scalogram clearly shows the seizure starting at 130 seconds. Frequency decomposition using DWT clearly identifies the seizure in the low-frequency (2–8 Hz) range at levels 5 and 6 (**Figure 2F**).

The results from validating time, frequency, and time-frequency domain analysis for scalp EEG ictal feature extraction against 50 datasets from the CHB-MIT database (7) is next presented. An improved ApEn statistical approach provided a seizure detection accuracy of 90%. FFT and spectral energy analysis enabled an accuracy of 92%. A combined time-frequency based Discrete Wavelet Transform (DWT) utilizing "coiflets" resulted in a 95% accurate algorithm (**Table 1**). Algorithmic performance results in terms of sensitivity and specificity for the three methods were also computed. The sensitivity ranges from 84–92% and the specificity ranges from 96–98%. Every automated ictal classification result was authenticated against actual seizure labels specified in the CHB-MIT dataset, as marked by a medical professional.

Table 1. Seizure detection accuracy from validating all three signal processing techniques against the CHB-MIT scalp EEG dataset.

Time Domain Entropy Analysis		**Target**	
		Positive	Negative
Model	Positive	42	2
	Negative	8	48
Accuracy = 90%		Sensitivity	Specificity
		84%	96%
Frequency Domain FFT Method		**Target**	
		Positive	Negative
Model	Positive	43	1
	Negative	7	49
Accuracy = 92%		Sensitivity	Specificity
		86%	98%
Time-Frequency Wavelet Analysis		**Target**	
		Positive	Negative
Model	Positive	46	1
	Negative	4	49
Accuracy = 95%		Sensitivity	Specificity
		92%	98%

Sensitivity and specificity values are provided in each case. The DWT wavelet analysis approach provides the highest overall seizure detection success rate of 95%.

DISCUSSION

Epilepsy has a great impact on the everyday life of patients. Several wearable devices have been proposed in the literature to detect seizures via patient monitoring (21-22). Such seizure alarms and aids for epilepsy patients would serve three main purposes: 1) Seizure detection, 2) seizure alarming and 3) recording of 30–60 seconds of pre-ictal and ictal EEG signals for precise diagnosis. A smart headband for epileptic seizure detection is presented in (23), but is expensive. There is a need to develop and implement real-time, high-speed, and accurate algorithms on various low-cost hardware devices for seizure detection and pervasive global use. Specifically, these medical devices demand precise seizure classification algorithms with reduced computational overheads.

In this paper, three seizure detection techniques are evaluated and classified as time, frequency, and wavelet (time–frequency) techniques. The time domain method analyzes signals based only on the time and magnitude components of time series data, and there is no visibility into the frequency components of the signal. The frequency domain approach provides a more articulate frequency spectrum of the signal. The advantage of the signal transformation from one domain to another is that it provides valuable insights and points out the important properties of the signals, which cannot be seen by visual inspection of the original signal alone, thus helping distinguish different states in seizure EEG signals. A wavelet transform as a time–frequency analyzing tool provides improved time and frequency localization capability. It uses long time windows for low-frequency components and short time intervals for high-frequency components of the signals.

Among the three methods evaluated, the DWT classification approach on epileptic EEG signals shows excellent promise for seizure classification and monitoring, with the analysis successfully detecting a seizure on 46 of 50 epileptic datasets, with an improved accuracy of 95%. The elastic principle of the wavelet enables short time signal components to be better detected and more precisely localized by the DWT approach when compared to results obtained by FFT and time domain methods.

In each algorithm, appropriate thresholding of the extracted features is critical for robust and reliable automated seizure detection. A combination of hard and soft threshold criteria was employed. When applying the ApEn algorithm on EEG signals, the resulting entropy values rapidly dropped towards zero during ictal events. Experimenting

with the limits showed that a hard ApEn threshold of 0.25 was optimal. In the case of FFT and DWT algorithms, a variable thresholding approach was applied. A seizure was identified as "true" only when current feature extracted vector values (e.g., integrated spectral energy in the FFT 2–6 Hz band or the DWT coefficients in levels 5/6) exceeded five times the magnitude of a rolling average over time. The seizure detection algorithms provide high values for sensitivity and specificity for EEG data sets in the CHB-MIT database without any additional assumptions of seizure patterns. The algorithms can be a valuable tool for fast and effective monitoring of long-term scalp EEG recordings. As future work, implementing patient-specific screening using adaptive thresholds may allow for improved seizure detection accuracy.

METHODS

The programming and analysis were performed using MATLAB numerical computing software. The work was carried out in phases — starting with time domain, followed by frequency domain, and finally a combined time-frequency analysis. The first algorithm, approximate entropy, was developed following observations of EEG signal patterns during seizures. Next, the work transitioned from the time domain into the frequency domain using FFT functions. Spectral energy binning using the short-term Fourier transform revealed that the seizure signals contained slow waves with large magnitudes. The FFT results led to the development of the second seizure classifier. The final method implemented a "best-of-both-worlds" strategy by analyzing signals in the time-frequency domain. The DWT approach using coiflets enables optimal time-frequency resolution across all frequency ranges by consistently extracting key seizure features in EEG data. The models were optimized using signal pre-processing and a sliding window protocol, increasing the accuracy of each algorithm. In the MATLAB code, a 50% (0.5 second) overlap is used in the computation loop. After all model parameters were finalized, they were tested using >75 hours of data from the CHB-MIT database (**Table 1**). To further validate the algorithms' effectiveness, a robustness check was performed using alternate *non-seizure* EEG databases (sleep database (24), motor movement/imagery database (25)). All algorithms passed the robustness trials successfully, with no additional false alarms reported.

ACKNOWLEDGEMENTS

The author sincerely thanks Dr. Nick Van Helleputte at IMEC, Belgium and Professor Tinoosh Mohsenin at the University of Maryland, Baltimore County for technical discussions and for reviewing the seizure detection results. The author also recognizes the engineers at MathWorks for sample code from MATLAB's signal processing toolbox that helped analyze uniformly sampled EEG signals.

Received: May 3, 2020
Accepted: September 16, 2020
Published: September 28, 2020

REFERENCES

1. "Epilepsy." *World Health Organization*, World Health Organization, 20 June 2019, www.who.int/news-room/fact-sheets/detail/epilepsy.
2. Laxer, Kenneth D., *et al*. "The Consequences of Refractory Epilepsy and Its Treatment." *Epilepsy and Behavior*, vol. 37, 2014, pp. 59-70., doi: 10.1016/j.yebeh.2014.05.031.
3. MD. "The Role of Seizure Alerts." Edited by Patty Obsorne Shafer, Epilepsy, Epilepsy Foundation, 12 Nov. 2019, www.epilepsy.com/learn/early-death-and-sudep/sudep/role-seizure-alerts.
4. Evans, Laura. "EEG Gold Standard in Epilepsy Diagnostics." Open Access Government, 6 Aug. 2019, www.openaccessgovernment.org/profile-eeg-gold-standard-epilepsy-diagnostics/17529/.
5. Smith, E J. "Introduction to EEG." EBME, 14 Sept. 2013, www.ebme.co.uk/articles/clinical-engineering/introduction-to-eeg.
6. "Electroencephalogram (EEG)." *Johns Hopkins Medicine*, www.hopkinsmedicine.org/health/treatment-tests-and-therapies/electroencephalogram-eeg.
7. Goldberger, Ary L., *et al*. "PhysioBank, PhysioToolkit, and PhysioNet: Components of a New Research Resource for Complex Physiologic Signals." *Circulation*, vol. 101, no. 23, 2000, e215-e220., doi: 10.1161/01.cir.101.23.e215.
8. "EEGLAB." Interactive Matlab Toolbox at https://sccn.ucsd.edu/eeglab/index.php.
9. Niko Busch, "Time-Frequency Analysis of EEG Waveforms", online tutorial @ Berlin School of Mind and Brain, Charite University.
10. Zhou, Yi, *et al*. "Application of Approximate Entropy on Dynamic Characteristics of Epileptic Absence Seizure." *Neural Regeneration Research*, vol. 7, no. 8, 2012, pp. 572-577., doi:10.3969/j.issn.1673-5374.2012.08.002.
11. Meenakshi, *et al*. "Frequency Analysis of Healthy & Epileptic Seizure in EEG Using Fast Fourier Transform". *International Journal of Engineering Research and General Science*, vol. 2, no. 4, 2014, pp. 683-691.
12. Pincus, Steven M., "Approximate entropy as a measure of system complexity." *Proceedings of the National Academy of Sciences of the United States of America*, vol. 88, no. 6, 1991, pp. 2297-2301., doi: 10.1073/pnas.88.6.2297.
13. Peng, Li, *et al*. "Detection of epileptic seizure based on entropy analysis of short-term EEG." *PLoS One*, vol. 13, no. 3, 2018, e0193691., doi: 10.1371/journal.pone.0193691.
14. Lehar, Steven. "An Intuitive Explanation of Fourier Theory." *Semantic Scholar*, 10 Mar. 2010, pdfs.semanticscholar.org/3d67/a901be76a2258db924799bd88e258032bb6b.pdf.

15. "MATLAB™." *MathWorks*, www.mathworks.com/products/matlab.html.
16. Chen, Duo, *et al*. "A High-Performance Seizure Detection Algorithm Based on Discrete Wavelet Transform (DWT) and EEG." *PLoS One*, vol. 12, no. 3, 2017, e0173138., doi: 10.1371/journal.pone.0173138.
17. Wei, Dong. *COIFLET-TYPE WAVELETS: THEORY, DESIGN, AND APPLICATIONS*. The University of Texas, Aug. 1998, users.ece.utexas.edu/~bevans/students/phd/dong_wei/phd.pdf.
18. "Continuous and Discrete Wavelet Transforms." MathWorks, www.mathworks.com/help/wavelet/gs/continuous-and-discrete-wavelet-transforms.html.
19. "Wavedec: 1-D Wavelet Decomposition." *MathWorks*, www.mathworks.com/help/wavelet/ref/wavedec.html.
20. Sarma, Parthana, *et al*. "Pre-Processing and Feature Extraction Techniques for EEG-BCI Applications- A Review of Recent Research." *ADBU-Journal of Engineering Technology*, vol. 5, 2016, pp. 0051604.
21. Conradsen, *et al*. "Evaluation of novel algorithm embedded in a wearable sEMG device for seizure detection," *2012 Annual International Conference of the IEEE Engineering in Medicine and Biology Society*, San Diego, CA, 2012, pp. 2048-2051, doi: 10.1109/EMBC.2012.6346361.
22. Beniczky, Sándor, *et al*. "Automated Real-Time Detection of Tonic-Clonic Seizures Using a Wearable EMG Device." *Neurology*, vol. 90, no. 5, 5 Jan. 2018, doi:10.1212/wnl.0000000000004893.
23. Lin, Shih-Kai, *et al*. "An Ultra-Low Power Smart Headband for Real-Time Epileptic Seizure Detection." *IEEE Journal of Translational Engineering in Health and Medicine*, vol. 6, 17 Aug. 2018, doi:10.1109/jtehm.2018.2861882.
24. Kemp, B, *et al*. "Analysis of a sleep-dependent neuronal feedback loop: the slow-wave microcontinuity of the EEG." *Institute of Electrical and Electronics Engineers Transactions on Biomedical Engineering*, vol. 47, no. 9, 2000, pp. 1185-1194., doi: 10.1109/10.867928.
25. Schalk, Gerwin, *et al*. "BCI2000: A General-Purpose Brain-Computer Interface (BCI) System." *Institute of Electrical and Electronics Engineers Transactions on Biomedical Engineering*, vol. 51, no. 6, 2004, pp. 1034-1043. doi: 10.1109/TBME.2004.827072.

JOURNAL OF
EMERGING INVESTIGATORS

Article

Testing different polymers and boron nitride nanotube properties in fabrication of ion-selective membranes

Joshua Yi[1], Jerry W. Shan[2]
[1]East Brunswick High School, East Brunswick, New Jersey
[2]Fluid Hydrodynamics Laboratory, Rutgers University, New Brunswick, New Jersey

SUMMARY

One largely untapped source of clean energy is the use of osmotic gradients where freshwater and saltwater are mixed, for example at estuaries. To harness such energy, charge-selective membranes are needed to separate the anions and cations in saltwater, establishing an electric potential like a battery. The objective of this study was twofold: to investigate the creation of the polymer matrix and test the properties of boron nitride nanotubes, as both are essential in the creation of an ion-selective membrane. The proposed polymer layer has many attractive properties: controllable thickness allowing nanotubes (typically 5-10 microns long) to pass through, being rapidly curable with a UV lamp, easy mounting on other substrates, resistance to O_2 and SF_6 plasma gas etching, and structural strength to prevent tears. The hypotheses for this study are that the Soltech 704 (SU704) will prove to be the best polymer in terms of both etching and curing results, in addition, the relationship between the magnetic dipole moment and the length of the nanotubes is predicted to be linear. The Soltech 704 is trifunctional, compared to the other difunctional polymers tested, which is why it is predicted to have the highest strength. The dipole moment was hypothesized to be linear with nanotube length, since a longer nanotube allows for more iron oxide particles to attach to it. Out of three polymer samples tested in this study, the mixture known as Soltech 704 showed the best resistance to etching, as well as the highest UV cure rate. These two traits are desirable since they lead to a sturdier membrane and one that is created more quickly. To allow such nanotubes to be aligned, we attached magnetic iron oxide particles and then applied a magnetic field. We then recorded the magnetic dipole moments of nanotubes and compared it to the length of the nanotube. The relationship between dipole moment and length can thus be discovered. Such results can be used to optimize the alignment procedure for the nanotubes, as well as the procedure for curing the polymer.

INTRODUCTION

Clean energy has been one of the most pressing issues in recent years. Most of the current energy generating methods rely on non-renewable resources, such as coal, oil, uranium, and natural gas. This is neither sustainable nor environmentally friendly, as many pollutants from combustion are released into the atmosphere (1). Although some other methods are currently being developed to generate energy such as solar or wind power, these sources are expensive, intermittent, and have limited efficiency in their power generation.

An alternative method to fix this issue is to harness the osmotic gradient between freshwater and saltwater in estuaries or the mouths of rivers. This is a better alternative energy source compared to existing sources, as it is cheaper to build than solar or wind farms, more available as facilities can be built at any coastal location with brackish water, and it provides constant non-intermittent power (1). Globally, it is estimated that over one terawatt of this unused energy can be successfully harnessed, roughly equivalent to the power of 1,000 nuclear reactors (1). Although there are many methods to harness such an energy, one of the most efficient methods is known as reverse electro-dialysis (1).

Reverse electro-dialysis works by driving ions across a series of cation- or anion-selective membranes (**Figure 1**). This diffusion of the ions across a membrane is caused by the large ion concentration gradient between freshwater and saltwater. Unfortunately, if the ions can freely diffuse, no power will be generated since both types of ions will pass across the membrane. However, if the saltwater and freshwater are separated by an ion-selective membrane, then only positive or negative ions will be allowed to flow across. Since only one type of ion is crossing to the freshwater, this will lead to a difference in electric charge and potential across the two reservoirs, as the positive and negative ions become separated (2). This potential energy can then be harnessed with electrodes to create current similar to a battery (2). The membrane created needs to be small and selective enough to only let specific ions through, as if both cations and anions are moved through the membrane, no potential difference will be created (1).

Nanotubes allow for the creation of these ion-selective channels (3). Such nanotubes are hollow cylinders one atom thick, through which ions may pass. The membrane in this study is one with boron-nitride nanotubes as pores,

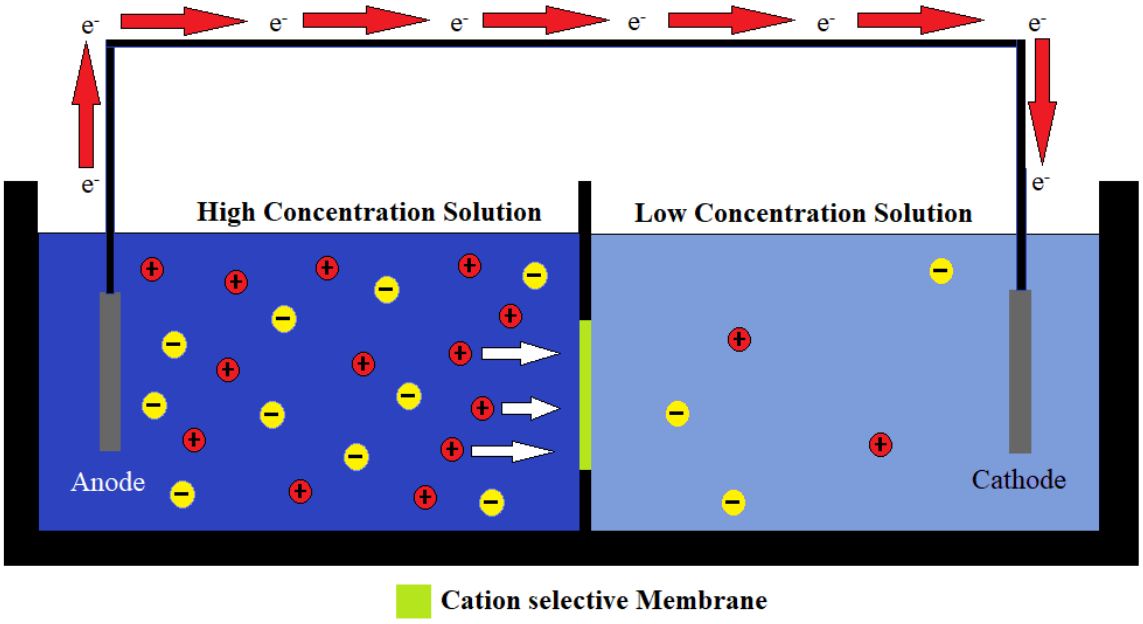

Figure 1. Diagram explaining how power might be generated by such a reverse electro-dialysis, current may be generated via the ion concentration difference between brackish and fresh water. Only one type of ion is allowed to pass, which enables a potential difference to be created.

embedded in a polymer matrix. In such a membrane, the nanotubes will act as open channels for the ions to flow through while they are surrounded by a polymer matrix that provides structural support (1). Boron-nitride nanotubes are used because they have a negatively charged inner surface (4). This negatively charged inner surface not only allows for ion selectivity of positive cations, but also leads to increased flow speed through the membrane as the negative surface attracts positive charges (4). However, there are many problems that need to be addressed to create power-generating membranes, as they are not commercially viable yet and have only produced high power densities at very small scales (measurements of one nanotube) (1). Ultimately, our research found three problems that needed to be solved to produce efficient and economically viable construction of ion-selective membranes. First, the nanotubes need to be aligned to allow them to traverse the entire length of the membrane. Otherwise, the nanotubes would not form an open channel through both ends. Second, the nanotubes must be concentrated to have the membrane with enough pore density to produce an economically viable amount of energy. Finally, agglomerations in the nanotubes must be removed, as this would lead to holes or defects in the membrane.

There are many desirable characteristics associated with the polymer layer of the membrane. First, it must be curable in a reasonable time, as long curing times would make creating the polymer unfeasible for mass production. This was achieved by mixing a photo-initiator into the polymer that would cure when exposed to ultraviolet (UV) light. Second, it must be resistant to plasma etching, as each membrane in our work is etched to remove the caps on the nanotubes, this is a necessary step to open the nanotubes to be channels, as seen in previous carbon and boron-nitride nanotube studies (5). Third, it must be a thin thickness of around 5-10 microns, as the relatively short nanotubes must pass all the way through the membrane. Finally, it also has to have mechanical strength, as it cannot rip or tear, which would render the membrane useless, as the saltwater and freshwater would simply mix. The first objective of this study was to test for these characteristics.

We aligned and concentrated the nanotubes by attaching iron oxide particles to the nanotubes in suspension, and then applying a strong magnetic field, as has been shown effective in previous studies (6-7). However, the details of this process are not well understood or documented, although such magnetic alignment has been performed in the past, notably on boron nitride platelets (7). The second objective of this study, therefore, was to investigate the relationship between the magnetic field and length of the nanotubes.

We hypothesized that the Soltech 704 (SU704) will prove to be the best polymer in terms of both etching and curing results, out of the three urethane acrylates we tested. In addition, we predicted the relationship between the magnetic dipole moment and the length of the nanotubes to be linear. These hypotheses were based on the fundamental chemistry of the components: Soltech 704 is a tri-functional polymer compared to the di-functional Soltech 710 (SU710), another polymer used in the study, with three attachments to nearby subunits compared to two (8). Trifunctional and difunctional simply refer to the amount of attachments each polymer subunit has to others, which was the only significant difference between the two polymers. This led us to predict

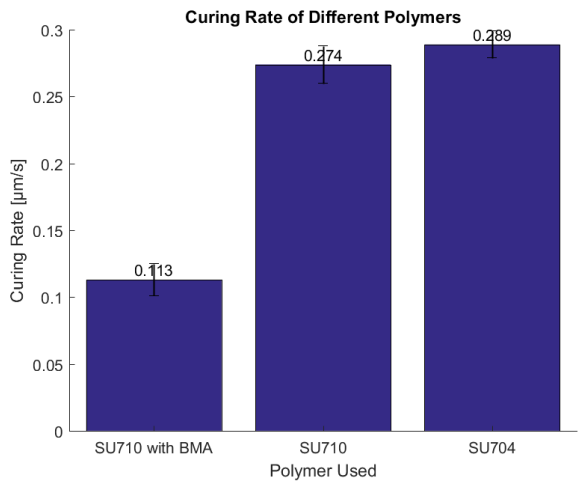

Figure 2. SU704 has the fastest curing rate. Average curing rates (µm/s) of SU704, SU710, and SU710 with BMA (10 different samples tested). Error bars represent standard deviation.

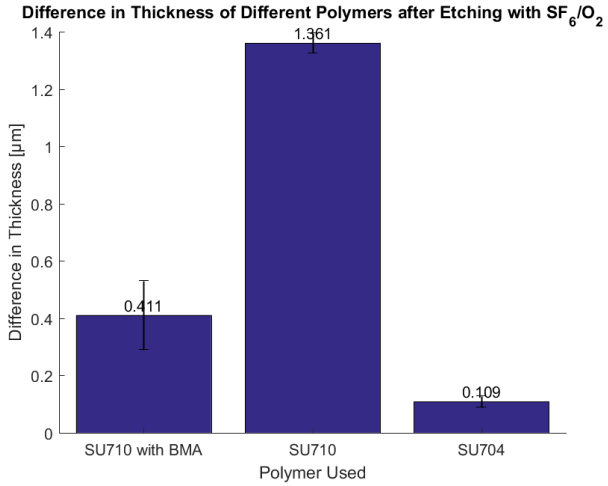

Figure 3. SU704 has the lowest etching rate, thus it is the most resistant. The difference in thickness of polymers (µm) under a 50/50 mixture of SF6 and O2 after etching for a given amount of time (three minutes). Error bars represent standard deviation.

that 704 would be stronger and thus more resistant to plasma etching, while curing faster. The relationship with dipole moment and length is predicted to be linear, due to similar effects with carbon nanotube alignment (5), as well as the fact that a longer nanotube leads to a greater amount of iron oxide units attached. The impact of our study will be to create more durable and efficient membranes, which may be more effective at generating power.

RESULTS

The first of our results are the average rates of curing, given in microns per second (**Figure 2**). The curing rates we calculated were an average taken of 10 membranes. The curing rates were found by curing several membranes for fixed amounts of time, then measuring the thickness. In this study, three polymer materials were tested: SU704, SU710, and SU710 mixed with butyl methacrylate (BMA), an additive that allowed the polymer to be more easily mixed, as well as being more resistant to etching. Only these three polymers were used because they have shown strong chemical resistance in previous studies (9).

The curing rates of the pure SU704 and SU710 membranes were almost the same, with that of the SU704 being slightly higher; however, t-test analysis found no statistical difference between the two. Both of these showed a thickness of roughly 17 µm after a 60 second cure time, with an average rate of 0.27 µm/s for the SU710 and 0.29 µm/s for the SU704 and standard deviations of 0.014 µm/s and 0.010 µm/s, respectively. However, the curing rate of the SU710 mixed with BMA was significantly lower than the rates of both of the other polymers, at 0.11 µm/s with a standard deviation of 0.012 µm/s. We found that SU710 with BMA cured at a rate significantly lower than the other two polymers (Student's t-test, *p*-value = 0.032). No intervals above 60 seconds were chosen as after 60 seconds, many of the membranes were too thick and exceeded the desired range of 5-10 microns.

This test showed that the better membranes were either SU704 or SU710, as they could be created faster. A faster cure was desirable for this test because that would mean the membrane requires less time and energy to make.

We then performed experiments to find the etching rates of the three polymers, which is a measure of how much of the polymer was etched away by the plasma after a given amount of time. We found that plasma etching caused the polymer thickness to decrease since the plasma etching removes part of the upper surface of the polymer. When SF_6 was used for etching, the polymer with the most resistance was SU704, as it had the lowest average thickness change from the initial thickness (0.109 µm, 0.020 µm standard deviation) (**Figure 3**). Both SU710 and SU710 mixed with BMA had thickness decreases nearly an order of magnitude higher than the SU704 (1.361 µm, 0.035 µm standard deviation and 0.411 µm, 0.120 µm standard deviation, respectively). Moreover, SU704 had a significantly lower etching rate (Student's t-test, *p*-value = 0.041).

The thicknesses of the membranes decreased from the initial in the SF_6 and O_2 mixture etching as well (**Figure 4**). Those two gases were chosen due to their ability to etch open the boron nitride nanotubes compared to the pure SF6. Similar to the SF_6 etching, the most etch-resistant polymer was SU704 again, as there was the least average change between the initial and final thicknesses for this polymer (0.067 µm, 0.015 µm standard deviation). Again, the SU710 and SU710 with BMA had much higher average etching thickness differences (0.888 µm, 0.027 µm standard deviation, and 0.556 µm, 0.023 µm standard deviation, respectively) (Student's t-test, *p*-value = 0.025. The t-test results also showed that the SU704 had a significantly lower etching rate, at a 5% confidence level.

The relationship between the magnetic dipole moment

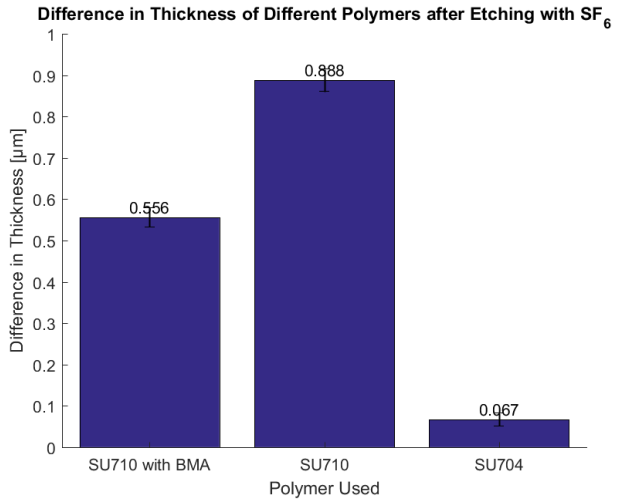

Figure 4. SU704 has the lowest etching rate, thus it is the most resistant. The difference in thickness of polymers (µm) under SF6 plasma gas after etching for a given amount of time (three minutes). Error bars represent standard deviation.

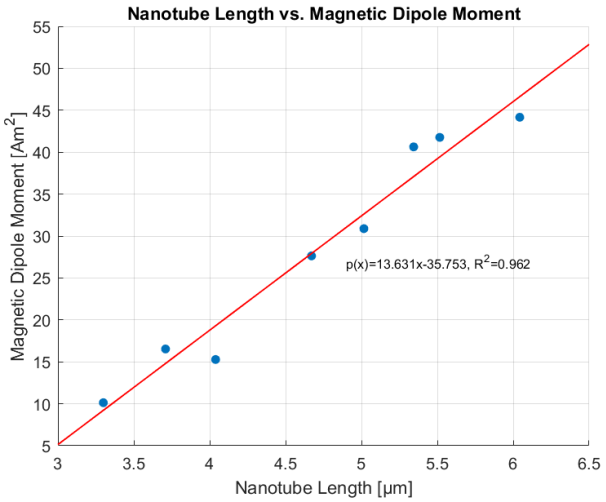

Figure 5. Nanotube length and magnetic dipole moment are linearly correlated. Graph showing the relationship between the nanotube length (µm) and the corresponding magnetic dipole moment (Am^2), giving a linear relationship with a r coefficient of 0.962.

and the length of the tube was linear, with a longer tube corresponding to a generally larger magnetic dipole (**Figure 5**). This data was collected by video recording nanotubes of different lengths in a microscope under a magnetic field. This correlation had a very high correlation coefficient of 0.962 (**Figure 5**). Since magnetic field multiplied by the magnetic dipole moment is equal to the torque, this relationship means that longer nanotubes experienced a greater torque when placed into a magnetic field of a certain strength. As torque is rotational equivalent of force, the greater torque on the nanotube would be expected to make the longer nanotubes align more quickly.

DISCUSSION

We conclude that the best polymer material out of the three tested was the SU704 membrane. This is because it performed significantly better than SU710 with BMA in both the curing rate test and significantly better than all the other polymers in the etching resistance test. SU704 displayed all four of the desired characteristics for nanotubes: reasonable strength, etching resistance, fast curing time, and 5-10 µm thickness. This investigation showed that by adopting this polymer, the resulting membranes created will not only have a stronger resistance to etching and therefore have fewer defects, but can also be produced more quickly in large quantities due to the faster curing rate. One plausible explanation for such results is that the BMA prevented the crosslinking of the photoinitiator and inhibited the curing. This would account for the much lower SU710 with BMA curing rate.

In addition, it can be concluded that the length does have a large positive relationship with the magnetic dipole moment of the nanotube. This investigation supported this by analyzing several nanotubes under a magnetic field and microscope. The results will be used in our future work to optimize the magnetic field alignment time for membranes with different thicknesses.

This study is innovative as it was one of the first to analyze how boron nitride nanotubes and the membranes that can be created with them (1, 8). Previous studies have shown the mechanics of the fluid and ion transport through the nanotubes (4), but none have investigated polymer properties for the creation of membranes. Similarly, some studies have investigated the thermal properties produced by using a magnetic field to achieve alignment for boron nitride platelets (8), but this study was one of the first to investigate the mechanics of how boron nitride nanotubes will align, and what relationships might be found between length, magnetic field strength, and magnetic dipole moment. This study may help to fill in those gaps in our knowledge by illustrating a viable way to create nanotube membranes, as well as giving insight on the alignment process.

Future research will investigate the relationship of the nanotubes with a variable magnetic field. I have already started this work with the creation of a Helmholtz coil to create a uniform but variable magnetic field on the microscope. This means that a variable magnetic field can be produced at will by altering the current, which will allow for more detailed studies of the nanotubes.

Although mostly speculation at the current stage, results of this study may be used to create global networks of clean electricity by producing more efficient ways to create ion-selective nanotube membranes. In addition, these membranes can be used for other applications, such as filtration or desalination.

METHODS

Membrane Preparation

There are many steps to creating the polymer layer of the nanotube (**Figure 6**). The first step was to prepare each of the polymer solutions by mixing them thoroughly with a stirring rod with a 7.8% by volume concentration of Darocur 1173 (2-hydroxy-2-methylpropiophenone, Sigma-Aldrich, Inc.). Darocur 1173 is a specific photoinitiator used in this procedure because it cross-links and hardens when exposed to UV light, allowing the mixture to cure properly (10). This specific concentration of photoinitiator was chosen as it allowed for even curing throughout the mixture, as well as not compromising the structural strength of the polymer, and was determined by numerous tests.

The second step was to place the solution in a vacuum chamber for 24 hours. This was done to remove air bubbles that formed during the mixing of the photoinitiator and the polymer. This is necessary, as air bubbles interfere with the cross-linking during curing and lead to an uneven cure, which would cause decreased structural strength of the resulting polymer.

The third step was to place one drop of the mixture on a glass slide, which acted as a substrate. A quartz slide was placed on top of the drop, which compressed the drop into a thinner sheet, as well as limiting its exposure to air. Quartz was used for the upper glass slide, as it was more transparent than glass to UV light. After the quartz slide was placed, a UV lamp was shone onto the polymer for a specific amount of time. This allowed the thickness of the membrane to be controlled as a longer time allowed more of the polymer to be cured.

The fourth step was to remove the polymer off the quartz slide. The quartz slide was taken out and sprayed with acetone to remove excess polymer. Acetone was used for this application as it is a good solvent of the liquid polymer and is relatively cheap and available. Ethanol and distilled water were tested as solvents, and they did not work as well. Then, the remaining cured polymer on the glass slide was coated in more acetone to cause the membrane to swell. This swelling occurred because the acetone collected in large pockets underneath the cured polymer. This swelling was induced because it allowed the membrane to be more easily washed away with distilled water, as less area of the polymer was adhered to the quartz slide.

The final step was to mount the polymer onto a new plastic substrate. After the membrane was washed off the quartz slide, it was then carefully picked up with tweezers and dropped into a dish of ethanol. This intermediate step was done to remove folds in the membrane that may have occurred as it was washed off the quartz slide. Ethanol was used, as the surface tension of the ethanol slowly unfolded the cured polymer to its original state. Then, the unfolded membrane was picked up with tweezers and placed in a dish filled with distilled water. The distilled water was used to clean excess ethanol or acetone off of the polymer. Then, the polymer was placed onto a flexible plastic ring that allowed for mobility and easier testing, while still providing enough structural strength.

Curing Rate Test

This test was done by creating several membranes but changing the amount of time that the UV lamp was turned

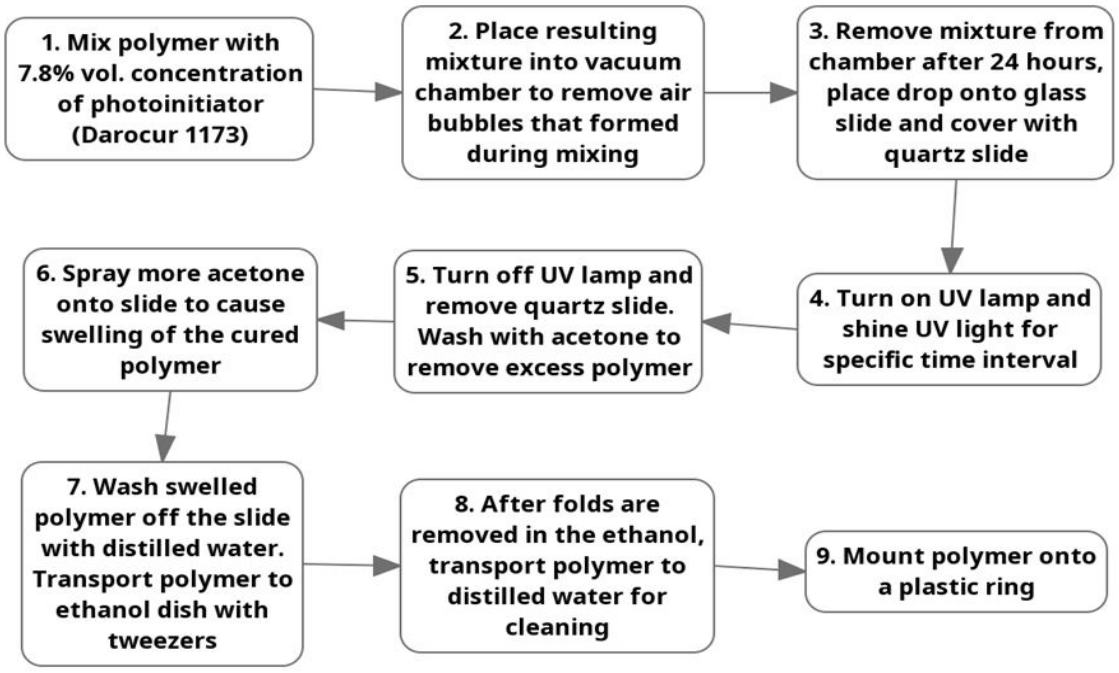

Figure 6. Chart explaining how cured polymer was created for this study. Polymer is first mixed, the cured with the UV light for a given amount of time, then washed with acetone to remove from a quartz slide.

on for each of them. For each different type of polymer, 4 different types of membranes were produced: one with the UV lamp on for 5 seconds, one with the UV lamp on for 10 seconds, one with the UV lamp on for 20 seconds, and one with the UV lamp on for 60 seconds.

The thicknesses of the finished membranes were then measured with a Filmetrics F3-sX series reflectometer. This device measured the thickness of the membrane by comparing the wavelengths of light reflected from top and bottom edges of the membrane. Three separate measurements were taken for each membrane, which were then averaged to find the thickness. The thickness could then be plotted against amount of time the UV lamp was curing the polymer for to find the curing rate of the polymer.

Etching Tests

The second test was the etching resistance test. This test was done to find which of the polymers was the most resistant to plasma etching. A more resistant polymer was desired as this would decrease the chances of etching causing a defect such as a hole or tear in the polymer.

First, polymers of the three chemicals were cured and each of their average thicknesses were measured with the reflectometer. Then, six of the membranes were etched by pure sulfur hexafluoride (SF_6) in a RF plasma etcher for three minutes, with two of each type of polymer: SU704, SU710, and SU710 with BMA. Another six membranes with two of each type were etched by an oxygen-sulfur mixture of 50% of each gas for three minutes. These gases were used because they have been proven to be capable of etching boron nitride nanotubes (10).

After the etching was finished, the thicknesses of each of the membranes were measured again with the reflectometer. By comparing the difference in thickness of the membranes before and after the etching process, both the amount of polymer etched away and the etching rate for each of the polymers could be calculated.

Nanotube Alignment Analysis

The nanotubes were first functionalized by attaching iron particles to them, and then analyzed while aligning in a set magnetic field. The procedure for this is explained below.

The nanotubes used in the experiment were boron nitride tubes purchased from Naieel Co. These tubes had a diameter of 30-50 nm and a variable length of at least 10 µm (12). Initially, the tubes were suspended and dispersed in isopropyl alcohol (IPA) at concentrations of about 0.1 mg/mL. IPA was chosen as an initial solvent for the nanotubes since they are both nonpolar and easily miscible (11). After mixing, the nanotubes were sonicated for five minutes in a bath sonicator to create a better dispersion and to break up clumps of nanotubes. After being dispersed, the IPA was evaporated and replaced with water and re-sonicated for 15 minutes. Water was used as a solvent since IPA was not compatible with the iron particles. After sonication, the iron particles were added at a concentration of 0.01 mL of the particle suspension for every 5mL of the nanotube suspension. This concentration was tested to be an optimal concentration, as it ensured that enough iron attached to each nanotube. After three hours of mixing, the particles clumped and attach to the nanotubes, turning them into magnetic dipoles able to be aligned by outside fields. Finally, the excess iron particles were centrifuged out, leaving only the nanotubes with iron particles attached to them. This relatively dilute solution of

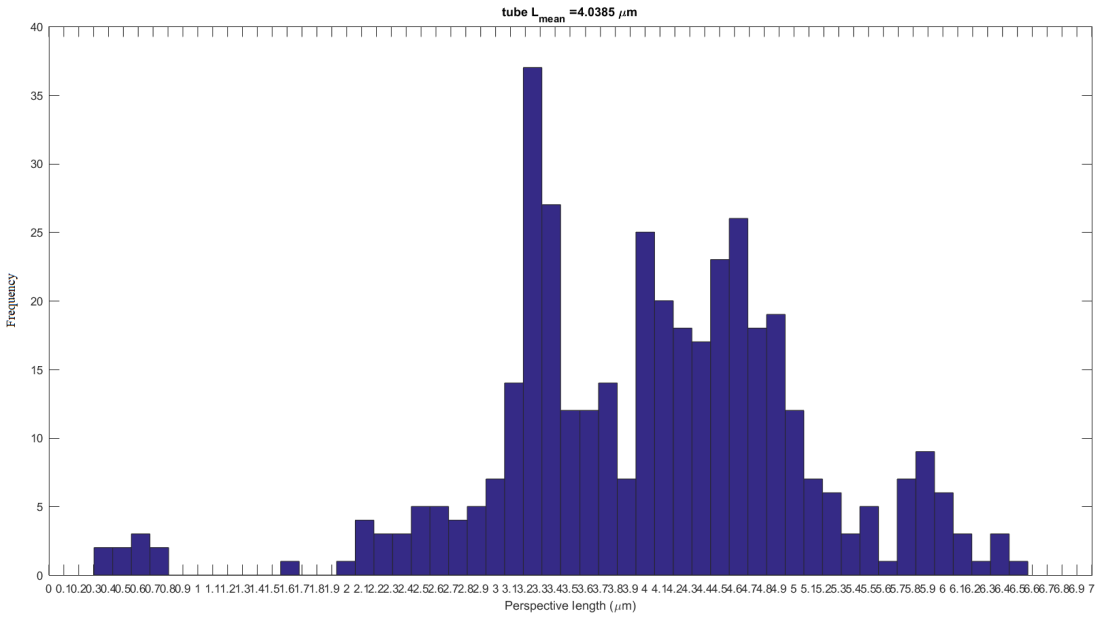

Figure 7. An example histogram representing the nanotube lengths (µm) recorded from each frame of the video of the nanotube under the microscope. The calculated length was the average from this distribution.

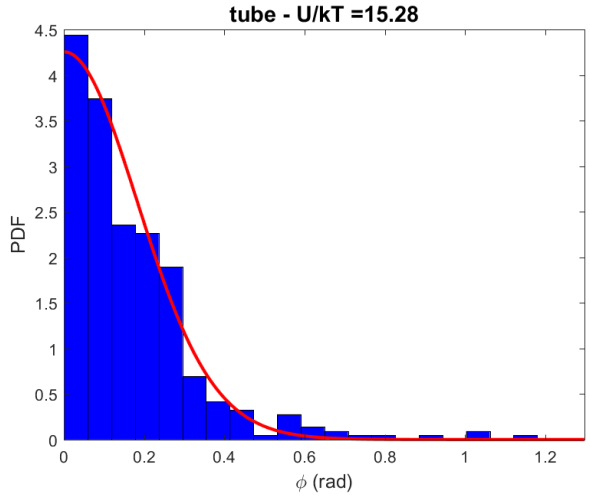

Figure 8. An example histogram representing the angle probability distribution from the recorded video of nanotubes under the magnetic field. Angle of the nanotube is measured with respect to the magnetic field direction.

functionalized nanotubes was ideal for investigating under a microscope.

The nanotubes were then analyzed using the microscope with a 40x objective lens. They were placed under a set magnetic field created with permanent magnets. This field could be varied with magnet placement and was 150 Gauss strong. Because of the magnetic iron particles attached to the tubes, this magnetic field aligned the tubes in one direction. To analyze the results, a camera was turned on to record the tubes' motion by recording a short video of the tube for up to one minute. After recording the video, individual frames of the video were analyzed by a MATLAB program that found the length of the tube and the angle it was at, relative to the angle of the magnetic field. The video was taken at 20 frames per second, amounting to 1200 frames of data for each nanotube.

These values were plotted on separate histograms. The histograms showing the length of the tube in each frame were plotted and averaged to find a length (**Figure 7**). The angle distribution is similarly plotted for each frame (**Figure 8**). After recording the values, the histogram of the angle distribution is fitted (**Figure 8**). This fit is used to calculate the dipole moment of the tube - the strength of the induced magnetic field of the tube. This dipole moment was then plotted against the length of the tube to see the relationship.

Received: June 5, 2020
Accepted: September 21, 2020
Published: September 28, 2020

REFERENCES

1. A. Siria, M.-L. Bocquet, and L. Bocquet, L., "New avenues for the large-scale harvesting of blue energy," *Nat. Rev. Chem.*, vol. 1, 2017, pp. 00-91. doi:10.1038/s41570-017-0091
2. Weinstein, J. N., and F. B. Leitz. "Electric Power from Differences in Salinity: The Dialytic Battery." *Science*, vol. 191, no. 4227, 1976, pp. 557-559. doi:10.1126/science.191.4227.557.
3. Hilder, T.A., Gordon, D. and Chung, S.-H. "Boron Nitride Nanotubes Selectively Permeable to Cations or Anions." *Small*, vol. 5, 2009, pp. 2870-2875. doi:10.1002/smll.200901229
4. Siria, Alessandro, *et al.* "Giant Osmotic Energy Conversion Measured in a Single Trans-Membrane Boron Nitride Nanotube." *Nature*, vol. 494, no. 7438, 2013, pp. 455-458. doi:10.1038/nature11876.
5. Castellano, Richard, *et al.* "Electrokinetics of Scalable, Electric-Field-assisted Fabrication of Vertically Aligned Carbon Nanotube/Polymer Composites." *Journal of Applied Physics*, vol. 117, no. 21, 2015, pp. 214-306. doi:10.1063/1.4921948
6. Chao Yuan, *et al.* "Thermal Conductivity of Polymer-Based Composites with Magnetic Aligned Hexagonal Boron Nitride Platelets." *ACS Applied Materials & Interfaces*, vol. 7, no. 23, 2013, pp. 13000-13006. doi:10.1021/acsami.5b03007
7. Du, Chunyu, *et al.* "Mussel-Inspired and Magnetic Co-functionalization of Hexagonal Boron Nitride in Poly(vinylidene fluoride) Composites Toward Enhanced Thermal and Mechanical Performance for Heat Exchangers." *ACS Applied Materials & Interfaces*, vol. 10, no. 10, 2018, pp. 34674-34682. doi:10.1021/acsami.8b14154
8. "Aromatic Urethane Acrylate." SOLTECH LTD. - UV Tech, UV Oligomer, UV Acrylate, UV Curing, UV Coating, Oligomer, Acrylate, Ultraviolet, Photo Chemistry, 2010.
9. Castellano, Richard J., *et al.* "Scalable electric-field-assisted fabrication of vertically aligned carbon nanotube membranes with flow enhancement." *Carbon*, vol. 157, 2020, pp. 208-216. doi: 10.1016/j.carbon.2019.10.012
10. Decker, C, *et al.* "UV-Radiation Curing of Acrylate/Epoxide Systems". *Polymer*, vol. 42, no. 13, 2001, pp. 5531-5541, doi:10.1016/s0032-3861(01)00065-9.
11. Popov, Cyril, *et al.* "Chemical Vapor Deposition of BC2N Films and Their Laser-Induced Etching with SF6." *Thin Solid Films*, vol. 312, no. 1-2, 1998, pp. 99-105. doi:10.1016/s0040-6090(97)00694-9.
12. "Products Purchase." Naieel.com, 2016, naieel.com/naieel/bbs/content.php?co_id=mall.

JOURNAL OF
EMERGING INVESTIGATORS

Article

Using the COmplex PAthway SImulator, stage analysis, and chemical kinetics to develop a novel solution to lower Tau concentrations in Alzheimer's disease

Peyton Carroll, Samhith Kakarla
Fremont High School, Sunnyvale, California

SUMMARY

Alzheimer's is a disease which afflicts 5.5 million Americans. In this study, we asked whether a Tau immunotherapy treatment, Hsp70 protein treatment, or dual treatment approach of both the Tau imunotherapy treatment and Hsp70 protein treatment leads to a greater reduction in Tau protein concentration. As a high concentration of Tau protein is directly related to Dementia and Alzheimer's, the proposed treatment which reduces the Tau protein concentration the most is the best Alzheimer's/Dementia treatment. We determined through our experimentation that the Tau immunotherapy treatment results in the least Tau protein concentration in early and advanced cases, less than the joint treatment and single Hsp70 protein treatment. However, the joint treatment was more effective at reducing Tau levels when initial Tau levels were consistent with those found in medium stage Alzheimer's. The dual treatment had similar effects as the immunotherapy treatment, but with less impacts to Tau concentration. The Hsp70 treatment slowed the increase in Tau concentration, delaying the simulated progression of the disease but not stopping the disease. However, the Hsp70 treatment had the lowest standard deviation, demonstrating it is the most consistent treatment. Overall, we were able to display that the effectiveness of the treatment ultimately relies on the stage of Alzheimer's.

INTRODUCTION

Alzheimer's disease is a disease that causes loss of neural function such as loss of memory and logical thinking to the extent where daily functions are difficult to carry out (1). Dementia is known as the general sphere of diseases which cause memory loss, while Alzheimer's disease is the most common type of Dementia, accounting for 60% to 80% of all cases of Dementia (1). Other forms of Dementia are Lewy body dementia, frontotemporal disorders, and vascular dementia (2). Alzheimer's disease affects mostly elderly individuals over the age of 65 but is not a natural part of aging (1). Alzheimer's disease is a progressive disease, as it does not manifest itself in its full form initially (1). One usually has minor memory loss initially, which then progresses into more major memory loss (1). Alzheimer's disease has no cure, but medications can make the disease more tolerable (1).

Currently, more than 5.5 million Americans live with Alzheimer's disease (2). These individuals suffer tremendously due to their lack of mental capability (2). Alzheimer's disease is also deadly, as it is the sixth leading killer in the United States for all ages and the third leading killer for those 65 years old or older (2).

Scientists have narrowed down the cause of Alzheimer's disease to two factors: plaques and Neurofibrillary tangles (3). These plaques are formed from beta-amyloid, which is residue from the protein, amyloid precursor protein (3-4). Currently, the function of the amyloid precursor protein is unknown (4). The amyloid precursor protein extends as a long rod, extending from inside the cell through the cell membrane to outside the cell (4). Scientists have determined the amyloid precursor protein splits into several pieces which reside both inside and outside the cell (4). One of the cut pieces called is beta-amyloid (4). These beta-amyloids join to form large plaques, which harms neurons and consequently brain function (3). The beta-amyloids first form very small groups, called oligomers, then chains of these oligomers form fibrils, then collections of these fibrils to build beta-sheets. The beta-amyloids are particularly sticky, resulting in a greater tendency to form large blocks (4). The brain naturally builds microtubules with Tau proteins to transfer nutrients and signals between neurons (3). Tau protein is malleable, as they are used to build microtubules between neurons in a variety of angles and shapes (3). When a patient has Alzheimer's disease, the patient's Tau protein forms abnormal Neurofibrillary tangles, which block the connections between the neurons (3).

One potential solution to decreasing the amount of Tau protein is through using Tau immunotherapy (5). Tau immunotherapy involves usage of antibodies to attach themselves to the Tau protein and remove them from the brain (6). The Tau immunotherapy approach offers insight into removing the Tau residing in the brain. This treatment has been successful in treating mice and will move to human trials in the future. Although this treatment has promise, it is built in removing the Tau once it is created not on slowing or stopping the creation of the Tau.

Another solution to decreasing the amount of Tau proteins

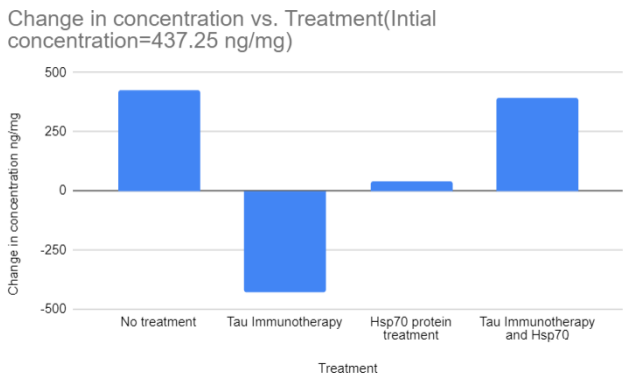

Figure 1. The resulting Tau concentrations and the change in Tau concentration for initial concentrations of 473.25 ng/mL. No treatment, Tau immunotherapy treatment, Hsp70 protein, or dual treatment of Tau immunotherapy and Hsp70.

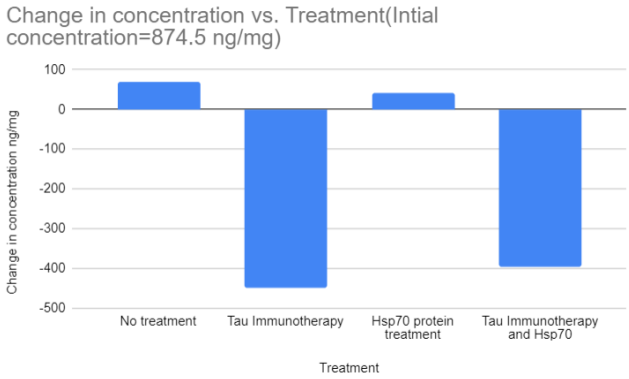

Figure 2. Resulting Tau concentrations and the change in Tau concentration for initial concentrations of 874.5 ng/mL. No treatment, Tau immunotherapy treatment, Hsp70 protein, or dual treatment of Tau immunotherapy and Hsp70.

is through using the Hsp70 protein (7). Hsp70 is a protein that has been shown to decrease the Tau protein production in the brain (8). Hsp70 does this through decreasing mutations in the MAPT gene that encodes Tau, thus limiting the production of Tau protein (8). The weakness with this approach is the production of Tau is decreased, but the current amount of Tau in the patient's brain remains the same (8). The Hsp70 treatment cannot reduce the amount of Tau in the brain, only the production of that Tau (8).

We utilized a simulation to determine whether a Tau immunotherapy treatment, Hsp70 treatment, or joint treatment of Tau immunotherapy and Hsp70 treatment resulted in the greatest decrease in Tau protein concentrations. We determined this through running simulations with a COmplex PAthway SImulator (COPASI). We modeled the brain through COPASI, a chemical simulator.

The brain contains 86 billing brain cells and 7000 connections. As we did not have enough computing power to simulate such a complex organ, so we simplified the brain to 86,000 neurons. We ran the simulations for different initial concentrations of a variety of different chemicals involved in Tau production and removal and measured the results for the Tau concentration over time. We hypothesized the dual treatment would be the most effective, as we reasoned when the amount of antibodies are increased, the rate of Tau removal should increase. This coupled with the decrease in the Tau production with Hsp70 would make the dual treatment most effective. In the simulations, we determined the Tau immunotherapy treatment approach was the most effective Tau treatment as it caused the greatest decrease in Tau concentration.

RESULTS

We simulated the effects of Tau immunotherapy treatment, Hsp70 protein treatment, and a dual treatment approach. We used the COPASI simulator to collect data on each of these treatments and compared the Tau concentrations over time to determine the most effective treatments. The Tau protein concentration in the brain for an Alzheimer's patient is 874.5 ± 51.34 ng/mL (8). We set the Tau concentration to 437.25 ng/mL, 874.5 ng/mL, and 1749 ng/mL. We conducted four different trials for each treatment, with a total of twelve trials. Each trial consisted of an initial concentration of half the Tau concentration (437.25), the Tau concentration (874.5), and double the Tau concentration (1749).

In **Figure 1**, we simulated early stage Alzheimer's, with Tau concentrations at 437.25 ng/mL. We observed the best treatment here was Tau immunotherapy, as it reduced the Tau concentration more than other approaches. In the early stage, Tau immunotherapy was the only treatment which decreased the Tau concentration. Additionally, both the joint treatment and Hsp70 slowed the growth of Tau compared to the control simulations but did not lower tau concentrations. In **Figure 2**, Tau immunotherapy was also the most successful treatment, as it caused the greatest decrease in tau. In the middle stage simulations, the joint treatment also caused a decrease in tau concentration, but not as much as Tau immunotherapy alone. Hsp70 reduced Tau production in comparison to the control simulations but did not lower tau concentrations. However, in **Figure 3**, the joint treatment of Hsp70 and Tau immunotherapy alone was most effective.

In summary, every treatment in every simulation produced better results than the control simulations. In early and middle stage Alzheimer's the Tau immunotherapy was most effective. In late stage Alzheimer's, the dual treatment was more effective.

DISCUSSION

In this study, we simulated the effects of Tau immunotherapy treatment, Hsp70 treatment, and a joint treatment of both Tau immunotherapy and Hsp70 treatment to determine the most effective Tau treatment as a possible cure to Alzheimer's disease.

Figure 1 lists the changes in concentrations of Tau protein in simulations without treatment, with Tau immunotherapy treatment, Hsp70 treatment, and a dual approach of both

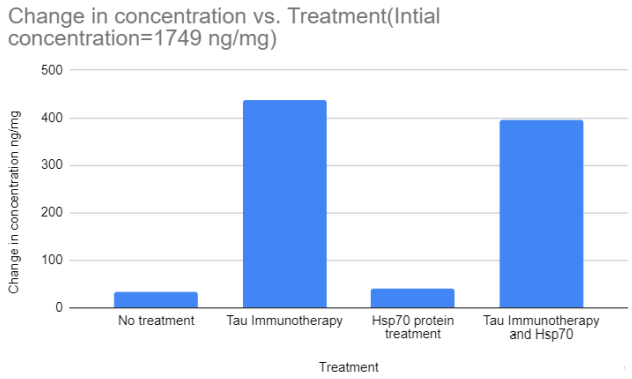

Figure 3. The resulting Tau concentrations and the change in Tau concentration for initial concentrations of 1749 ng/mL. No treatment, Tau immunotherapy treatment, Hsp70 protein, or dual treatment of Tau immunotherapy and Hsp70.

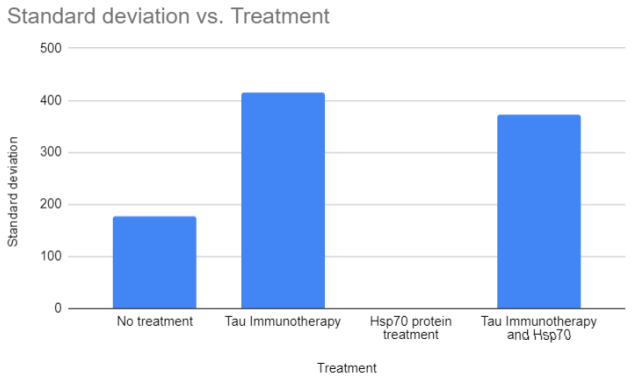

Figure 4. Standard deviation calculations for all four treatments.

Tau immunotherapy treatment and Hsp70 treatment. The Tau concentration in these simulations were 437.25 ng/mL, best modeling a patient in the early stages of Alzheimer's. In this case, the Tau concentration increased 427.474 ng/mL in the non-treatment simulation. Therefore, any treatment which resulted in a lower increase in Tau concentration would be more effective than no treatment at all. The Tau immunotherapy treatment was the most effective of all the treatments in **Figure 1**, resulting in Tau concentration decreasing by 427.473 ng/mL. The next most effective Tau treatment was the dual approach, which resulted in a decrease of 393.6473 ng/mL. The least effective approach was the Hsp70 treatment, which resulted in a 41.61 ng/mL increase in Tau concentration. Although the Hsp70 treatment was the only treatment which resulted in an increase in Tau concentration, it must be noted the increase in Tau in the Hsp70 treatment was less than that in the no treatment group, indicating Hsp70 is a valid way to slow the progression of Alzheimer's but not cure it. From the data we gathered from the 427.474 ng/mL Tau concentration group, we can conclude that the Tau immunotherapy is likely to be effective for patients with early stages of Alzheimer's.

Hsp70 treatment was more effective than no treatment, despite the increase in Tau concentration. Overall, Hsp70 was the least effective treatment, although it still slowed the progress of the disease, while the Tau immunotherapy treatment was the most effective treatment for the 874.5 ng/mL Tau concentration simulation.

Then, we reviewed the effectiveness of the treatments when the Tau concentration is 1749 ng/mL (**Figure 3**). This Tau concentration was used to simulate patients who are in the advanced stages of Alzheimer's disease. The most effective treatment was the Tau immunotherapy treatment, which results in a decrease of 437.25 ng/mL in the Tau concentrations.

With **Figures 1-3**, we were able to determine which treatment was most effective in particular stages of Alzheimer's. However, another important factor is standard deviation, given we do not know the Tau concentration. We determined the Hsp70 protein treatment had the lowest standard deviation, and therefore was the most consistent. Secondly was the no treatment approach. However, although the standard deviation was second lowest, standard deviation is how much the data points deviate. Because of this, the no treatment was consistent, but consistently ineffective. The highest standard deviation for the treatments was Tau immunotherapy.

Overall, the Tau immunotherapy treatment resulted in the greatest decrease in Tau concentration in the patients who were in early and advanced stages of Alzheimer's. The joint treatment was more effective for medium stage Alzheimer's. Due to the standard deviation calculations, the Tau immunotherapy treatment is not the most consistent given we do not know the Tau concentrations. If we do not know the Tau concentrations, the Hsp70 protein treatment is most consistent. We are not entirely sure why the Tau immunotherapy treatment is more effective in the early stages and finals stages, but it does validate our model. In a poorly made model, the joint treatment would be more effective in all stages, as it would be simply the addition of two treatments. However, here we can see the joint treatment was effective only one of three times.

Future experiments would include testing other treatments to Alzheimer's and other combinations of treatments to find an even more effective treatment and testing these treatments in animal models, such as mice.

METHODS

We used the COPASI simulator to determine the Tau concentrations over time with Tau immunotherapy treatment, Hsp70 treatment, and dual treatment approach. We used the Tau protein concentration to determine the most effective treatment.

We used COPASI version 4.27, Windows 64 bit. We imported a neuron environment to simulate where the reactions will occur. We also manually created 7 species: Tau, Hsp70, Hsp1, Binding immunoglobulin protein, MAPT, TauN

Table 1. Kinematics equations used in COPASI.

Parameter	Reaction	Rate Law
Hsp70_creation	HSP1 + "Binding immunoglobulin protein" -> Hsp70	Mass action(irreversible)
Tau_Creation	MAPT -> Tau; Hsp70	Mass action(irreversible)
Tau_destrction	Tau + Tau immunotherapy_Drug -> TauN	Mass action(irreversible)

and Tauimmunotherapy_Drug. We created three reactions: Hsp70_creation, Tau_Creation and Tau_destrction. We then ran the simulations with varying amounts of initial concentration.

We defined a function which gave the end points of the brain, then randomly generated neuron locations between those endpoints. We ensured neurons were not closer than 20 nanometers. We then connected close neurons to each other. At each of these neurons, we inserted tau proteins with 874.5 ng/mL, 437.25 ng/mL, and 1749 ng/mL. We then defined known reactions, as can be seen in **Table 1**. We then ran this simulation on our 86,000 neurons. We summed the remaining tau and recorded the results.

COPASI offered data in graphs in data tables. The graphs provided valuable visual analysis of the data but did not allow us to quantitatively measure which approach was more effective. Therefore, we used the data points from COPASI to measure quantitatively the most effective treatment.

Received: June 7, 2020
Accepted: September 22, 2020
Published: September 28, 2020

REFERENCES

1. Polis, B., Samson, A. O., and Wisniewski, T., "Chapter 1A New Perspective on Alzheimer's Disease as a Brain Expression of a Complex Metabolic Disorder", *Alzheimer's Disease*, 2019.
2. Weller, J. and Budson, A., "Current understanding of Alzheimer's disease diagnosis and treatment", *F1000Resesarch*, 2018. doi: 10.12688/f1000research.14506.1.
3. Gouras, G. K., *et al*. "β-Amyloid Peptides and Amyloid Plaques in Alzheimer's Disease", *Neurotherapeutics*, vol 12, no 1, 2015, pp. 3-11. doi: 10.1007/s13311-014-0313-y.
4. Medeiros, Rodrigo, "*The Role of Tau in Alzheimer's Disease and Related Disorders", CNS Neurosci Ther*, vol 17, no 5, 2010, pp. 514-24. doi: 10.1111/j.1755-5949.2010.00177.x.
5. Hoskin J. L., Sabbagh MN, Al-Hasan Y, Decourt B. "Tau immunotherapies for Alzheimer's disease". *Expert Opin Investig Drugs*. Vol 28, no 6, 2019, pp. 545-554. doi:10.1080/13543784.2019.1619694.
6. Campanella, Claudia, *et al*. "Heat Shock Proteins in Alzheimer's Disease: Role and Targeting." *International Journal of Molecular Sciences*, vol 19, no 9, 2018, pp. 2603. doi: 10.1080/13543784.2019.1619694.
7. Han, Pengcheng, *et al*. "*A Quantitative Analysis of Brain Soluble Tau and the Tau Secretion Factor.*" *Journal of Neuropathology and Experimental Neurology*, Oxford University Press, vol 76, no 1, 2017, 1, pp. 44-51. doi: 10.1093/jnen/nlw105.
8. Young, Zapporah T, *et al*. "Stabilizing the Hsp70-Tau Complex Promotes Turnover in Models of Tauopathy." Cell Chemical Biology, U.S. National Library of Medicine, 18 Aug. 2016, www.ncbi.nlm.nih.gov/pmc/articles/PMC4992411/.

JOURNAL OF
EMERGING INVESTIGATORS

Article

A novel approach to prevent and restrict early stages of cancer cell growth using a combination of moringa and sesame in a *Drosophila* model

Aryan Ganesh, Ganesh Vanamu
Solorsano Middle School, Gilroy, CA

SUMMARY

Cancer is a highly prevalent disease with many causes but no cure; here, we examined the efficacy of the naturally anti-inflammatory moringa and sesame plants to prevent or restrict cancer cell growth in *Drosophila melanogaster*. In our previous work, we showed that sesame and moringa individually repressed eye tumor formation in *D. melanogaster.* In this work, we studied combinations of moringa and sesame at different proportions to compare their effects in preventing cancer cell growth. We studied *D. melanogaster* eye tumors which allowed easy detection of the phenotypes with simple microscopes. As we increased the concentration of sesame and moringa in the mixture, the cancer symptoms improved. We showed that a diet consisting of a combination of 10% sesame and 15% moringa can be used to effectively prevent visible tumor growth in the *D. melanogaster* eye, and the endpoints were close to those of healthy, wild-type flies. This data showed improved tumor growth compared to the treatments used individually. We extended the study to restrict early stages of cancer using these treatments. Progeny of Gal4-Ret cross at four different stages of the lifecycle were treated with experimental food and compared to control sample flies. Our study showed this combination of Moringa and Sesame treatments during the second instar or third instar larvae could restrict the cancer cells growth. Therefore, we concluded that a combination of 15% moringa and 10% sesame could prevent cancer and restrict early stages of cancer growth in this specific model of cancer using *D. melanogaster.*

INTRODUCTION

Cancer is a group of diseases that still has no complete cure. It is estimated that the number of cancer cases will reach 24 million worldwide by 2035 (1). Cancer can affect any tissue or organ of the human body; breast, lung, prostate, liver, and stomach cancers are some of the primary cancers leading to death (2). Chemotherapy helps treat cancer for many patients, but not without significant adverse side effects such as hair loss, anorexia, malabsorption, and anemia, among others (3). As our body processes food, waste substances are produced which are known as free radicals also called reactive oxygen species. If the body cannot remove these free radicals effectively it can result in an oxidative stress that could harm cells and body function. Antioxidants are compounds that prevent the formation of these free radicals by inhibiting oxidation (4). Since chemotherapy can often be very taxing, we examined if a diet enriched with antioxidants could help prevent the onset of cancer or even lessen its progression in animals already affected by it.

Sesame (*Sesamum indicum*) and moringa (*Moringa oleifera*) have natural antioxidants that could be a way to prevent cancer or potentially even cure the early stages (5, 6). Sesame is an oilseed that has several anti-inflammatory and antioxidant properties and is very effective for the prevention of cardiovascular diseases (7, 8). Sesame consists of nutrients like proteins, carbohydrates, antioxidants, lignans, and tocopherols, among others (9). Sesame compounds inhibit the inflammatory mediator NF-κB and ERK/p38 MAPK signaling pathways, thereby suppressing inflammatory responses (10). Moringa is called the "miracle vegetable" because it is one of the most nutrient-dense plants on the planet (11). Studies have demonstrated that moringa has antiviral and anti-inflammatory properties and can treat viral infections and heart diseases as well as boost immunity (12-18). Moringa extract decreases NF-κB and increases the anti-inflammatory cytokines IL-10 and IκB-α(19).

Several animal species are routinely studied as cancer models in a laboratory setting. *Drosophila melanogaster* is one such model that has been extensively studied (20-21). 75% of disease-causing genetic variants in humans are also found in *D. melanogaster* where they have been shown to cause the same disease (22). *D. melanogaster* is a model that is very amenable to experimentation and study, particularly when working with the eye, as it allows for easy detection of phenotypes using simple microscopes. The RetMEN2B allele contains mutations observed in the multiple endocrine neoplasia (MEN) domain of *Ret*. *Ret* is an oncogene that causes retinoblastoma in *D. melanogaster* and causes lung and thyroid cancer in humans. Using the Gal4/UAS system, oncogenes such as *Ret* can be used to induce cancer in the *D. melanogaster* eye called a "rough eye" (an irregular and uneven, usually smaller eye). Gal4 is a tissue-specific transcriptional activator, derived from yeast, that can turn on activity for any gene with an upstream activator sequence (UAS) present. Male flies containing the UAS-RetMEN2B transgene can be crossed with a female GMR-Gal4 fly to produce offspring (Gal4-RET) that are susceptible to cancer (23-24). Expression of the RetMEN2B allele leads to phenotypes in the *D. melanogaster* eye that are similar to those observed in vertebrates, specifically increased proliferation and incorrect differentiation to neuronal cell types.

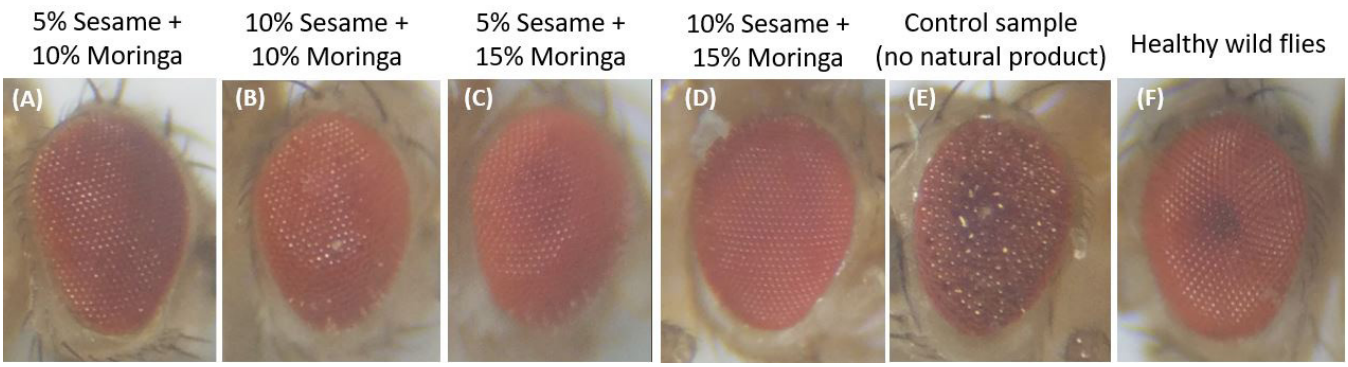

Figure 1. Flies treated with a 10% sesame and 15% moringa diet exhibited the most uniform ommatidia. A-F) Representative images of fly eyes from vial #1 (A; 5% sesame + 10% moringa), showing some nonuniform ommatidia and tumor symptoms (rough eye); vial #2 (B; 10% sesame + 10% moringa), also showing some nonuniform ommatidia and tumor symptoms; vial #3 (C; 5% sesame + 15% moringa), showing some nonuniform ommatidia but no tumor symptoms; vial #4 (D; 10% sesame + 15% moringa), showing no tumor symptoms and uniform ommatidia; vial #5 (E; water control), showing tumor symptoms and nonuniform ommatidia; and vial #6 (F; wildtype flies with water control), showing no tumors and uniform ommatidia. All images of progeny were taken five weeks after the parents mated. All experiments were performed with one trial.

In our previous study (25), we showed that individually, a 10% sesame diet showed some repressed tumor formation (showing smooth eye symptoms) and a 15% moringa diet showed good results in preventing cancer (showing both smooth eye and uniform ommatidia). In this work, we hypothesized that a combination of sesame and moringa in the right proportion would be even more effective as anti-cancer agent because of the great absorbance of the sesame (26) and presence of the anti-tumor compound niazimicin in moringa (27). We also hypothesized that we could find a combination therapy to restrict early stages of cancer.

RESULTS

Treatment of flies with combination of sesame and moringa for cancer prevention

To determine whether a dietary combination of sesame (Se) and moringa (Mo) could prevent *D. melanogaster* model of eye cancer better than either plant alone, we first wanted to determine the optimal concentration of each. In our earlier study, we tested doses in the range of 5–75% for sesame and 5–90% for moringa individually. We found that the optimal dose of sesame was 5–10% and of moringa was 10–15% when treated individually, so we used these doses in this current study (25). Gal4-RET flies were placed in four test vials, containing different combinations of sesame (5% or 10%) or moringa (10% or 15%). A 6th vial, containing healthy wild-type flies, was also taken without expression of any transgene (did not add any experimental food to the vial) for reference (**Table 1**). We also studied combinations of higher concentrations of sesame and moringa, including 15% sesame and 20% moringa, in 7th and 8th vials but flies did not survive (25). Higher concentrations killed the flies as it may be too high of a dose for the flies. The flies in all the vials were fed with Formula 4-24® Instant *Drosophila* Medium food (15ml), water (15ml) and 6-8 grains of yeast were added to each of the vials.

Fly eyes from vials 1 (5% Se + 10% Mo) and 2 (10% Se + 10% Mo) showed some nonuniform ommatidia and few tumor symptoms such as a rough eye phenotype, and fly eyes from vial 3 (5% Se + 15% Mo) showed a dark patch in the center with some nonuniform ommatidia (**Table 1, Figure 1**). Fly eyes from vial 4 (10% Se + 15% Mo) did not show any signs of tumors or nonuniform ommatidia. Fly eyes from control vial 5 (water only) showed clear, nonuniform ommatidia as expected. Fly eyes from the healthy wildtype flies in vial 6, which did not express any transgene, did not show any nonuniform ommatidia, as expected. Twenty flies were randomly chosen from each vial to score for tumors and uniformity of the ommatidia. We analyzed the percentage of flies that showed smooth eyes and uniform ommatidia in each vial (**Figure 2**). The percentage of smooth-eyed flies were 60%, 75%, 90%, 95%, 10% and 100% for vials 1–6, respectively. All of the experimental vials showed good improvement compared to the control vials. The combination of 10% sesame + 15%

Vial	Treatment	Type of flies	# of flies with smooth eyes	# of flies with uniform ommatidia	# of flies that died	Total # of flies tested
Vial #1	5% Se + 10% Mo	Gal4-RET cross	12	9	0	20
Vial #2	10% Se + 10% Mo	Gal4-RET cross	15	13	0	20
Vial #3	5% Se + 15% Mo	Gal4-RET cross	18	16	0	20
Vial #4	10% Se + 15% Mo	Gal4-RET cross	19	17	0	20
Vial #5	Water (Control)	Gal4-RET cross	2	3	0	20
Vial #6	Water	Healthy wildtype flies	20	20	0	20
Vial #7	15% Se + 15% Mo	Gal4-RET cross	N/A	N/A	20	20
Vial #8	15% Se + 20% Mo	Gal4-RET cross	N/A	N/A	20	20

Table 1. Description of the flies and type of food used in each of the 8 vials. Six vials, containing flies were given food with different combinations of sesame and moringa. 1 vial containing flies is given water and standard food and vial #6 had the healthy wild flies for reference. "N/A" indicates results not obtained due to fly death, while "Se" stands for sesame and "Mo" stands for moringa.

Figure 2. The combination of 10% sesame and 15% moringa prevented cancer symptoms in *D. melanogaster* eyes. A) The percentage of flies that showed smooth eye phenotypes were measured following treatment with the indicated combinations of sesame and moringa. The control sample consisted of mutant flies treated with a water control, whereas healthy wildtype flies were also treated with a water control. B) The percentage of flies that showed uniform ommatidia were measured following the same conditions as above. Twenty flies were randomly chosen from each vial to score for the tumors and uniformity of the ommatidia.

moringa showed the greatest effect, with 95% flies displaying smooth eye phenotypes. The percentage of flies with uniform ommatidia were 45%, 65%, 80%, 85%, 15% and 100% for each of the vials 1–6, respectively which showed that all the experimental vials have improved tumor symptoms compared to the control vials.

The lifespan of the flies, measured as the number of days flies were alive, with all the combinations of sesame and moringa was greater than the control flies (**Figure 3**). Survival percentage is the number of flies survived after certain days. As the number of days increased after a certain value, the survival percentage decreased and reached close to 0%. The median survival time for the control sample of Gal4-RET cross flies was 30 days and that of healthy wildtype flies was around 98 days. The median survival time for the test samples were between 55 days and 90 days. The median survival time for vial 1 (5% Se + 10% Mo), vial 2 (10% Se + 10% Mo), vial 3 (5% Se + 15% Mo), and vial 4 (10% Se + 15% Mo) were 55 days, 71 days, 71 days, and 90 days, respectively. This study also showed that as we increased the concentration of sesame and moringa in the mixture, the lifespan of the flies increased, with the best survival rate for the 10% sesame and 15% moringa combination. The slope of each of the curves appeared similar to one another as the number of days increases. This means that the number of flies that died per day was similar for each of the vials.

Treatment of flies with combination of 10% sesame & 15% moringa to restrict early stages cancer cell growth

Next, we wanted to test whether a combination of 10% sesame and 15% moringa could restrict early stages of cancer by administering this combination to the flies during different stages of the fly life cycle, specifically the second instar larval stage, third instar larval stage, pupal stage, and newly eclosed adult stage (**Table 2**). We examined the eyes of each fly for tumors and ommatidia appearance, two weeks after the larvae turned into adult flies. Eyes of the flies from vial 1 (second instar), showed a small area of tumor and uniform ommatidia in the rest of the area (**Figure 4A**). Fly eyes for the control sample (vial 2) compared to flies from vial 1 (second instar) showed complete rough eye (complete tumors, tumors formed on the entire area of the eye) and nonuniform ommatidia (**Figure 4B**). Thus, the 10% sesame and 15% moringa combination showed better performance in restricting cancer growth compared to the control sample.

Eyes of flies from vial 3 (third instar) showed few areas of tumor and uniform ommatidia in the rest of the area (**Figure 4C**). Fly eyes for the control sample (vial 4) compared to flies from vial 3 (third instar) showed complete rough eye and nonuniform ommatidia (**Figure 4D**) which indicates that the 10% sesame and 15% moringa combination had an effect in restricting cancer growth compared to the control sample.

Fly eyes from vial 5 (pupa) showed complete tumors and nonuniform ommatidia (**Figure 4E**) similar to the fly eyes for the control sample in vial 6 (**Figure 4F**). Fly eyes from vial 7 (newly eclosed) showed complete tumors and nonuniform ommatidia (**Figure 4G**) similar to the fly eyes for the control sample in vial 6 (**Figure 4H**).

In order to monitor the progression of cancer symptoms, we examined several flies that were treated during second and third instar larval stages several days to weeks after the pupae turned into flies (**Figure 5A-H**). In the first fly, a small tumor was found on the left side of the eye on the first day after the fly eclosed from the pupae (**Figure 5A**). After four days, the tumor size increased until nine days (**Figure 5B-C**) and did not change after that. A similar pattern was observed in a second fly (**Figure 5E-H**) where the tumor size did not grow after nine days.

DISCUSSION

We hypothesized that a combination of sesame and moringa would be more effective as an anti-cancer agent than either plant alone and could help prevent and restrict early stages of tumor growth. We determined the optimal combination of moringa and sesame to prevent tumors in the *Drosophila* eye to be 10% sesame and 15% moringa. In our

Vial #	Stage at which flies were treated	Treatment
Vial #1	2nd instar larval stage	Experimental (10% Se + 15% Mo)
Vial #2	2nd instar larval stage	Control (Water)
Vial #3	3rd instar larval stage	Experimental (10% Se + 15% Mo)
Vial #4	3rd instar larval stage	Control (Water)
Vial #5	Pupal stage	Experimental (10% Se + 15% Mo)
Vial #6	Pupal stage	Control (Water)
Vial #7	Newly eclosed adult stage	Experimental (10% Se + 15% Mo)
Vial #8	Newly eclosed adult stage	Control (Water)

Table 2. Description of the flies, type of food used and the stage at which flies started treatment in each of the eight vials.

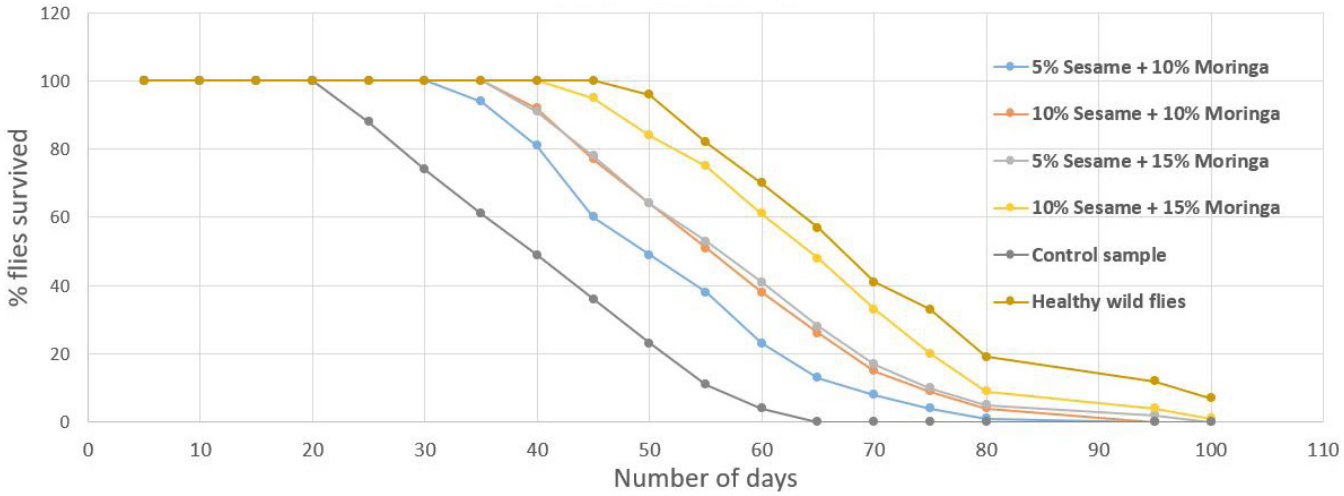

Figure 3. Treatment of flies with all tested combinations of sesame and moringa improved lifespan compared to controls. The lifespan of flies in each condition was calculated as the percent of flies surviving at each timepoint. Mutant flies were administered diets consisting of the indicated combinations of sesame and moringa or a water control. As an additional control, healthy wildtype flies were administered a water control. Twenty flies were analyzed for each vial.

earlier work (25), we showed that sesame at a concentration of 10% can be used to prevent rough eye phenotypes, while moringa at a concentration of 15% was found to be promising for preventing rough eye and uniform ommatidia in this fly model of cancer. In this work, we first wanted to determine the best concentration of each compound. We used different combinations of sesame and moringa. At higher concentrations, such as 15% sesame and 20% moringa, none of the flies survived in any of the samples, so we could not examine the eyes for rough versus smooth eye phenotypes. Past studies showed that high doses of these compounds may actually lessen their anti-oxidant effects (28) and that extremely high doses may cause buildup of iron which can cause gastrointestinal distress and hemochromatosis, a condition caused due to an overload of iron in the body (29).

The fly eyes treated with 10% moringa and any concentration of sesame showed few tumor symptoms and some nonuniform ommatidia. Fly eyes from vials with 15% moringa and 5% sesame showed no tumor symptoms but some nonuniform ommatidia. Fly eyes from vials with 15% moringa and 10% sesame prevented cancer in the *D. melanogaster* eye and the outcomes, that of smooth eye and uniform ommatidia, appeared similar to those of a healthy wildtype fly. The flies treated with 10% sesame and 15% moringa are gene muted flies and hence the eyes of the flies do not look similar to those of the healthy wildtype fly eyes. This work showed that the lifespan of the flies in all the combinations of sesame and moringa increased compared to that of the control flies (Gal4-RET + water). This study also showed that as we increased the concentration of sesame and moringa in the combination, the lifespan of the flies increased, with the best survival rate for 10% sesame and 15% moringa combination. The slope of all the curves are similar, which signifies that the death rate is similar for all the sample flies once the initial flies start to die.

Since we identified the best concentration of each compound to use in the combination, we then treated flies with this optimized combination. We started the treatment at the indicated stage (second instar larval stage, third instar larval stage, pupal stage, and newly eclosed adult stage)

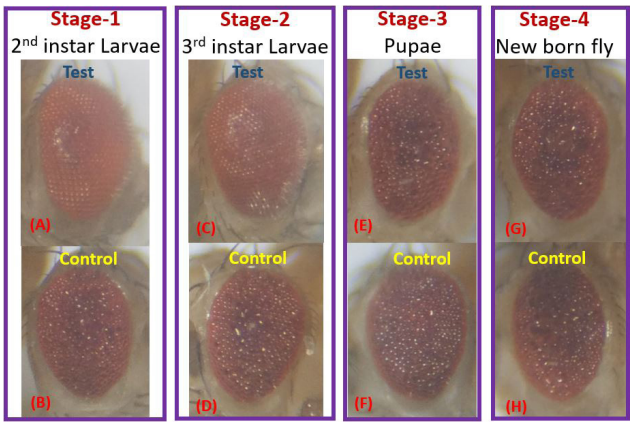

Figure 4. Flies treated during second and third instar larval stages restricted cancer growth compared to controls. A) Representative image of the eyes of the flies from vial #1 (second instar larvae with 10% sesame and 15% moringa combination) showing small area of tumor and uniform ommatidia everywhere else. B) Representative image of the eyes of the flies from vial #2 (second instar larvae with water control), showing cancer symptoms (tumor and nonuniform ommatidia). C) Representative image of the eyes of the flies from vial #3 (third instar larvae with 10% sesame and 15% moringa combination) showing few areas of tumor and uniform-ommatidia in the rest of the area. D) Representative image of the eyes of the flies from vial #4 (third instar larvae) showing cancer symptoms (tumor and nonuniform ommatidia). E) Representative image of the eyes of the flies from vial #5 (Pupa with 10% sesame and 15% moringa combination) showing cancer symptoms (tumor and nonuniform ommatidia). F) Representative image of the eyes of the flies from vial #6 (Pupa), showing cancer symptoms (tumor and nonuniform ommatidia). G) Representative image of the eyes of the flies from vial #7 (eclosed flies with 10% sesame and 15% moringa combination) showing cancer symptoms (tumor and nonuniform ommatidia). H) Representative image of the eyes of the flies from vial #8 (eclosed flies) showing cancer symptoms (tumor and nonuniform ommatidia).

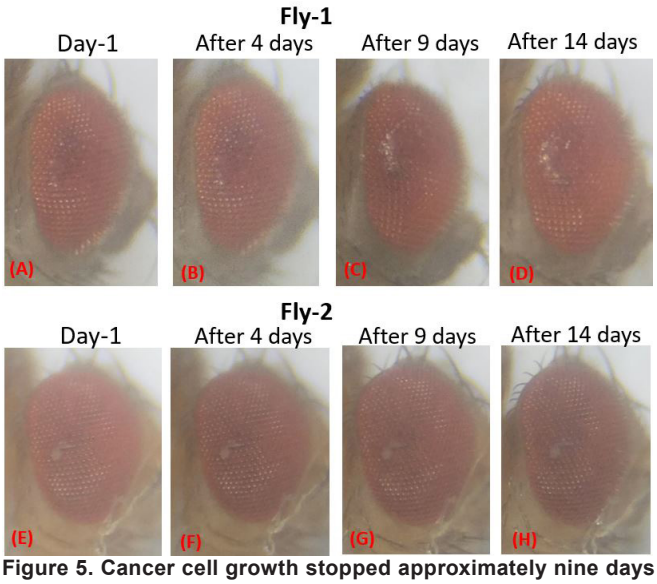

Figure 5. Cancer cell growth stopped approximately nine days after the fly eclosed from the pupal stage for the flies treated during second larvae stage. A-D) Images of the eye of fly #1 from vial #1 (mutant flies treated with 10% sesame and 15% moringa) (A) shortly after, (B) 4 days, (C) 9 days and (D) 14 days after pupae eclosion. E-H) Images of the eye of fly #2 from vial #1 (A) shortly after, (B) 4 days, (C) 9 days and (D) 14 days after pupae eclosion.

and continued through adulthood for the duration of the experiment. During the larval stages, imaginal discs of *D. melanogaster* eyes are formed, and during the pupal stage, eyes are developed (30). Since most of the food consumption in the flies occurs during the larval stages, we reasoned that if we treated the flies before the larval stage, we might prevent cancer occurrence using these natural products (25, 31). Our study revealed that the right combination of sesame and moringa could prevent cancer in *D. melanogaster.*

We were not able to restrict the tumor growth when we treated the flies in the pupal or early adult stages using the combination of sesame and moringa, likely because fly eyes were already developed by the pupal stage. We were also not able to prevent the cancer in the early stages (extract during second instar larvae and third instar larvae) when treated with the experimental food but were able to restrict the cancer cell growth to a certain extent. Cancer cell growth is restricted more severely when treated during second instar larval stage versus during the third instar larval stage. We tried treating the first instar larval flies using 10% sesame and 15% moringa combination but at this stage the larvae are so delicate, handling larvae at the first instar larval stage was lethal to the animals. The fact that we were not able to treat the cancer when treated in the initial stages may be because the natural products took some time to be absorbed into the fly or might require a longer amount of time to work.

The control samples for all the respective experimental stages showed tumors on the entire eye which indicated that the combination of 10% sesame and 15% moringa was indeed a potent combination to restrict cancer cell growth when administered during early stages of fly development. Moringa contains the anti-tumor compound niazimicin (27). Sesamin compound in sesame is known to have high absorbance into cells (25), which perhaps helps increase the absorbance of the compound Niazimicin when the combination of sesame and moringa was taken. The dosage concentrations recommended based on this work are 10% sesame and 15% moringa but in reality, these amounts may not be consumed by most people in their daily diets. Possible methods to increase the amount of moringa we consume is by adding moringa leaves to our soups and stews like lentil soup or chicken soup, adding them to drinks such as hot teas, or adding them to other foods such as scrambled eggs or egg rolls. Possible methods to increase the amount of sesame we consume could include using sesame to season meat or vegetables, to decorate baked goods with sesame seeds, to serve as salad dressing, or to make desserts with sesame oil (32).

Although we tried our best to minimize errors, there were some challenges and limitations in this study. The most challenging part was to collect the newly eclosed flies. Pupae were mostly stuck on the vials. We had to keep monitoring the pupae for eclosing and move them into fresh vials so that we did not mix them up with already present adult flies in the vial. The flies took several hours to eclose out of the pupae, so we had enough time to monitor them. The adult flies in the vial had to be flipped out into another vial on a frequent basis to transfer out the larvae, pupae, and eclosed flies. The microscope used in this study was not a high-resolution microscope, so some of the actual data may slightly vary from what was shown here, as we were unable to see smaller changes, but we do not think this would change the conclusions of the study. Although the flies were anesthetized during analysis, occasionally they moved slightly, making it difficult to capture high quality images. The procedure to pick the larvae could be improved in order to minimize the time the larvae spend exposed to the atmosphere. This might decrease the progression of the tumors size which would need further study. This study showed a combination of moringa and sesame treatments during the second instar or third instar larvae could prevent cancer and also restrict early stages of cancer growth in this specific model of cancer using *D. melanogaster*.

MATERIALS AND METHODS

Drosophila melanogaster care and crosses

Drosophila wildtype, the Oregon-R strain flies were purchased from Carolina Biological Supply Company. The RetMEN2B mutant and UAS-GAL4 driver lines were purchased from Bloomington *Drosophila* Stock Centre. The GMR-Gal4 line (STOCK# 1104) was crossed to the UAS-RetMEN2B line to drive expression of the RetMEN2B allele in the eye. The guidelines of the Carolina ® *Drosophila* manual was used to care the *Drosophila melanogaster* (32). The flies in all the vials were fed with Formula 4-24® Instant *Drosophila* Medium food (15 mL) and water (15 mL). Six to eight grains of yeast were added to each vial.

To treat flies with different combinations of sesame & moringa, at the indicated concentrations, for cancer prevention, four experimental vials along with a control vial without any natural products (water and regular Formula 4-24®) were used to compare with the experimental samples. A cross between UAS-RetMEN2B male flies and GMR-Gal4 female flies was set up by adding six to eight flies from each of the five vials. A sixth control vial was set up with just water and added healthy wildtype flies. After four to five days, the parental flies were separated, and the larvae were allowed to grow into adult flies. In about two weeks, most of the larvae turned into adult flies. Twenty flies were chosen randomly from each vial and scored for the tumors and uniformity on the ommatidia.

To treat flies with a combination of sesame & moringa, at the indicated concentrations, to restrict early stages of cancer cell growth, a cross was setup. The flies were allowed to mate for three to four days, and the parental flies were removed from the vial. Fifteen flies at each of the developmental stages were taken out and moved into eight vials for testing.

Experimental food preparation

Fifteen mL of Formula 4-24® Instant *Drosophila* Medium food was mixed with 15 mL of a liquid solution to make a total of 30 mL food. The liquid solution was a mixture of sesame, moringa, and water. Commercial liquid extracts of organic, Costa Rican *Moringa oleifera* (Pura Vida moringa) and Hawaiian *Sesame indicum* (Hawaii Pharm LLC) were used without further purification. For example, to prepare a sample containing 20% moringa, we added 3 mL of moringa extract to 12 mL of water and mixed well.

Handling and phenotypic analysis

All flies were examined under an AmScope SE306R-PZ-LED Stereo Microscope using 20X, 40X, and 80X magnification. The flies were put to sleep using a FlyNap® Anesthetic Kit (Item # 173010). We followed the procedures in the Carolina® *Drosophila* Manual (33). The difference between a rough eye and a smooth eye under the microscope is shown in **Figure 1E-F**. The *D. melanogaster* compound eye contains approximately 700-750 optical units known as 'ommatidia' (34). Ommatidia could be visibly seen under the microscope and we examined the uniformity qualitatively. The lifespan of the flies was initially measured by counting the number flies that died every five days, at the start of the experiment when deaths were relatively few. Once many flies were dying, we started counting the number of flies that survived.

To test whether the combination of sesame and moringa could restrict early stages of cancer growth, we transported most of the larvae carefully using a paint brush onto on a piece of paper. The second instar and third instar larval stages were separated based on the size of the larvae. Second instar larvae were 1–2 mm smaller than the third instar larvae. We note that it is important not to separate the larvae when they are moving since they elongate and stretch during this movement, making it possible to confuse a second instar for a third instar larva. We also picked some pupae from the vial, leaving some pupae to eclose into adult flies. We placed the vial horizontally and used the back of the paint brush to gently tap the pupae. Once detached from the surface, the pupae were placed on a clean surface.

Received: April 6, 2020
Accepted: June 11, 2020
Published: September 28, 2020

REFERENCES

1. Stewart *et al*. "Cancer prevention as part of precision medicine: 'plenty to be done'." *Carcinogenesis,* vol. 37, no. 1, 2015, pp. 2–9.
2. Freddie Bray *et a*l. "Global cancer statistics 2018: GLOBOCAN estimates of incidence and mortality worldwide for 36 cancers in 185 countries." *American Cancer Society,* CA: A Cancer Journal for Clinicians, vol. 68, no. 6, November/December 2018, pp. 394-424
3. Kulmira *et al*. "Adverse Effects of Cancer Chemotherapy: Anything New to Improve Tolerance and Reduce Sequelae?" *Frontiers in Pharmacology,* Vol 9 , 2018, pp. 245.
4. Arsova-Sarafinovska, Zorica *et al*. "Natural Antioxidants in Cancer Prevention", April 2013, *Macedonian Pharmaceutical Bulletin* 59(1, 2):3 - 14
5. Khamphio *et al*. "Sesamol induces mitochondrial apoptosis pathway in HCT116 human colon cancer cells via pro-oxidant effect." *Life Sciences,* vol. 158, 2016, pp. 46–56.
6. Nayak *et al*. "Sesamol prevents doxorubicin-induced oxidative damage and toxicity on H9c2 cardiomyoblasts." *J ournal of Pharmacy and Pharmacol.,* vol. 65, no. 7, 2013, pp.1083–1093.
7. Abou-Gharbia *et al*. "Effects of processing on oxidative stability of sesame oil extracted from intact and dehulled seeds." *Journal of the American Oil Chemists' Society*, vol 74, no. 3, 1997, pp. 215-221.
8. Geetha *et al*. "Sesamol: an effcient antioxidant with potential therapeutic benefits." *Medicinal Chemistry,* vol. 5, no .4, 2009, pp. 367–371.
9. Prasad *et al*. "A Review on Nutritional and Nutraceutical Properties of sesame." *Journal of Nutrition & Food Sciences*, vol. 2, no. 2, 2012, pp. 1-6
10. Majdalawieh *et al*. "Sesamol, a major lignan in sesame seeds (Sesamum indicum): Anti-cancer properties and mechanisms of action." *European Journal of Pharmacology,* vol. 855, 2019, pp. 75-89.
11. Mukunzi *et al*. "Comparison of volatile profile of moringa oleifera leaves from Rwanda and China using HS-SPME." *Pakistan Journal of Nutrition,* vol. 10, 2011, pp. 602–608.
12. Chumark *et al*. "The in vitro and ex vivo antioxidant properties, hypolipidaemic and antiatherosclerotic activities of water extract of moringa oleifera Lam leaves." *Journal of Ethnopharmacology,* vol. 116, 2008, pp. 439–446.
13. Miyachi *et al*. "Benzyl isothiocyanate inhibits excessive superoxide generation in inflammatory leukocytes:

implication for prevention against inflammation-related carcinogenesis." *Carcinogenesis,* vol. 25, 2004, pp. 567–575.
14. Faizi *et al*. "Isolation and structure elucidation of new nitrile and mustard oil glycosides from moringa oleifera and their effect on blood pressure." *Journal of Natural Products,* vol. 57, 1994, pp. 1256–1261.
15. Waiyaput *et al*. "Inhibitory effects of crude extracts from some edible Thai plants against replication of hepatitis B virus and human liver cancer cells." *BMC Complementary and Alternative Medicine,* vol. 12, 2012, 246–252.
16. Sultana *et al*. "Effect of extraction solvent/technique on the antioxidant activity of selected medicinal plant extracts." *Molecules,* vol. 14, 2009, pp. 2167– 2180.
17. Kumar *et al*. "Antibacterial and antioxidant activity of extract of moringa oleifera leaves-An in vitro study." *International Journal of Pharmaceutical Sciences Review and Research,* vol. 12, 2012, pp. 89–94.
18. Kumar *et al*. "Retinoprotective Effects of moringa oleifera Via Antioxidant, Anti-Inflammatory, and Anti-Angiogenic Mechanisms in Streptozotocin-Induced Diabetic Rats." *Journal of Ocular Pharmacology and Therapeutics,* vol. 29, no .4, 2012, pp. 420-426
19. Tan *et al.* "Moringa oleifera Flower Extract Suppresses the Activation of Inflammatory Mediators in Lipopolysaccharide-Stimulated RAW 264.7 Macrophages via NF-κB Pathway." *Mediators of Inflammation,* 2015, pp. 1-11
20. Pandey *et al*. "Human disease models in *Drosophila melanogaster* and the role of the fly in therapeutic drug discovery." *Pharmacological Reviews,* vol. 63, no. 2, 2011, pp. 411–436.
21. Huo *et al*. "The applications and advantages of *Drosophila melanogaster* in cancer research." *Hereditas,* vol. 36, no. 1, 2014, pp. 30–40
22. Fortini *et al*. "A Survey of Human Disease Gene Counterparts in the Drosophila Genome" The *Journal of Cell Biology,* vol. 150, no. 2, 2000, pp. F23-F29
23. Zoranovic *et al.* "A genome-wide Drosophila epithelial tumorigenesis screen identifies Tetraspanin 29Fb as an evolutionarily conserved suppressor of Ras-driven cancer" *PLOS Genetics*, 2018, pp. 1-36
24. Das *et al*. "Drosophilaas a Novel Therapeutic Discovery Tool for Thyroid Cancer" *THYROID*, vol. 20, no. 7, 2010, pp. 689-95
25. Ganesh *et al.* "Study and comparison of effects of different natural products that can reduce tumor growth using *Drosophila* model", *Journal of Emerging Investigators*, vol. 3, no. 6, 2020, pp. 63-71
26. Abdul Wakil *et al.* "Evaluation of rice bran, sesame and moringa oils as feasible sources of biodiesel and the effect of blending on their physicochemical properties" *RSC Advances*, vol. 4, no. 100, 2014, pp. 56984-56991
27. Pangastuti *et al.* "Natural bioactive compound from *Moringa oleifera* against cancer based on *in silico* screening" *Jurnal Teknologi,* vol. 78, no. 5, 2016, pp. 315-318
28. Hsu *et al*. "Sesame oil does not show accumulatively enhanced protection against oxidative-stress-associated hepatic injury in septic rats" *Journal of Parenteral and Enteral Nutrition*, vol. 32 (2008), pp. 276-280
29. Asiedu-Gyekye *et al.* "Micro- and macroelemental composition and safety evaluation of the nutraceutical *Moringa oleifera* leaves" *Journal of Toxicology*, vol. 2014, no. 4, 2014, pp. 1-13
30. Dübendorfer *et al.* "Development and differentiation in vitro of *D. melanogaster* imaginal disc cells from dissociated early embryos" *Journal of Embryology and Experimental Morphology,* vol. 33, no. 2, 1975, pp. 487-498
31. Zera *et al.* "The physiology of life history trade-offs in animals." *Annual Review of Ecology, Evolution, and Systematics,* vol. 32, 2001, pp. 95-126
32. Elleuch, M., *et al*. "Sesame (*Sesamum indicum L.*) Seeds in Food, Nutrition and Health" *Nuts & Seeds in Health and Disease Prevention*, 2011, pp. 1029-1036
33. Flagg, Raymond O., Ph.D. Carolina ® *Drosophila* Manual. N.p.: *Carolina ® Biological Supply*, 2005.
34. Ross *et al*. "Principles of *D. melanogaster* Eye Differentiation" *Current Topics in Developmental Biology*, vol. 89, 2009, pp. 115–135

Sponsorship

Editor's Circle $10,000+

ALLOY THERAPEUTICS

Patron $5,000+

NEW ENGLAND BioLabs® Inc.
enabling technologies in the life sciences

PORTFOLIOS WITH PURPOSE®

Institutional Supporters

HARVARD UNIVERSITY

HARVARD MEDICAL SCHOOL

Tufts UNIVERSITY

Charitable Contributions

We need your help to provide mentorship to young scientists everywhere.

JEI is supported by an entirely volunteer staff, and over 90% of our funds go towards providing educational experiences for students. Our costs include manuscript management fees, web hosting, creation of STEM education resources for teachers, and local outreach programs at our affiliate universities. We provide these services to students and teachers entirely free of any cost, and rely on generous benefactors to support our programs.

A donation of $30 will sponsor one student's scientific mentorship, peer review and publication, a six month scientific experience that in one student's words, 're-energized my curiosity towards science', and 'gave me confidence that I could take an idea I had and turn it into something that I could put out into the world'. **If you would like to donate to JEI, please visit https://emerginginvestigators.org/support, or contact us at questions@emerginginvestigators.org.** Thank you for supporting the next generation of scientists!

'Journal of Emerging Investigators, Inc. is a Section 501(c)(3) public charity organization (EIN: 45-2206379). Your donation to JEI is tax-deductible. '

emerginginvestigators.org